LATVIAN JOURNAL of PHYSICS and TECHNICAL SCIENCES

ISSN 0868 - 8257

6

SPECIAL ISSUE
(Vol. 60)
2023

CONTENTS

LATVIAN JOURNAL of PHYSICS and TECHNICAL SCIENCES

LATVIJAS FIZIKAS un TEHNISKO ZINĀTŅU ŽURNĀLS

ЛАТВИЙСКИЙ ФИЗИКО-ТЕХНИЧЕСКИЙ ЖУРНАЛ

Published six times a year since February 1964
Iznāk sešas reizes gadā kopš 1964. gada februāra
Выходит шесть раз в год с февраля 1964 года

6 Special Issue (Vol. 60) • 2023

RĪGA

Language Editor: O. Ivanova
Computer Designer: I. Begicevs

INDEXED (PUBLISHED) IN

www.scopus.com
www.sciendo.com
EBSCO (Academic Search Complete, www.epnet.com), INSPEC (www.iee.org.com).
VINITI (www.viniti.ru), Begell House Inc/ (EDC, www.edata-center.com).

Issuers: Institute of Physical Energetics,
Institute of Solid State Physics, University of Latvia
Registration Certificate Number: 000700221

Editorial Contacts:
14 Dzerbenes Street, Riga, LV-1006
LATVIA
tel: +371 26245896
M: +371 29363105
leo@lza.lv

sciendo

LATVIAN JOURNAL OF PHYSICS
AND TECHNICAL SCIENCES
2023, N 6

PREFACE

The application of numerical methods and usage of computers in mathematical modelling of environmental and technological processes has a very long tradition at the University of Latvia. The history of these activities traces back to the late 1960s when the *Computing Centre* of University of Latvia was established, and the first mainframe computers (series *BESM*) appeared there. From the very beginning, physicists were among the most active users of this new equipment. The purpose of these activities was industrial research and they led to the establishment of the Chair for *Electrodynamics and Continuum Mechanics* at the University of Latvia in 1970. Among the founders of that Chair were physicists not only from University but also from the *Institute of Physics* and *Institute of Polymer Mechanics* with ideas for different industrial applications of numerical models. The established contacts with researchers in engineering sciences and active collaboration with leading applied research and development institutions in Moscow, St. Petersburg and Kyiv in the 1970s and 1980s were very fruitful and became one of the major reasons of the success of this research area at the University of Latvia.

In the early 1990s when all organisational structures of research in our country underwent dramatic changes, not all ideas and all institutions managed to adapt successfully to the new conditions. Fortunately, the people who were involved in computer modelling related research were among the most successful. Development of already existing and newly established contacts in Western Europe and reorientation of their applied research to disciplines actively studied in partner universities was also an important factor for financing our research activities. The first agreement of scientific collaboration with a university from the West at the University of Latvia was signed in 1988 with the Leibnitz University of Hannover in the field of numerical modelling for solving different engineering problems in metallurgy and semiconductor industry. This collaboration has been very successful and has various forms nowadays. There are common projects, scientific conferences and publications, there is exchange of researchers and more. As a result, research groups involved in this research successfully joined the international effort related to the application of computer models to industrial processes.

A logical next step for concentration of research activities in this field at the Faculty of Physics and Mathematics was foundation of the *Laboratory for Mathematical Modelling of Environmental and Technological Processes* in 1994 and the *Institute of Numerical Modelling* in 2020. Currently, the research field of engineering physics, the core of which is the multiphysical modelling of environmental and technological processes at the Institute with more than 40 researchers and PhD students, is one of the largest successfully developing scientific areas at the University of Latvia.

Continuing the tradition established by the international scientific colloquiums

Modelling for Materials Processing in Riga (1999, 2001, 2006, 2010 and 2017) and *Modelling for Electromagnetic Processing* in Hanover (2003, 2008 and 2014), the University of Latvia with its long-time cooperation partner Leibnitz University of Hanover organised the 9-th colloquium in Riga in September 2023.

In the colloquium, recent results of numerical and experimental research activities in the field of industrial technologies for creating new and alternative materials, materials with highest quality and purity and new innovative products were presented. In two colloquium sessions, the new achievements in crystal growth research were discussed. Traditionally also applications on basics of multiphysical models with strong interaction of different physical processes – thermal, electromagnetic, and hydrodynamic – were presented. In many cases, the processes in multiphase materials with movement of phase interfaces and melting/crystallisation are successfully researched. This colloquium also gives the opportunity the young researchers and PhD students to present and discuss details of numerical and experimental methods and approaches.

Selected papers devoted to the solving of different engineering problems after reworking are presented in this special edition of the *Journal of Physical and Technical Sciences*.

Andris Jakovičs
Head of the Laboratory of
Multiphysical Processes
Institute of Numerical Modelling
University of Latvia

sciendo

LATVIAN JOURNAL OF PHYSICS
AND TECHNICAL SCIENCES
2023, N 6

DOI: 10.2478/lpts-2023-0041

NUMERICAL MODEL AND SYSTEM FOR PREDICTION AND REDUCTION OF INDOOR INFECTION RISK

J. Virbulis*, J. Telicko, A. Sabanskis, D.D. Vidulejs, A. Jakovics

Institute of Numerical Modelling, University of Latvia,
Jelgavas str. 3, Riga, LV-1004, LATVIA
*e-mail: janis.virbulis@lu.lv

The developed numerical model assesses the risk of a COVID-19 infection in a room based on the measurements of temperature, relative humidity, CO_2 and particle concentration, as well as the number of people and occurrences of speech, coughing, and sneezing obtained through a low-cost sensor system. As the model operates faster than real-time, it can dynamically inform the persons in the room or building management system about the predicted risk level. When the infection risk is high, the model can activate an air purifier equipped with filtration and UV-C disinfection. This solution improves energy efficiency by reducing the ventilation intensity required during colder seasons to maintain the same safety level and activating the purifier only when the predicted infection risk surpasses a specified threshold.

Keywords*: Air purification efficacy, indoor infection risk, virion concentration modelling.*

1. INTRODUCTION

Since the COVID-19 pandemic, opportunities to reduce the infection risk are of utmost interest in the science, technology, and society. Many experts expect that SARS-COV-2 will likely become endemic [1], which means that it will continue to circulate in the world and cause other waves of infection.

SARS COV-2 spreads primarily by respiratory droplets [2]–[4]. There are several pathways for SARS COV-2 transmission: (1) direct transport of exhaled droplets by an infected person into the mouth, nose, or eyes of a susceptible person; (2) touching surfaces contaminated by droplets and subsequently touching the face and (3) via aerosol – inhaling aerosolized microdroplets containing the virus that persist in the air. The risk of infection is especially high indoors where high concentration of aerosols can persist [5], [6]. While maintaining physical distance and regularly disinfecting surfaces and hands can mitigate risks associated with pathways (1) and (2), aerosol transmission remains the predominant factor in an indoor environment [7], [8].

As for infection risks indoors, we have found several models to predict the risk of infection with SARS-CoV-2 [9], [10]; however, only one model uses carbon dioxide (CO_2) as a proxy [11]. Unlike our model, none of the aforementioned models calculate the risk factor in real-time, as they lack integration with a real-time sensor measurement system. Additionally, our system integrates an air purification device that activates based on the model's calculation of virion concentration in aerosols.

We have developed a sensor system that measures various parameters, including temperature, relative humidity (RH), CO_2 concentration, the number of people in the room, particle concentration in the air and others (described in detail in [12]). The sensor system is coupled with a model (described in the present article) that evaluates the risk of COVID-19 infection for an individual in the monitored room. Additionally, the system includes an air purification device with filtration and UV-C disinfection capabilities which is controlled by the model depending on the infection risk.

The model is developed specially for the reduction of COVID-19 infection. However, it can be adapted and used for prediction and reduction of other viral infections, e.g., influenza, by changing the model parameters.

The sensor systems can be used in indoor environments such as auditoriums, offices, public facilities, gyms and more. They serve to alert individuals when the risk of a COVID-19 infection is high, prompting actions like leaving the space or enhancing ventilation. These systems can be centralised, offering automatic monitoring with alert notifications – potentially integrating with building management systems to make the schools, universities, shops, offices, courts, etc. safer.

2. INFECTION RISK MODEL

The model processes sensor data to evaluate the infection risk for a person in the room. The model is integral and predominantly uses the average parameter values for the whole room. The key processes of virus transport are illustrated in Fig. 1. The expelled droplets (1) undergo evaporation, reducing their mass (2). A portion of these droplets settles (3) onto the floor. The smaller particles form an aerosol that can linger in the air for a long time without sedimentation. Virions within this aerosol are transported out of the room through ventilation (4), partially adhere to surfaces (5), or lose their viability over time (6). The aerosols and droplets are filtered and the viability of virions is reduced in the purification device (7). At the end, the droplets and aerosols are inhaled (8) increasing the infection risk of another individual.

2.1. Characteristics of the Model Room

The dimensions of the room – length, width, and height – are used for the calculation of volume, surface area, and vertical distribution of droplets. Data on temperature and RH are taken directly from the measurement system. The room is also characterised by the total mass of CO_2, the count of small airborne aerosol particles (droplets), the total number of virions in aerosol particles, and the number of virions sedimented and deposited on surfaces (mostly on the floor). The quantity and size distribution of large droplets in the air is also accounted for in sedimentation, evaporation, and transport calculations.

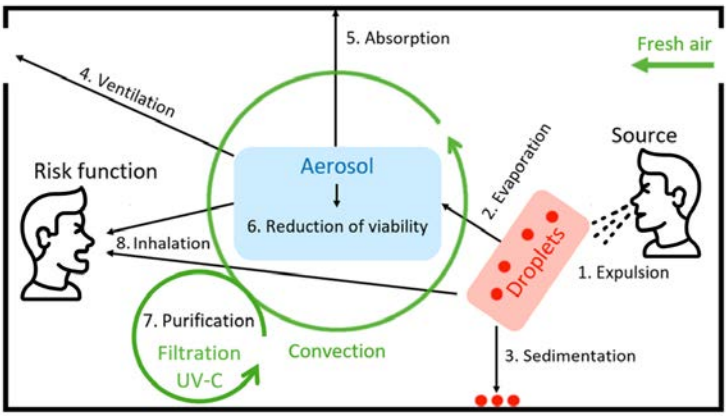

Fig. 1. A schematic overview of the processes incorporated in the model.

2.2. Sources of Virions

The virus is introduced into the room by an infected person as mucus droplets expelled during breathing, speech, coughing and sneezing. Each event is characterised by expulsion of a certain volume of mucus distributed in droplets with a radius of 1.25 μm to 500 μm [13]. The corresponding expelling events are provided to the model by the measurement system analysing the recorded sound. The expelled droplets are initially distributed in a 9 cm high layer 1.2 m above the floor – this corresponds to a sitting person as the most probable position for the considered room types. It is assumed that the droplet density varies in the vertical direction only, since the exact positions of people and the infected person are unknown a priori.

The concentration of COVID-19 in mucus is assumed to be $10^{5.4}$ RNA/ml on average. 20% of infected carry more than 10^7 RNA/ml and 5% carry > 10^8 RNA/ml [14].

2.3. Evaporation of Droplets

Evaporation of mucus droplets is calculated as described in Chaudhuri [5]. The following material properties are considered: density of air ρ, heat capacity of water $c_{p,l}$, thermal conductivity of air k_g, thermal diffusivity of air α_g, diffusivity of water vapor in air D_v, latent heat of evaporation L, RH and temperature of air, initial temperature of droplets T_s.

The evaporation mass flux has two components:

$$\frac{dm_1}{dt} = -4\pi\rho\, D_{\mathrm{v}}\, R_{\mathrm{s}} \ln(1 + B_M),$$

$$\frac{dm_2}{dt} = -4\pi\rho\, \alpha_g\, R_{\mathrm{s}} \ln(1 + B_T),$$

where R_s is the instantaneous droplet radius, B_M and B_T are the dimensionless Spalding mass and heat transfer numbers,

$$B_M = \frac{Y_{1,s} - Y_{1,\infty}}{1 - Y_{1,s}},$$

$$B_T = \frac{c_{p,l}}{h_{fg}} \cdot (T_s - T_\infty).$$

Here, h_{fg} is the specific heat of vaporization, Y_1 is the mass fraction of water vapour, and s and ∞ denotes the location on surface or far field. The energy balance of a droplet is governed by

$$mc_{p,l}\frac{\partial T_s}{\partial t} = -k_g A_s \frac{\partial T}{\partial r} + h_{fg}\frac{dm_1}{dt} - e_l \frac{dm_2}{dt},$$

where m is droplet mass, T_s is instantaneous droplet temperature, k_g is conductivity of gas, A_s is surface area and e_l is specific internal energy of the binary mixture of salt. The change of droplet size and temperature in time is calculated numerically until the minimum size is reached (depending on RH) or droplet get smaller than 5 μm and is added to the airborne part which is assumed to stay in the air for an infinitely long time. The minimum diameter is around 25% of the initial droplet diameter and is dependent on the relative humidity of air [15].

2.4. Sedimentation and Diffusion

Sedimentation is modelled in two ways. For the evaporating (large) droplets, the sedimentation velocity v_{sed} as the function of diameter D and the vertical position are calculated at every time step following [16]:

$$v_{sed} = \sqrt{\frac{4\,\rho_{water}\,g\,D}{3\,\rho_{air}\,C_D}},$$

$$C_D = \left(\left(\frac{24}{Re}\right)^{0.52} + 0.32^{0.52}\right)^{\frac{1}{0.52}},$$

$$Re = \frac{\rho_{air}\,D\,v_{sed}}{\nu}$$

until the floor is reached or a droplet reaches its final size. When the final size is reached, droplet dynamics are calculated by solving a one-dimensional (vertical room dimension) convection-diffusion equation where convection is described by the sedimentation velocity given above and the diffusion accounts for the turbulent mixing of air in the room. Solving equations for every expelled particle group is not possible in the real-time operational model, therefore the solution is prepared beforehand for all pair combinations of 16 diameters (from 5 to 20 μm) and 16 turbulent diffusivities (from 0.00086 to 0.014 m^2/s). The calculated temporal distributions at the height of 1.2 m are the least squares fitted using combination of two exponents and interpolated for any combination of particle diameter and turbulent diffusivity. The turbulent diffusion coefficient K (used in one-dimensional convection-diffusion equation) is calculated from room volume V and ventilation Q according to [17].

$$K = V^{2/3}\left(0.31 + 0.52\frac{Q}{V}\right).$$

The droplets are assumed sedimented if their concentration at the inhalation height of 1.2 m is below 0.1% of the initial concentration.

2.5. Wall Sedimentation

Sedimentation of small airborne particles on surfaces is calculated according to [18]. The mechanism for this sedimentation is Brownian diffusion through the laminar boundary layer. Contrary to the vertical sedimentation, which is faster for larger particles, Brownian diffusion is more pronounced for smaller particles. The rate of wall loss for total particle number N is defined as

$$\frac{dN}{dt} = -\beta\,N.$$

The wall loss rate coefficient

$$\beta = \frac{D_{Br}\,A}{d_{BL}V}$$

depends on surface area A, volume V, thickness of the laminar boundary layer d_{BL}

(assumed 1 cm) and diffusion coefficient

$$D_{Br} = \frac{k_B T\, C_{slip}}{6\,\pi \nu R}$$

where

$$C_{slip} = 1 + \frac{l}{R}\left(1.26 + 0.418\, e^{\frac{-0.867\,R}{l}}\right)$$

l is free path length and R is particle radius.

2.6. Ventilation

The effect of ventilation is considered assuming perfect mixing. The fresh air from the ventilation inlet contains no droplets or virions. It is mixed with the room air and is lead out with the average room concentration. The number of particles N is a function of the ventilation volume flow Q and the room volume V

$$\frac{dN}{dt} = -N\frac{Q}{V}$$

The validity of this simple approach has been demonstrated by 3D air flow simulation in a typical room [19].

The volume flow of ventilation is specified if known, otherwise, the volume flow in the model is varied by PID controller so that the measured and calculated CO_2 concentrations are similar. The applicability of the latter approach is demonstrated in the Results Section.

2.7. Viability Correction

The viability of the virus in aerosols and small droplets decreases over time [20]. The model assumes the following dynamics:

$$N^{i+1} = N^i\, e^{-1.64e-4\,dt}$$

where the constant in the exponent is obtained by digitalising the experimental data from [20].

2.8. Purification

The developed system includes a purification device consisting of fans, filters and UV-C lamps. It is cube-shaped, with UV-C lamps placed along its four walls and M5 class filters at the top and bottom, through which fans blow air. The operation of the device from the view of the model is characterised by the flow rate [m^3/h] and average UV-C intensity [W/m^2] in internal volume.

The filter is characterised by the ability to prevent the passing of a certain part of particles depending on their diameter. The filter type M5 is used in the active device produced during this project. A typical filter efficiency η as a function of diameter D given in [21] is approximated by an analytical formula for more efficient use in the model calculations:

$$\eta = \frac{1}{1 + e^{-5\cdot 10^6 (D - 2\cdot 10^{-6})}}.$$

The filtration in model is considered as follows. The model time step (typically 0.5 seconds) multiplied by the flow rate (m^3/s) gives the filtration volume, which is multiplied by the respective efficiency for considered diameter and divided by the total room volume. This value is multiplied by the total number of particles and, thus, the reduction is calculated.

The disinfection is realised inside the active device when the flowing air is prevailing in the chamber with UV-C lamps. Two effects need to be considered here. The first is the shielding of UV-C light by the outer layers of the particle. Since the light has some penetration depth, virions that are

located deeper in the particle are partially shielded from the disinfection. This effect is estimated using numerical simulation in [22]. The data from this simulation are used to construct a function S which describes the dependence of shielding on the particle diameter D:

$$S = \frac{1}{1 + e^{3.5 \cdot 10^5 \, (D - 5 \cdot 10^{-6})}}.$$

Another effect to be considered is the dose of UV-C radiation necessary to reduce the viability of virions. We use the experimental data from [23]. At irradiation intensity E of 1 J/m^2 the viability B is reduced almost by two orders during one second. The experimental data are fitted using the exponent depending on the device volume V_F and flow rate Q_F:

$$B = 1.45 \, e^{-4.638 \, E \, V_F / Q_F}.$$

To better determine the combined effect of filter and disinfection, both diameter dependencies are represented in one graph, see Fig. 2. Only the efficiencies as functions of diameter are combined here, assuming that the necessary UV-C dose is provided. It can be seen that the chosen combination of the filter size and UV-C is well adjusted, the UV-C treatment extends the reduced filtration capability at lower diameters and there is no dip in the combined efficiency curve. It can be also clearly seen that the efficiency of UV-C does not reach 100% for smaller diameters, the reason following the paper [22] is the reflection of UV-C light on the surface of the particle. Theoretically, at diameters comparable to that of the virion, the efficiency should reach 100%. However, since the aerosol particle is significantly larger, the approximation used is sufficiently accurate.

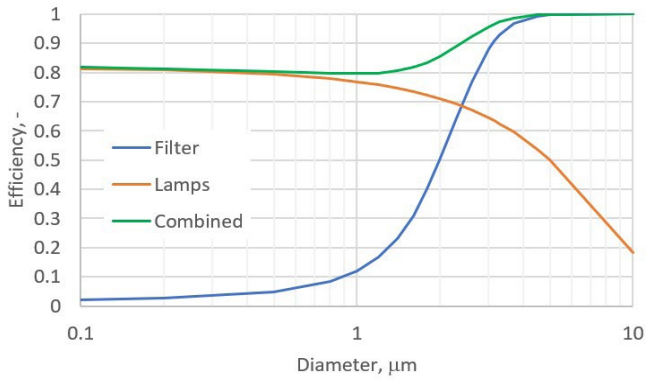

Fig. 2. The efficiencies of filtering, UV-C disinfection and combination of both as a function of particle diameter.

2.9. Inhalation

The person, for whom the infection risk is calculated, inhales 0.4 l/s of air with an average room concentration of aerosols and the concentration of droplets at the height of 1.2 m. Depending on their size, between 19% and 95% of inhaled particles are absorbed [24]. As a result, certain number of virions enter the body, and this count is used to calculate the infection risk.

2.10. Risk Function

The risk function, representing the probability of infection, is derived from [25]. The current understanding suggests that there is not strict threshold for infection in terms of the number of absorbed virions and even one virion can lead to infection. Nevertheless, the probability of infection scales with the number of absorbed virions and is low with only a few particles. This scaling law is called the dose-infection response model. A 50% infection probability corresponds to the absorption of 300 virions:

$$R_{infection} = 1 - (1 - 0.0023)^N,$$

where N is the number of absorbed virions.

To predict the infection risk, some assumptions about the frequency of events associated with different virion sources in the room should be made. The first scenario assumes that the first person in the room is always infected and is expelling the virus with the defined virus concentration according to the frequency of registered instances of breathing, sneezing etc. The infection risk is assessed for the second person entering the room. The same is assumed for other infection spreading events – all speech, cough and sneezing events are assigned to the infected person.

The second scenario takes into account the prevalence of infection in the population. Every person in the room, excluding the second person, has a certain probability of illness depending on the epidemiological state in the country or region. The number of expelled virions in the room is multiplied by prevalence and the number of people in the room. The prevalence of infection is not well known and can change rapidly, therefore the first scenario offers a more straightforward analysis, especially if the effects of ambient parameters and room characteristics are evaluated or compared. Therefore, in this work, it is assumed that the first person in the room is always infected and the infection risk is calculated for the second person.

2.11. Practical Implementation

The MQTT protocol is used for interaction between the sensors and the model. The system, comprising both the sensors and the model, operates for the room specified by MQTT topic. The model continuously monitors the sensor data, calculates the risk function, and publishes it to the room topic as MQTT message. The model listens to messages in the specified topic containing values of temperature, RH, number of persons, events of speaking, coughing, laughing and sneezing. Additionally, the model reads CO_2 measurement data which can be used together with number of people in room to adjust the often unknown ventilation intensity.

The model is written in the Python language and operates notably faster than the real-time on one core of the HPC cluster if a timestep of 0.5 s is used. Most of the computation efforts are allocated to the simulation of droplet evaporation. This is because every droplet size from every cough or sneezing event is treated individually until either the droplets attain an aerosol size due to evaporation or 99.9% of them are sedimented.

3. RESULTS

3.1. Simple Scenarios

In this section, we examine the influence of several model parameters in a simple basic scenario where two individuals, one infected and the other uninfected, enter a previously uncontaminated room. The room dimensions are 3x3x3 m^3, maintaining a steady temperature of 25 °C and RH of 50%. Different virus expulsion scenarios, ranging from continuous breathing and speaking to instances of coughing or sneezing at one-minute intervals are investigated. The data are presented in Fig. 3-left. The use of a logarithmic scale clearly emphasises the substantial difference in risk levels based on the type of the viral expulsion. Speaking elevates the infection risk roughly tenfold compared to breathing alone. Sequentially, coughing increases this risk by another order of magnitude, compared to speaking. Sneezing has the greatest infection risk that is by an order higher than that of coughing. The time required to approach a notable infection risk of 10% aligns with the conventional definition of "contact" for COVID-19 infection, characterised as a 15-minute interaction within 1-meter distance.

Figure 3-right illustrates the effect of viral concentration in an infected individual's mucus on the infection risk. Three distinct cases are shown: the median concentration (where 50% of tested subjects present higher values), the upper 20% and the upper 5% of the infected. Under the assumption of a sneezing once per minute, staying in a room with a highly infectious individual will result in nearly 100% infection probability in just 5 minutes. Nevertheless, the median concentration is used in the model for all other cases.

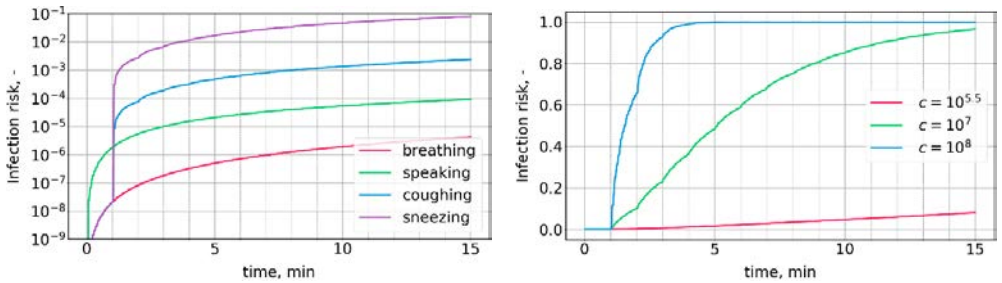

Fig. 3. Left – infection risk for expulsion scenarios (continuous speaking and coughing and sneezing once per minute). Right – infection risk for various virus concentrations in mucus (sneezing once per minute).

The model also reveals the vertical distribution and temporal dynamics of virions in indoor environment. In Fig. 4-left, the number of virions in the same room contained in droplets (D>5 μm) and aerosols (D<5 μm) are shown for different ventilation rates. The lowest ventilation rate of 40 m^3/h corresponds to 1.5 air changes per hour and the highest of 1080 m^3/h to 40 air changes per hour – this rate is approximately equal to the effect of a fully open window. The source of virions in this sce-

nario is sneezing of an infected individual once per minute during the first 10 minutes. Most virions are contained in droplets (note the logarithmic scale) and less in aerosols, however, this difference is reduced during the time without sneezing as the droplets undergo sedimentation due to gravity. The number of virions in aerosols are reduced by ventilation but in the zero-ventilation case mainly due to viability reduction.

Interestingly, the dependence of the number of virions contained in droplets on the ventilation rate is not monotone – at low rates the increase of ventilation causes the increase of the number of virions in the air. The reason is the increased turbulent diffusion which reduces the sedimentation and, therefore, the droplet concentration grows. At low ventilation rates this effect is stronger than the decrease of concentration due to a higher air exchange and only higher ventilation rates of 360 and 1080 m^3/h reduce the number of virions significantly.

The inhaled virions by the second individual are shown in Fig. 4-left with dotted lines. In contrast to the virions in droplets, the count of inhaled virions is a monotonic relationship of the ventilation rate – more virions are inhaled at lower ventilation rates despite the fact that more virions are in the air at the ventilation rate of 40 m^3/h than at 0 m^3/h. The reason for this is the vertical distribution of virions – at higher ventilation they are better mixed and the concentration at 1.2 m height (the inhalation level) is lower.

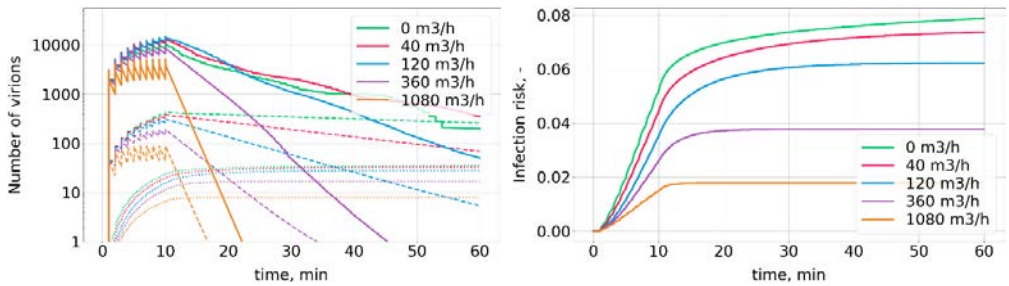

Fig. 4. The effect of the ventilation rate. Left – the number of virions in droplets (solid line), in aerosols (dashed line) and inhaled (dotted line). Right – infection risk. The source of virions is sneezing once per minute during the first 10 minutes.

The corresponding infection risk is depicted in Fig. 4-right. The infection risk increases with time as virions are inhaled. The risk is higher for low ventilation rates, and it grows faster in the first 10 minutes when virions are expelled and their concentration is at its peak. In the subsequent period the risk grows slower for small ventilation rates and the growth stops after just a few minutes for high ventilation rates when the concentration diminishes significantly. In this particular scenario, raising the ventilation rate from zero to 120 m^3/h decreases the infection risk from 8 % to 6 %. A further increase in the ventilation rate to 360 m^3/h reduces the risk significantly to 4 %.

3.2. Room Equipped with the Measurement System

In this section, the prediction of the infection risk in an office with the dimensions of 8.0x6.0x3.5 m^3 equipped with the measurement system is demonstrated and

analysed. The room has a central ventilation system with air inlets and outlets positioned in the ceiling. The ventilation rate is unknown and can vary in time. In the first simulation, a constant rate of 380 m^3/h is assumed.

The simulation was started at midnight and continued for a duration of 48 hours. The measured number of persons and the CO_2 concentration are shown in Fig. 5-left together with the simulated CO_2 concentration. Rapid fluctuations in the recorded number of persons by one are largely attributed to the measurement artefact despite of the advanced camera system and the AI algorithm employed [12].

In Fig. 5-right, the recorded instances of sneezing, coughing, and speech, as well as the calculated risk of infection, are shown. The worst-case scenario is used, it is assumed that the first person entering the room is the virus carrier, and the risk is calculated for the second person. The infection risk is low mainly due to the large room size and the small number of virus expulsion events (comprising a single sneeze and 18 coughing events over two days). This result also emphasises the significance of accurately measuring expulsion events. The model resets the infection risk after 8-hour window with no room occupancy. In this case, the reset occurs at the 33 h mark during the night time hours.

The reason for a disagreement between the measured and simulated CO_2 concentration in the night can likely be attributed to the reduced ventilation intensity between 7 PM and 5 AM. The knowledge of the ventilation intensity is important for an accurate prediction of the infection risk, and it can hardly be predicted by the measurement system e.g., due to manual opening and closing of doors and windows.

To address these limitations, an indirect prediction of the ventilation intensity using the measured number of people and CO_2 concentration is proposed. The PID (Proportional-Integral-Derivative) controller approach is introduced in the model. The measured CO_2 acts as the desired value or setpoint, the simulated CO_2 value is the process value, and the ventilation intensity is the control variable. The PID values were adjusted in several runs to $K_d=2 \cdot 10^{-6}$, $T_i=1 \cdot 10^7$ s, and $T_d=1000$ s. The minimum and maximum ventilation rates are limited to 5 m^3/h and 1080 m^3/h, respectively.

The results with PID control of the ventilation intensity are shown in Fig. 6. The agreement of CO_2 concentration is considerably improved, the ventilation during the night time is strongly reduced in the model and is probably completely turned off in reality. On the first day the PID-adjusted average ventilation rate was 368 m^3/h (2.19 air changes per hour) and on the second day, it was 248 m^3/h (2.47 air changes per hour). The distinct variation of the PID-adjusted ventilation rate could be attributed not only to the used PID method and parameters but also to the potential measurement artefacts of CO_2 concentration and the number of people. Moreover, the unknown CO_2 concentration of the outside air, i.e., the air in the ventilation system, is assumed in a simplified manner to be constant (400 ppm) in this simulation.

The risk of infection is slightly increased from 0.0583% to 0.0603% at the end of the first day and from 0.207% to 0.208% at the end of the second day when the PID-adjusted ventilation was used. The differences are small due to the well guessed ventilation rate during the daytime and the minor effect of ventilation on the infection risk at low air changes as it has already been shown in Fig. 4.

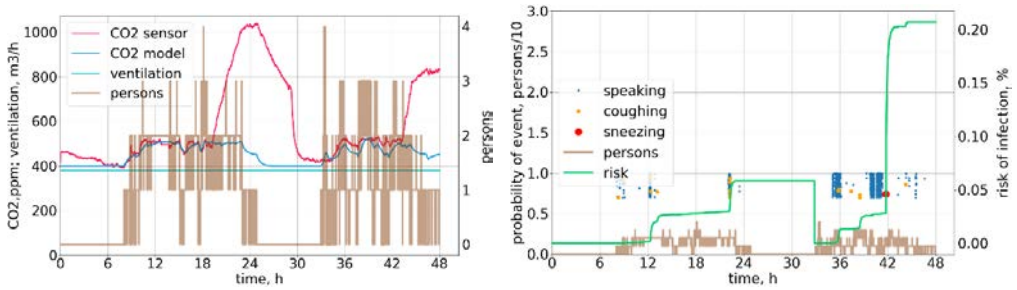

Fig. 5. Left – measured number of people and measured and simulated CO_2 concentrations. Right – measured speaking, coughing, and sneezing events and predicted infection risk in the office room.

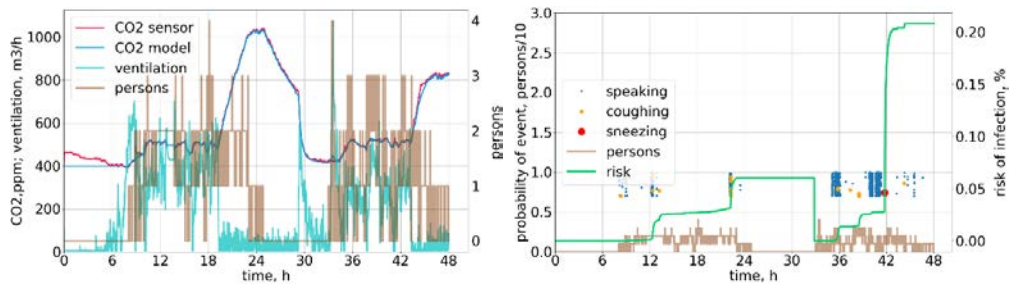

Fig. 6. The same as in Fig. 4, but using the adjusted ventilation intensity.

3.3. Room Equipped with the Purification Device

An alternative to the need of a strongly increased ventilation is the use of a purification device with air filtration and UV-C disinfection. This solution has distinct advantages in cold seasons when a large amount of fresh (outside) air must be heated. As explained in the model chapter, the purification device from the model perspective can be characterised by the flow rate, filter type, volume and UV-C intensity inside the volume. The secondary effect of the purification device on an average turbulent diffusion in the room is not considered. It can be assumed that the presence of the device does not change the measured values, it reduces only the droplet and aerosol concentration, and viability of virions. Therefore, the effect of the purification device in any real scenario can be analysed afterwards also virtually without placing the real device in the room together with the measurement system.

The impact of the purification device is demonstrated in a real operational scenario of 21 January 2023 in Riga, the device being placed in the same office room as described in the previous section. The assumed parameters of the device are the following: the maximum flow rate of 700 m^3/h, the maximum UV-C intensity of 22 W/m^2, the internal volume of 0.2 m^3. The goal of the model is not only to calculate the risk and notify about the increased risk but also to control the filtration and disinfection device. Based on the concentrations of droplets and aerosols, the device is turned on or off, or the intensity of air flow through the filter or the UV-C radiation is adjusted accordingly.

The infection risk is cumulative and the source of risk is the virion concentration in the air, which is used as a control variable. To effectively manage the purification device, defining the thresholds for the low and high

risks is crucial. It is difficult to find absolute definitions, but it is often assumed that the low risk is below 1% and the high is above 5%, considering a time frame spanning from 1 to 10 years. Assuming the worst-case scenario for the office, when a person is present in the room during the entire working day, and the typical duration of seasonal flu outbreaks or the wave of COVID-19 pandemics are 40 working days in a year, a low risk will correspond to a concentration of the virus when the probability of infection will be below 1 % after this time period.

Analysing typical simulations using the infection risk model, the inhaled and absorbed number of virions is around 5 per minute when the average concentration in the air is 1000 m^{-3}. Accordingly, the infection probability is low if the concentration is less than 0.0455 m^{-3} (4.4 inhaled virions in 320 hours) and high if the concentration is higher than 0.233 m^{-3} (22 inhaled virions in 320 hours). The final model assumption is to turn the device on for 50 % of flow and radiation intensity when the virion concentration exceeds the low risk concentration, and to operate it 100% when the virion concentration exceeds the high risk concentration.

Three distinct scenarios have been analysed – the real scenario without a purification device, a scenario with the purification device permanently turned on at full power, and a scenario where the purification device is controlled by the model. The unknown ventilation rate is adjusted using the PID algorithm as described in the previous section. The measured and modelled CO_2 concentrations and the number of people are shown in Fig. 7-left. Dashed lines correspond to cases with constant ventilation of 120 m^3/h and solid lines to PID-adjusted ventilation. It can be seen that contrary to the previous case (Fig. 5-left) the ventilation rate is very low the whole time which is related to high energy prices and regulation of the exceptional energy saving in winter of 2023.

The number of virions in droplets and aerosols, the ventilation and the fan flow rates are shown in Fig. 7-right. It can be seen that the purification device is turned on at full power after sneezing and coughing events as well as after some periods of intensive speaking. It is turned on at half power after less intensive speaking periods. Overall, the purification device is operational for 8.7% of the 24 hours.

The events of virion expulsion together with the infection risk for all three scenarios are shown in Fig. 8. The use of the model-controlled purification device reduces the infection risk relatively by 51% and the continuously switched-on device reduces the risk relatively only by an additional 2%. This proves the efficiency of the model-controlled algorithm as the device can be turned off for 91.3% of time and this increases the infection risk only by the relative 2% (the absolute infection risk is increased from 0.97% to 1.02%).

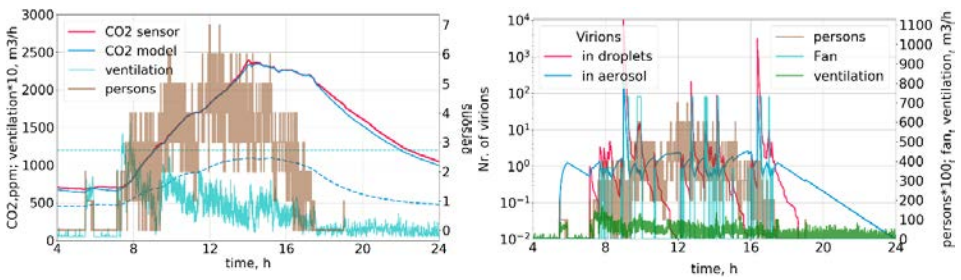

Fig. 7. Left – measured number of people, measured and simulated CO_2 concentrations. Dashed lines are for constant ventilation rate and solid lines for PID-adjusted ventilation rate. Right – the number of virions in droplets and aerosols, ventilation and fan flow rate.

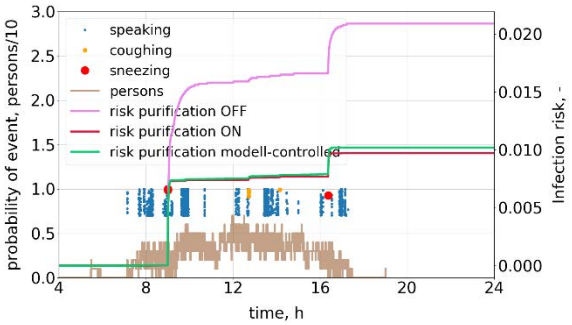

Fig. 8. The measured speaking, coughing, and sneezing events and the predicted infection risk for three different scenarios.

If a comparable reduction of the infection risk should be implemented by ventilation instead of using the purification device, it will lead to a very high energy consumption. A simplified calculation, assuming the average outside temperature of -5 °C on the considered day, room temperature of 18 °C, heat energy price of 0.12 euro/kWh and electric energy consumption of purification device 0.4 kW (costing 0.3 euro/kWh) reveals the price difference of 86 times when both methods operate non-stop for 24 hours. When the purification device operates model controlled, the difference is increased by 11 times more. Although the differences for the average yearly values and considering the recuperation process will be smaller, the use of the purification device instead of ventilation for reduction of the infection risk has a very high potential for energy saving.

4. CONCLUSIONS

The model presented offers an enhanced precision compared to the conventional "contact" definition in prediction of the viral infection risk in an indoor environment. The parameter studies indicate that the infection risk slightly decreases for lower ventilation rates, whereas intensive ventilation decreases the risk considerably. The coughing and especially sneezing events strongly increase the risk of infection in the room; therefore, distinguishing of these events is very important for the risk assessment. Being integrated with the measurement system, the model can predict the real-time infection risk and increase the safety in an indoor environment. A method for determining an unknown ventilation rate by monitoring the number of occupants and the CO_2 concentration has been proposed and tested. The model-controlled purification device using filtration and UV-C disinfection significantly reduces the infection risk, and, in cold weather, it consumes energy several magnitudes lower compared to sole ventilation.

ACKNOWLEDGEMENTS

The present research has been supported by the European Regional Development Fund, Project "System for Prediction and Reduction of COVID-19 Infection Risk in Indoor Environment" No. 1.1.1.1/21/A/046.

REFERENCES

1. Cohen, L. E., Spiro, D. J., & Viboud, C. (2022). Projecting the SARS-CoV-2 Transition from Pandemicity to Endemicity: Epidemiological and Immunological Considerations. *PLOS Pathogens*, *18* (6), e1010591. doi: 10.1371/journal.ppat.1010591
2. Huang, C., Wang, Y., Li, X., Ren, L., Zhao, J., Hu, Y., … & Cao, B. (2020). Clinical Features of Patients Infected with 2019 Novel Coronavirus in Wuhan, China. *The Lancet*, *395* (10223), 497–506. doi: 10.1016/s0140-6736(20)30183-5
3. Liu, J., Liao, X., Qian, S., Yuan, J., Wang, F., Liu, Y., …. & Zhang, Z. (2020). Community Transmission of Severe Acute Respiratory Syndrome Coronavirus 2, Shenzhen, China, 2020. *Emerging Infectious Diseases*, *26* (6). doi: 10.3201/eid2606.200239
4. Chan, J. F.-W., Yuan, S., Kok, K.-H., To, K. K.-W., Chu, H., Yang, J., … & Yuen, K.-Y. (2020). A Familial Cluster of Pneumonia Associated with the 2019 Novel Coronavirus Indicating Person-to-Person Transmission: A Study of a Family Cluster. *The Lancet*, *395* (10223), 514–523. doi: 10.1016/s0140-6736(20)30154-9
5. Chaudhuri, S., Basu, S., Kabi, P., Unni, V. R., & Saha, A. (2020). Modeling the Role of Respiratory Droplets in Covid-19 Type Pandemics. *Physics of Fluids*, *32* (6). doi: 10.1063/5.0015984
6. Nishiura, H., Oshitani, H., Kobayashi, T., Saito, T., Sunagawa, T., Matsui, T., … & Suzuki, M. (2020). Closed Environments Facilitate Secondary Transmission of Coronavirus Disease 2019 (COVID-19). *medRxiv*. doi: 10.1101/2020.02.28.20029272
7. Asadi, S., Bouvier, N., Wexler, A. S., & Ristenpart, W. D. (2020). The Coronavirus Pandemic and Aerosols: Does COVID-19 Transmit via Expiratory Particles? *Aerosol Science and Technology*, *54* (6), 635–638. doi: 10.1080/02786826.2020.1749229
8. Santarpia, J. L., Herrera, V. L., Rivera, D. N., Ratnesar-Shumate, S., Reid, St. P., Denton, P. W., … & Love, J.J. (2020). The Infectious Nature of Patient-Generated SARS-CoV-2 Aerosol. *medRxiv*. doi: 10.1101/2020.07.13.20041632
9. Bazant, M. Z., & Bush, J. W. M. (2020). Beyond Six Feet: A Guideline to Limit Indoor Airborne Transmission of COVID-19. *medRxiv*. doi: 10.1101/2020.08.26.20182824
10. Peng, Z., Rojas, A. L. P., Kropff, E., Bahnfleth, W., Buonanno, G., Dancer, S. J., … & Jimenez, J.L. (2021). Practical Indicators for Risk of Airborne Transmission in Shared Indoor Environments and their Application to COVID-19 Outbreaks. *medRxiv*. doi: 10.1101/2021.04.21.21255898
11. Peng, Z., & Jimenez, J. L. (2021). Exhaled CO2 as a COVID-19 Infection Risk Proxy for Different Indoor Environments and Activities. *Environmental Science & Technology Letters*, *8* (5), 392–397. doi: 10.1021/acs.estlett.1c00183
12. Telicko, J., Vidulejs, D. D., & Jakovics, A. (2021). A Monitoring System for Evaluation of COVID-19 Infection Risk. *Journal of Physics: Conference Series*, *2069* (1), 12192. doi: 10.1088/1742-6596/2069/1/012192
13. Duguid, J. P. (1946). The Size and the Duration of Air-Carriage of Respiratory Droplets and Droplet-Nuclei. *Epidemiology and Infection*, *44* (6), 471–479. doi: 10.1017/s0022172400019288
14. Schijven, J., Vermeulen, L. C., Swart, A., Meijer, A., Duizer, E., & de Roda Husman, A. M. (2020). Exposure Assessment for Airborne Transmission of SARS-CoV-2 via Breathing, Speaking, Coughing and Sneezing. *medRxiv*. doi: 10.1101/2020.07.02.20144832
15. Fabian, P., Brain, J., Houseman, E. A., Gern, J., & Milton, D. K. (2011). Origin of Exhaled Breath Particles from Healthy and Human Rhinovirus-Infected Subjects. *Journal of Aerosol Medicine and Pulmonary Drug Delivery*, *24* (3), 137–147. doi: 10.1089/jamp.2010.0815

16. Holterman, H. (2003). *Kinetics and evaporation of water drops in air*. Wageningen: IMAG report 2003-12
17. Kai-Chung Cheng, Viviana Acevedo-Bolton, Ruo-Ting Jiang, Neil E. Klepeis, Wayne R. Ott, Oliver B. Fringer, and Lynn M. Hildemann. Modeling Exposure Close to Air Pollution Sources in Naturally Ventilated Residences: Association of Turbulent Diffusion Coefficient with Air Change Rate. *Environmental Science & Technology* 2011 *45* (9), 4016-4022 DOI: 10.1021/es103080p
18. Park, S. H., Kim, H. O., Han, Y. T., Kwon, S. B., & Lee, K. W. (2001). Wall Loss Rate of Polydispersed Aerosols. *Aerosol Science and Technology*, *35* (3), 710–717. doi: 10.1080/02786820152546752
19. Virbulis, J., Sjomkane, M., Surovovs, M., & Jakovics, A. (2021). Numerical Model for Prediction of Indoor COVID-19 Infection Risk Based on Sensor Data. *Journal of Physics: Conference Series, 2069* (1), 12189. doi: 10.1088/1742-6596/2069/1/012189
20. van Doremalen, N., Bushmaker, T., Morris, D. H., Holbrook, M. G., Gamble, A., Williamson, B. N., … & Munster, V.J. (2020). Aerosol and Surface Stability of SARS-CoV-2 as Compared with SARS-CoV-1. *New England Journal of Medicine*, *382* (16), 1564–1567. doi: 10.1056/nejmc2004973
21. Shi, B. (2012). Removal of Ultrafine Particles by Intermediate Air Filters in Ventilation Systems: Evaluation of Performance and Analysis of Applications (p. 177). Chalmers University of Technology (Sweden).
22. Doughty, D. C., Hill, S. C., & Mackowski, D. W. (2021). Viruses Such as SARS-CoV-2 can be Partially Shielded from UV Radiation when in Particles Generated by Sneezing or Coughing: Numerical Simulations. *Journal of Quantitative Spectroscopy and Radiative Transfer*, *262*, 107489. doi: 10.1016/j.jqsrt.2020.107489
23. Gidari, A., Sabbatini, S., Bastianelli, S., Pierucci, S., Busti, C., Bartolini, D., … & Francisci, D. (2021). SARS-CoV-2 Survival on Surfaces and the Effect of UV-C Light. *Viruses*, *13* (3), 408. doi: 10.3390/v13030408
24. Stahlhofen, W., Rudolf, G., & James, A. C. (1989). Intercomparison of Experimental Regional Aerosol Deposition Data. *Journal of Aerosol Medicine*, *2* (3), 285–308. doi: 10.1089/jam.1989.2.285
25. Basu, S. (2020). Computational Characterization of Inhaled Droplet Transport in the Upper Airway Leading to SARS-CoV-2 Infection. *medRxiv*. doi: 10.1101/2020.07.27.20162362

sciendo

LATVIAN JOURNAL OF PHYSICS
AND TECHNICAL SCIENCES
2023, N 6

DOI: 10.2478/lpts-2023-0042

CFD ANALYSIS OF AIRBORNE PATHOGEN DISINFECTION IN A UV-C AIR PURIFICATION DEVICE

A. Sabanskis, D. D. Vidulejs, J. Virbulis, A. Jakovics

Institute of Numerical Modelling, University of Latvia,
Jelgavas Street 3, Riga, LV-1004, LATVIA,
*e-mail: andrejs.sabanskis@lu.lv

Numerical simulations of the airflow inside a portable air purification device have been carried out. The simplified system geometry is comprised of key components – fans, particle filters and UV lamps for disinfection, which are included in the model. The study investigates the velocity distribution, UV irradiance, and its impact on air disinfection. The effects of the flow rate and UV dose on the purification efficacy have been investigated. The findings provide valuable insights for optimising the design and configuration of air purification devices, and their potential role in reducing the transmission of airborne diseases.

Keywords: *Aerosol transport, air filtering, COVID-19, computational fluid dynamics, UV disinfection.*

1. INTRODUCTION

In the domain of public health and disease control, the containment of airborne pathogens has necessitated the need for development and evaluation of effective air purification technologies. The airborne pathogens, which include a wide spectrum of microorganisms like bacteria, viruses, and fungi, can cause diverse health issues upon entering the respiratory system [1]. Some specific examples include the influenza A virus, SARS-CoV-2, Mycobacterium tuberculosis, and Stachybotrys chartarum or black mould. As these microorganisms can spread via respiratory droplets or aerosols, enclosed spaces, particularly those with an inadequate ventilation, pose a significant risk for their transmission [1]. The resulting challenge is the development and validation of devices capable of efficiently disinfecting air, reducing the risk of exposure and potential transmission of airborne diseases.

Ultraviolet (UV) radiation disinfec-

tion, notably via UV-C light, has been used as a potent tool for inactivating a broad spectrum of microorganisms [2]. The specific wavelength of UV radiation works by inducing cell damage to the DNA or RNA of the microorganism, thus rendering the pathogens non-infectious [3]. During the COVID-19 pandemic, an interest in the efficacy of UV-C radiation against coronaviruses, especially SARS-CoV-2, has surged. A comprehensive review [4] investigated the UV doses required to achieve a 90% reduction in coronavirus count. Their analysis, rooted in previous studies on coronavirus photoinactivation, suggests that the log-reduction dose for these viruses ranges from a conservative median upper limit of 10.6 mJ/cm^2 to a more realistic estimate median of 3.7 mJ/cm^2. On the other hand, the study [5] suggests that SARS-CoV-2 is much more sensitive to UV irradiance than previously thought. The researchers have conducted in vitro experiments using cells infected with SARS-CoV-2 at different viral concentrations. The study has found that even a low UV-C dose of 3.7 mJ/cm^2 could achieve an inactivation of 3-log without any signs of the viral replication, regardless of the viral concentration.

For the quantification of air purifier performance, the metric of Clean Air Delivery Rate (CADR) has been established by the Association of Home Appliance Manufacturers [6]. CADR quantifies the air purifiers in terms of removing a volume of airborne particulates from the room. For an operating air purifier, the mean concentration of contaminants in the room follows the exponential relationship

$$C(t) = C_0 \exp(-k\, t), \tag{1}$$

where C_0 represents the initial concentration at time $t = 0$ and k denotes the decay rate. This relationship can be further expanded to derive the CADR as $\mathrm{CADR} = k\, V$, with V being the total volume of air in the room. CADR is the product of the airflow rate and the single-pass efficiency of the purification device (the percentage removal of pollutants passing through the device). The CADR is specified for particles sized 0.3 μm and larger. However, pathogens such as viruses, bacteria, and fungal spores not suspended in water or mucus droplets fall within the size range of 0.02 to 0.3 μm [1]. Moreover, the CADR is traditionally specified for devices which use particulate filters and not germicidal UV lamps. Therefore, while a high CADR indicates a device's effectiveness for particle removal, it does not necessarily guarantee its efficacy against airborne microorganisms. In the present study, similarly to [2], we chose to extend the definition of the CADR to include the airborne pathogen deactivation.

Ensuring the performance of purification systems requires a fundamental understanding of the flow dynamics involved in the air purification process, the irradiation conditions, and the characteristics of the airborne pathogens. For this purpose, computational fluid dynamics (CFD) has been utilised for simulating and optimising the performance of air purification devices (see, e.g., [7]). CFD allows for the modelling of complex interactions between the air flow, UV-C irradiance, and airborne particles, thereby enabling the detailed analysis and optimization of device parameters. However, only a few related works which explicitly investigate the air flow inside the purifier and model disinfection by UV light are available in the literature.

The study [8] proposes a novel conceptual design for a low-cost UVC-LED air purifier consisting of a dust-filter assembly, a UVC chamber, and a fan. The dust filter aims to reduce dust accumulation, the UVC chamber utilises turbulence-generating grids and a unique LED arrangement to promote

air mixing and pathogen inactivation, and the single high-static pressure fan ensures a high airflow rate. CFD is used to analyse the airflow patterns, irradiance distribution, and disinfection performance of the device. They employed the k-omega SST turbulence model, suitable for transitional flows, and the assumed frozen turbulence, where the velocity of the particle is much larger than the eddy velocity. They also assumed isotropic turbulence for estimating the particle motion. The irradiation was modelled using the Lambert's cosine law, assuming an inverse square distance law which neglects scattering and absorption by the air. A disinfection rate of over 97% was demonstrated for SARS-CoV-2 and tuberculosis, and over 92% for influenza A, at a flow rate of 100 L/s (360 m^3/h) and power consumption below 300 W. The turbulence-generating grid enhances air mixing, maintaining a uniform distribution of pathogens in the UVC chamber and ensuring effective disinfection.

For a different use case, [9], the CFD simulation study focuses on the use of in-duct UV-C lamp arrays for air disinfection in ventilation systems. The researchers investigated the effect of lamp array configurations on average UV dose, UV dose distribution, and disinfection rate. Four different lamp array positions were examined within a square cross-section ventilation duct. The k-ε turbulence model and the Lagrangian particle model were used to analyse the air flow and the particle distribution, and the Discrete Ordinates (DO) radiation model was employed to obtain the UV irradiance field, which considers the refraction and reflection of the UV radiation. The study has found that the lamp array position significantly affects the UV dose distribution. With an average air speed of 2.5 m/s and 4 UV-C lamps with a power of 8.5 W each, the highest average UV dose obtained was 19.12 J/m^2, while the lowest was 18.30 J/m^2. The corresponding disinfection rates for the MS2 bacteriophage virus were calculated as 56.05% and 54.47%, respectively. The study highlights the importance of considering not only the average dose values but also the dose distribution and standard deviation for the evaluation of UV-C disinfection systems.

The DO model, including the shadowing effect, has also been applied in [10] to calculate the irradiance produced by an UVC lamp in the upper corner of a room. An increase in the disinfection rate by 50–85% was demonstrated; however, the whole room was irradiated, which might not be practical for real-world applications.

In [11] a shielded UV irradiation device engineered for both air and surface sanitization has been developed. The device contains a staggered grid of 28 low-intensity (11 W) UV lamps and is designed to offer a broad cross-sectional airflow and an extended path for the effective irradiation of airborne particles. Experiments were conducted to assess various performance metrics, including UV irradiation quality, ozone generation, and disinfection efficiency against bacterial and viral aerosols. A six-log reduction (99.9999%) was achieved for multiple types of microbial aerosols within a 10-second exposure, while maintaining ozone levels within permissible limits. The device high efficacy and safety profile render its potent solution for a variety of settings, including healthcare facilities and public spaces, particularly in responding to infectious airborne diseases such as COVID-19. However, this work is mainly experimental – only one CFD simulation of the air flow inside the device was presented, without analysing the purification process.

Another study [12] investigated the performance of a novel UV disinfection reactor for water disinfection. They utilised a combination of numerical simulations and experimental measurements to evaluate its

performance. The researchers developed a 3D model of the reactor and employed ANSYS-Fluent software to simulate the UV dose under different inlet flow rates and UV powers. Notably, they introduced an innovative and efficient approach to validate their simulations by measuring the absorbance of hydroxyl radicals using an H_2O_2 solution. The experimental results aligned with the predictions from the CFD simulations, validating their modelling approach. The study emphasised the significance of flow dynamics and radiation distribution when designing and optimising water disinfection devices and found that reducing the flow rate is more cost-efficient than increasing the UV power.

According to the literature review, the air flow and UV irradiation inside air purifiers are seldom investigated. In this study we conduct a CFD analysis of the airborne pathogen disinfection performance in a prototypical portable air-purification device, focusing on the processes inside the device. The modelled device consists of two particle filters at both ends, many high-static pressure fans in parallel for high airflow as well as flow-aligned UV-C lamps. The device parameters such as flow rate, UV-C dose and lamp count are varied to observe the effect on the performance.

2. METHODS

2.1. System Description

The geometry of the air purifier is based on the in-house prototype device, but is simplified – fine features, such as screws, are not considered in the CFD simulations, see Fig. 1. The purifier is divided into volumetric regions for the top and bottom particle filters, and regions for each of the fans. The purifier has outer dimensions of 615x657x840 mm^3 and is installed in a room of size 3x3x3 m^3. The distance between the air purifier and the floor is 55 mm (device legs are not included in the model), it is equipped with 36 fans, 80x80 mm^2 each, and 20 UV-C lamps with a total electrical power P = 318 W. The fans create an upward air flow; a deflector is installed in the upper part of the device. The lamps have a cylindrical shape, with a diameter of 25 mm and a length of 440 mm. In the numerical simulations, the lamps can be turned on individually to evaluate their performance with respect to air disinfection; however, the heating due to the lamps is neglected. Assuming the airflow rate Q = 220 m^3/h, the air passing through the device is expected to heat by $\Delta T = P/(\rho c_p Q) \approx 4$ K on average.

A MERV 8 filter is modelled, which boasts a particulate removal rate of greater than 70% in the range of 3 to 10 μm, working synergistically with the UV-C light presumed to effectively inactivate microorganisms smaller than 3 μm. The filter aids in capturing larger particles and dust, also acting as a pre-filter.

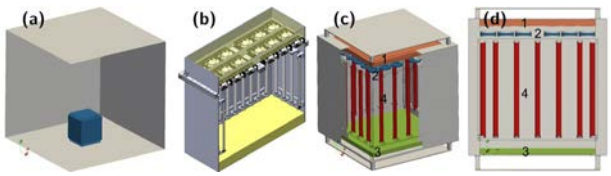

Fig. 1. System geometry. (a) – global view, (b) – CAD model of the air purifier, (c) – simplified air purifier geometry used in CFD simulations, (d) – vertical cross-section of the air purifier. 1 – top filter, 2 – regions for fans, 3 – bottom filter, 4 – UV lamps.

2.2. Air Flow

The CFD model predicts the steady-state air velocity distribution inside the purifier device as well as in the room. The Navier-Stokes and continuity equations are solved using the Finite Volume Method (FVM) software OpenFOAM. k-omega SST turbulence model is used, and the results are averaged over the last 2000 iterations.

In the filter regions, the Darcy-Forchheimer porosity model is applied as a source term for the velocity field $\vec{U}$. Two model parameters have to be provided – Darcy coefficient $d = 4667118\ \mathrm{m}^{-2}$ for the linear term with respect to the velocity and Forchheimer coefficient $f = 22.7898\ \mathrm{m}^{-1}$ (calculated based on the 1" PerfectPleat HC M8 curve from [13]) for the quadratic term according to the equation

$$S = \nabla p = -\left(\mu d + \frac{\rho U}{2} f\right)\vec{U}, \qquad (2)$$

where $\mu = 1.83 \cdot 10^{-5}\ \mathrm{Pa \cdot s}$ is the dynamic viscosity and $\rho = 1.2\ \mathrm{kg/m^3}$ is the density of air.

Regarding the fans, their blades are not included in the model. Instead, a momentum source is applied for selected cells to ensure a specified mean velocity over the fan cross-section. Each fan is controlled individually, requiring the same flow rate (the total flow rate divided by the number of fans). Since the air velocity near the UV lamps is of the greatest interest, we believe these simplifications are justified by the presence of particle filters, which laminarise the flow.

To test the influence of the filters, additional simulations were carried out with top and/or bottom filter removed. While the pressure drop would be lower for such cases if the fan power were unchanged, we assumed the same flow rate in the model regardless the filter configuration.

2.3. UV Radiation Disinfection

The UV irradiation dose D absorbed by a particle is characterised by the irradiance E and the exposure time t. The dose required for inactivation of a microorganism is often characterised by the Log-reduction dose, representing a 90% reduction in the species concentration. The log-reduction can be expressed as:

$$\ln(0.1) = -2.30 = -z\,E\,t = -z\,D, \qquad (3)$$

where z is the inactivation constant. For instance, in this study, we use the median dose required for a log-reduction of SARS-CoV-19, which is 3.7 mJ/cm^2 or 37 J/m^2 [4]. Calculating for the inactivation constant, we obtain $z = 0.0622\ \mathrm{m^2/J}$. This UV disinfection process follows a first-order kinetic model, where the rate of inactivation is directly proportional to the concentration of viable pathogens. The simplified inactivation process of the pathogen concentration C from an initial value of C_0 can be described by the exponential decay equation:

$$C(t) = C_0 \exp(-zEt). \qquad (4)$$

The geometry of the simulated UV-C disinfection device can be seen in Fig. 1. The inner volume has reflective aluminium coated side walls and UV-C lamps located near the walls. We model an undisclosed germicidal UV-C lamp, designed for air disinfection units. The UV-C lamp consumes 15.9 W of power and emits 4.9 W of UV-C. In this study the irradiance is calculated by mathematical integration over the source, neglecting scattering and absorption by the air.

The irradiance E at a given point can be

described by the radiant power P emitted by the lamp over a closed surface S. For a point light source, the irradiance at a distance of r is given as:

$$E = \frac{P}{S} = \frac{P}{4\pi r^2}. \tag{5}$$

The straight UV lamp can be modelled as a uniform line source in xyz coordinates, spanning a length L in the z axis. For a point located inside the UV disinfection chamber, we must integrate over the irradiance contributions lengthwise. The limits of the integral, z^- and z^+ are coordinates from the point z to both ends of the lamp, where $z^+ - z^- = L$. For each point in the numerical grid, the total irradiance of a single lamp with linear power density $P_l = P/L$ is calculated as:

$$E(x,y,z) = \int \frac{dP}{4\pi r^2} = \frac{P_l}{4\pi} \int_{z^-}^{z^+} \frac{dz'}{x^2 + y^2 + (z - z')^2} = \\ = \frac{P_l}{4\pi\sqrt{x^2 + y^2}} \left[\tan^{-1}\left(\frac{z^+ - z}{\sqrt{x^2 + y^2}} \right) - \tan^{-1}\left(\frac{z^- - z}{\sqrt{x^2 + y^2}} \right) \right]. \tag{6}$$

The total irradiance field produced by all lamps is obtained by superposition. Additionally, reflections are considered in a simplified manner, treating the vertical aluminium walls as smooth, specularly reflecting mirrors with a reflectance $R = 0.85$. Reflections from each wall are calculated once, without considering any multiple or subsequent reflections. For simplicity, the lamps are assumed to be transparent, meaning they do not cast any shadows.

The UV irradiance was calculated on a fine uniform structured grid using Python's NumPy library. The irradiance field is resampled to cell centres on the OpenFOAM mesh and implemented as a negative source term (sink) in the numerical solver. The corresponding UV chamber mesh region contains around 1.69 million cells.

2.4. Pathogen Species Transport

Particles in CFD simulations can be modelled using either the Lagrangian or Eulerian particle transport model. In the Lagrangian approach, individual particles or droplets are tracked as they move through the flow field. This method calculates the kinematic trajectories of each particle, considering the effects of the flow field and gravitational force. The Lagrangian approach is particularly useful for cases with low particle counts and significant particle mass, where the dynamics of individual particles is important.

On the other hand, the Eulerian approach treats particles as a continuous phase within the fluid or gas (such as air). This method is applicable when the mass of particles is negligible, and the Stokes number is much smaller than 1. The Stokes number is defined as the ratio of the particle response time to the characteristic flow time scale. The Eulerian approach is suitable for cases where the particles move with the flow field and their individual dynamics are not critical. At the minute timescale, the Eulerian particle transport model is effective in describing aerosolized particles with diameters up to 20 μm [14].

Due to their small mass, these particles can be treated as part of the continuous fluid phase, allowing for efficient simulation of their transport and dispersion in the flow field. Moreover, most pathogenic microorganisms and viruses are below this size and the UV-C irradiation is most effective in this range [3]. For these reasons, we employ the Eulerian particle transport model in this study.

The time-dependent transport of the pathogen species concentration C is described by the advection-diffusion equation with an additional source term for the influence of UV irradiance:

$$\frac{\partial C}{\partial t} + \nabla \cdot \vec{U}C = \nabla \cdot (D_{\text{eff}} \nabla C) - zEC, \qquad (7)$$

where $\vec{U}$ is the air velocity, $D_{\text{eff}} = D + D_t$ is the effective diffusion coefficient, $D = 10^{-11}$ m^2/s – Brownian diffusion coefficient, $D_t = \nu_t / \text{Sc}_t$ – turbulent diffusion coefficient with ν_t being the turbulent kinematic viscosity and $\text{Sc}_t = 0.8$ – turbulent Schmidt number. The effect of the top and bottom particle filters on the concentration distribution is not considered in the model.

The turbulent diffusion of particles in the air is described by the effective diffusion coefficient D_{eff}. This coefficient accounts for the random particle motion due to thermodynamics and the mixing of particles caused by turbulence in the airflow. The turbulent diffusion coefficient D_t is calculated using the turbulent kinematic viscosity (ν_t) field and the turbulent Schmidt number (Sc_t). The turbulent kinematic viscosity is calculated in the RANS airflow simulation. The turbulent kinematic viscosity represents the rate at which the turbulent fluctuations in velocity are dissipated.

For each of the air purifier configurations with different airflow and irradiation parameters, we simulate the airborne pathogen's concentration distribution over time. The initial conditions for the simulation are uniform relative concentration $C_0 = 1$. The zero gradient boundary condition is applied for all surfaces. The simulations are conducted until time $t = 60$ s.

The uniform starting concentration was chosen to estimate the CADR of the air purifier. This simulation setup slightly diverges from the [6] measurement standards because it typically employs a mixing fan to ensure a homogeneous aerosol distribution in the room. However, as evident in the simulations, the concentration distribution at the device inlet is relatively homogeneous throughout the simulation timeframe. In our previous work, a more realistic initial distribution of the aerosol and the effects of different heating regimes were investigated numerically [15].

3. RESULTS AND DISCUSSION AIR FLOW

The finite volume mesh of the considered system has been created by the snappyHexMesh utility from the OpenFOAM software. It consists of approx. 4.9 million cells, with an additional mesh refinement inside the air purifier and at the room walls. Mesh size of 40 mm far from the walls and 2.5 mm at the air purifier walls and in the fans was chosen based on our previous experience in modelling the air flow and CO_2 transport [16], [17].

Different scenarios were considered for the air flow simulations as summarized in Table 1. They include the reference case, cases with reduced and increased flow rate, as well as simulations without one or both air filters.

Table 1. Summary of the Considered Cases for Airflow Simulations

Case	Mean fan velocity, m/s	Description
A	0.5	Reference case, flow rate 220 m^3/h
B	0.37	Reduced flow rate 160 m^3/h
C	0.2	Reduced flow rate 90 m^3/h
D	1	Increased flow rate 440 m^3/h
E	0.5	Without top filter
F	0.5	Without bottom filter
G	0.5	Without both filters

The calculated global air flow pattern for the reference case is shown in Fig. 2. The flow inside the air purifier is directed upwards. When leaving the purifier, the air is diverted horizontally by a diffuser (top lid), and flows towards the walls of the room, where it splits. Two vortices are formed – one above the air purifier, and another between the air purifier and floor. The bottom vortex feeds the air intake at the bottom of the purifier. Another diffuser (bottom lid) is installed below the air intake, so the air is entering from the sides and is not sucked from below.

A zoomed-in view of the air flow pattern inside the purifier is shown in Fig. 3. The results indicate that the bottom filter is especially important for keeping the air flow homogeneous. Note that for the reference case, due to the different cross-sectional areas of the fans and the inner region of the air purifier where the lamps are located, the mean air velocity inside the purifier is approximately two times lower than the mean velocity through the fans.

Figure 4 shows the vertical velocity component for different configurations of top and bottom filters. For the reference case the flow rate in the centre of the air purifier is quite homogeneous. There are only small changes in the flow field for the case without the top filter. However, when the bottom or both filters are removed, the air forms a strong central jet and even exhibits a downward flow near the corners of the purifier. Additionally, the flow thorough the fans is also affected – it becomes less homogeneous, with a noticeable backflow, especially for the fans closest to the walls.

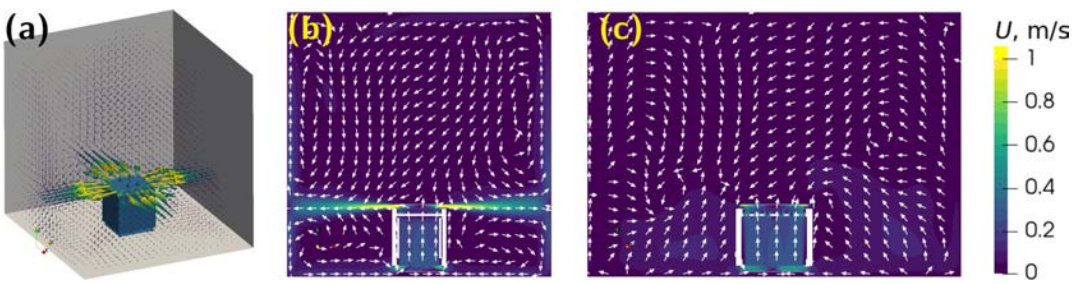

Fig. 2. Global velocity distribution (case A): (a) – 3D view with variable length vectors, (b) and (c) – vectors of equal length in vertical cross-sections at 0° and 45° planes, respectively.

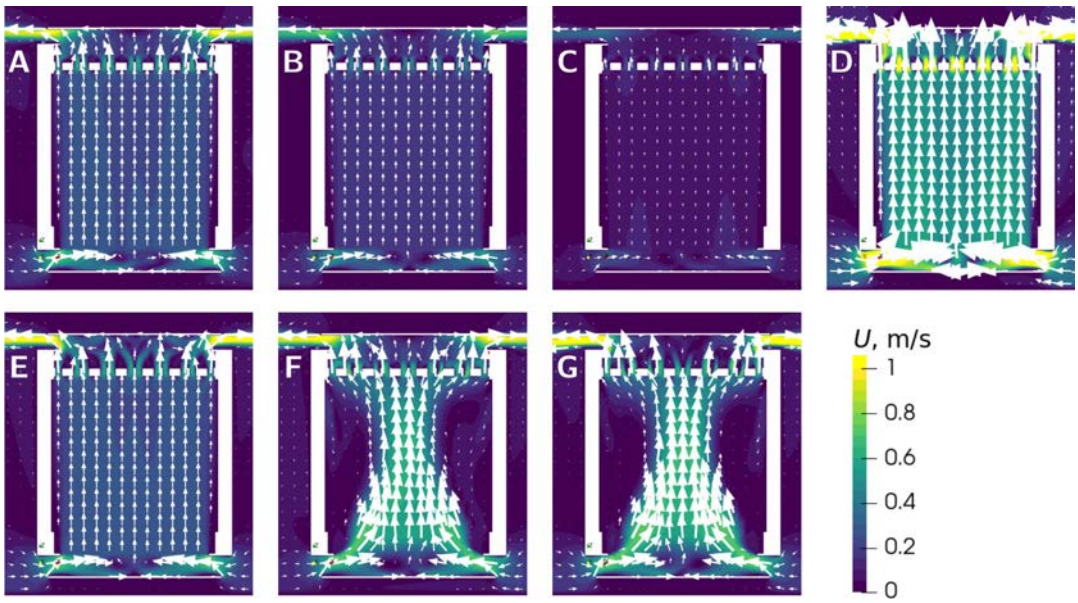

Fig. 3. Velocity distributions inside the air purifier for different scenarios A–G (XZ plane through the centre of the second row of fans).

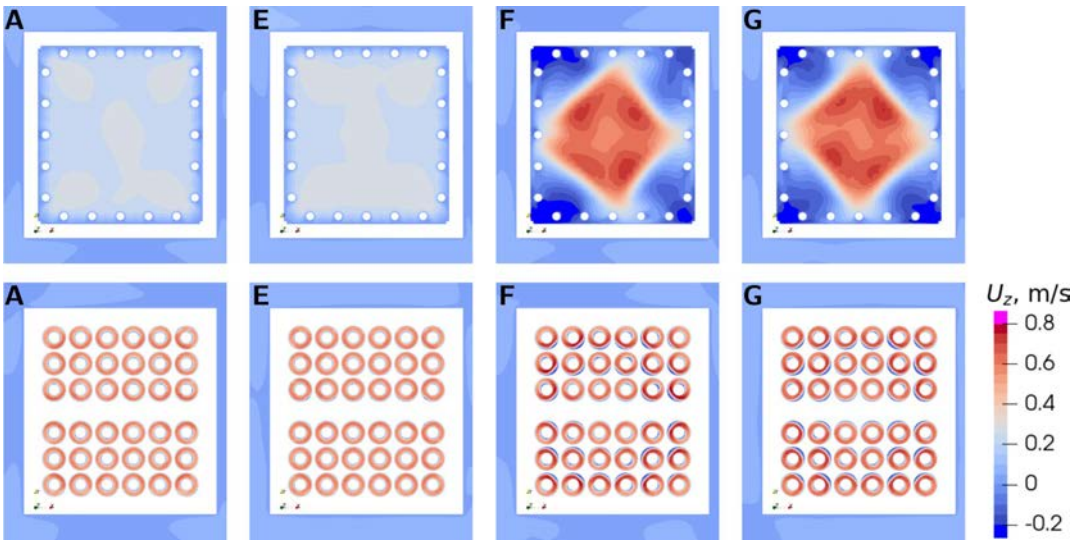

Fig. 4. Distributions of the vertical velocity component in XY (horizontal) cross-sections through the centre or the air purifier (top row) and through the fans (bottom row).

3.1. UV Light Intensity and Air Disinfection

The resulting irradiance field for 20 (all) UV lamps is visualised in Fig. 5. The XY and YZ cross-sections are drawn in the middle of the device. The irradiance is high-

est near the lamps and rapidly drops with distance. In the vertical direction the intensity is highest in the middle. The average irradiance value in the volume is 236 W/m^2.

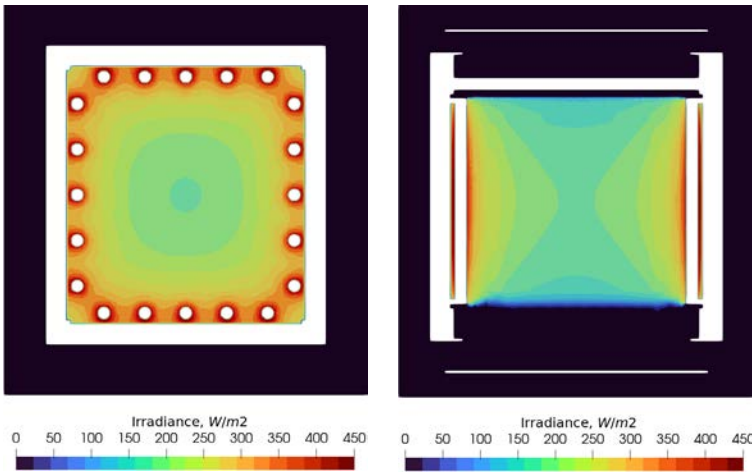

Fig. 5. XY and YZ cross-section of irradiance with 20 UV lamps.

The air purification performance of the device can be quantified with the CADR and pathogen log-reduction values. For each timestep of the simulation, the average pathogen concentration in the room is saved for data analysis. The resulting plot is then fit to the CADR equation (1), and all simulation CADR values are collected in Table 2. The pathogen log-reduction values for the different airflow configurations and lamp counts are collected in Tables 2 and 3.

The air purifier's pathogen log-reduction value is obtained by studying the decrease in pathogen concentration over the Z axis. This is done by plotting a line centred within the UV chamber, going from the device inlet to the outlet, the direction of decreasing concentration. This line extends parallel to the airflow and the lengthwise UV lamps, in the Z axis. There is an exponential decline in the pathogen concentration along this direction because the pathogen is irradiated by a progressively larger UV dose. The curve is fit to an exponent $C(z) = Ae^{-Bz}$ with coefficients A and B and the log-reduction rate is expressed. Notably, the centre of the purifier on the plane perpendicular to the airflow (XY plane) coincides with the least UV irradiation due to the device design. This provides us with a conservative estimate of the device pathogen concentration log-reduction rate.

The relative airborne pathogen concentration after 60 seconds for the reference case (A) with 20 UV lamps can be seen in Fig. 6. The UV disinfection device blows streams of purified air into the room, which diffuses with the contaminated air. There is a feedback loop, where a part of the purified air recirculates back into the inlet of the device. Nevertheless, during the 60 second simulation the device is constantly supplied with contaminated air. The air volume of the 3x3x3 m^3 room (including the device) is 26.9 m^3, which results in 0.13 air changes per minute and 7.66 air changes per hour for this case. The CADR value of this configuration is 206 m^3/h and the pathogen log-reduction is 6.64, which corresponds to a disinfection rate of 99.99998%.

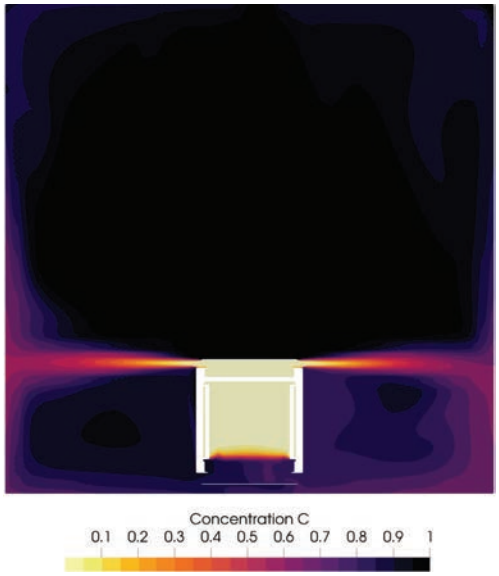

Fig. 6. YZ cross-section of concentration after 60 seconds for the reference case (A).

While a high disinfection rate is generally desirable, it may be excessive considering the power usage of the UV lamps, each consuming 15.9 W. Another factor to be considered is that the CADR value may be more important than the disinfection rate, since a larger CADR corresponds to a larger volume of the air purified. By analysing the simulation results within the context of the specific application requirements (e.g., classroom, hospital ward), the device design can be iteratively optimised for energy efficiency and performance.

Table 2. Calculated Air Purification Efficacy for Different Cases Sorted by CADR

Case	CADR, m^3/h	Log-reduction
C	80	13.6
B	149	8.57
E	203	6.48
A	206	6.65
F	208	3.76
G	209	3.70
D	396	3.50

As an optional post-processing step, we solve for the irradiation dose on the numerical mesh in OpenFOAM, see Fig. 7. Analogously to the concentration, the irradiation dose is treated as a scalar field in Eq. (8), excluding the turbulent diffusion term, since it is defined for a specific particle size and mass. The irradiation dose is obtained after a few seconds, when the particles would have traversed the device once.

$$\frac{\partial D}{\partial t} + \nabla \cdot \vec{U} D = E. \tag{8}$$

The irradiation dose in Fig. 7 is not used for the calculation of pathogen concentration, since it does not account for the turbulent diffusion of the concentration. Nevertheless, it is indicative of the irradiance dose received by the particles when traversing the device once. The side-by-side comparison of the two cases in Fig. 7 illustrates the importance of the airflow pattern. Both cases have an equal mean velocity, but the case without the bottom filter alters the airflow pattern unfavourably for disinfection. There is also some backward flow at the air intake.

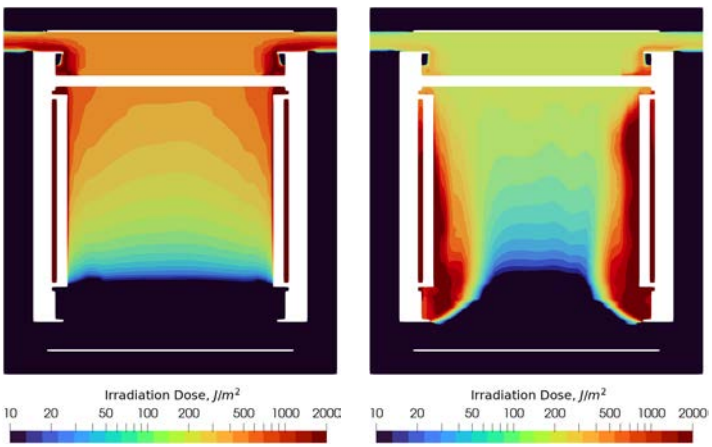

Fig. 7. YZ cross-section of irradiation dose for cases A (left) and F (right) with 20 UV lamps.

For cases without the bottom filter, the log-reduction of contaminants along the centre line is roughly 1.7 times smaller (see Table 2). The irradiation dose is lower due to a compound effect – the airflow is focused around the XY plane centre, which is also where the irradiance intensity is the lowest. The bottom filter acts to laminarise the airflow pattern, distributing the contaminants evenly along the cross section.

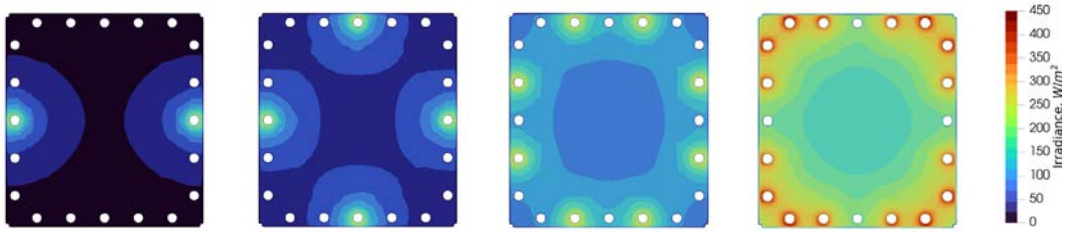

Fig. 8. Irradiance field at XY cross-sections for increasing UV lamp counts.

Figure 8 displays XY cross-sections of the irradiance field for increasing UV lamp counts within the UV disinfection device. The configurations comprise of 2, 4, 8, and 16 lamps, while the remaining lamps are turned off. The mesh, consisting of 20

lamps, remains the same across all configurations. In the case with 2 and 4 lamps, they are situated directly opposite each other, centrally positioned on the walls. For 8 lamps a staggered pattern is used to maintain symmetry.

Table 3. CADR and Disinfection Rates for Increasing UV Lamp Counts

No. of UV lamps	CADR, m^3/h	Log-reduction	Disinfection rate
2	182	0.946	88.7%
4	202	1.75	98.2%
8	205	3.10	99.92%
16	206	5.37	99.9996%
20	206	6.65	99.99998%

The data in the accompanying Table 3 indicate the air purification performance of each lamp configuration. As the number of UV lamps increases from 2 to 4, the CADR increases by only 11% and further increase in lamp count brings diminishing returns. The CADR value for the simulated UV-C disinfection devices depends mostly on the airflow rate. The log-reduction scales linearly with the lamp count N_{lamp}:

$$\log_{10}\frac{C}{C_0} = -0.31\, N_{lamp} - 0.50. \qquad (9)$$

4. CONCLUSIONS

CFD simulations of the air flow and disinfection using UV light have been carried out. The particle filters produce a homogeneous flow distribution inside the device, allowing for a better irradiation of the pathogens. The number of UV lamps has a weak but noticeable (below 15%) influence on the CADR but it strongly affects the total power consumption of the device which scales linearly with the lamp count. A compromise between the power consumption and the disinfection rate must be chosen according to the particular use case. The most important parameter influencing the CADR is the flow rate – the CADR increases with the flow rate almost linearly. The disinfection rate (log-reduction) is higher for lower flow rates since the particles spend a longer time inside the air purifier. In future, the developed mathematical model should be experimentally validated.

ACKNOWLEDGEMENTS

The present research has been supported by the European Regional Development Fund, Project “System for prediction and reduction of COVID-19 infection risk in indoor environment”, No. 1.1.1.1/21/A/046.

REFERENCES

1. Tang, J., Li, Y., Eames, I., Chan, P., & Ridgway, G. (2006). Factors Involved in the Aerosol Transmission of Infection and Control of Ventilation in Healthcare Premises. *The Journal of Hospital Infection, 64* (2), 100–114. doi:10.1016/j.jhin.2006.05.022
2. Kujundzic, E., Matalkah, F., Howard, C., Hernandez, M., & Miller, S. (2006). UV Air Cleaners and Upper-Room Air Ultraviolet Germicidal Irradiation for Controlling Airborne Bacteria and Fungal Spores. *Journal of Occupational and Environmental Hygiene, 3* (10), 536–546. doi:10.1080/15459620600909799
3. Kowalski, W. (2009). *Ultraviolet Germicidal Irradiation Handbook: UVGI for Air and Surface Disinfection*. Springer Berlin Heidelberg. doi:10.1007/978-3-642-01999-9
4. Mankar, V., Dhengre, A., Agashe, N., Rodge, H., & Chandi, D. H. (2020). Ultraviolet Irradiation Doses for Coronavirus Inactivation – Review and Analysis of Coronavirus Photoinactivation Studies. *GMS Hygiene and Infection Control, 15*, 466-472. doi:10.3205/DGKH000343
5. Biasin, M., Bianco, A., Pareschi, G., Cavalleri, A., Cavatorta, C., Fenizia, C., ... & Clerici, M. (2021). UV-C Irradiation is Highly Effective in Inactivating SARS-CoV-2 Replication. *Scientific Reports, 11* (1), 1–7. doi: 10.1038/s41598-021-85425-w
6. ANSI/AHAM AC-1. (2006). *Method for Measuring Performance of Portable Household Electric Room Air Cleaners.*
7. Mohamadi, F., & Fazeli, A. (2022). A Review on Applications of CFD Modeling in COVID-19 Pandemic. *Archives of Computational Methods in Engineering, 29* (6), 3567–3586. doi: 10.1007/s11831-021-09706-3
8. Kapse, S., Rahman, D., Avital, E. J., Venkatesan, N., Smith, T., Cantero-Garcia, L., ... & Beggs, C.B. (2023). Conceptual Design of a UVC-LED Air Purifier to Reduce Airborne Pathogen Transmission – A Feasibility Study. *Fluids, 8* (4), 111. doi: 10.3390/fluids8040111
9. Atci, F., Cetin, Y. E., Avci, M., & Aydin, O. (2020). Evaluation of In-duct UV-C Lamp Array on Air Disinfection: A Numerical Analysis. *Science and Technology for the Built Environment, 27* (1), 98–108. doi:10.1080/23744731.2020.1776549
10. Buchan, A. G., Yang, L., & Atkinson, K. D. (2020). Predicting Airborne Coronavirus Inactivation by Far-UVC in Populated Rooms Using a High-Fidelity Coupled Radiation-CFD Model. *Scientific Reports, 10* (1). doi: 10.1038/s41598-020-76597-y
11. Martinovs, A., Mezule, L., Revalds, R., Pizica, V., Denisova, V., Skudra, A., … & Juhna T. (2021). New Device for Air Disinfection with a Shielded UV Radiation and Ozone. *Agronomy Research, 19* (S1), 834–846. doi: 10.15159/AR.21.068
12. Pan, Y., Tian, X., Zhang, B., Zhu, Z., Pan, H., Rahman, M. M., & Leng, J. (2020). Numerical Verification for a New Type of UV Disinfection Reactor. *Ain Shams Engineering Journal, 11* (4), 1191–1200. doi:10.1016/J.ASEJ.2020.03.014
13. AAF. (2023). *Product Catalog*. Available at https://aafeurope.com/
14. Vuorinen, V., Aarnio, M., Alava, M., Alopaeus, V., Atanasova, N., Auvinen, M., … & Osterberg, M. (2020). Modelling Aerosol Transport and Virus Exposure with Numerical Simulations in relation to SARS-CoV-2 Transmission by Inhalation Indoors. *Safety Science, 130*, 104866. doi: 10.1016/j.ssci.2020.104866
15. Sabanskis, A., Vidulejs, D. D., Teličko, J., Virbulis, J., & Jakovičs, A. (2023). Experimental and numerical evaluation of the efficiency of an indoor air cleaner under different conditions. In M. Schweiker, C. van Treeck, D. Müller, J. Fels, T. Kraus, & H. Pallubinsky (eds.), *Proceedings of Healthy Buildings 2023 Europe*, (pp. 522–530). Aachen, Germany.

16. Sabanskis, A., & Virbulis, J. (2016). Experimental and Numerical Analysis of Air Flow, Heat Transfer and Thermal Comfort in Buildings with Different Heating Systems. *Latvian Journal of Physics and Technical Sciences, 53* (2), 20–30. doi: 10.1515/lpts-2016-0010

17. Virbulis, J., Sjomkane, M., Surovovs, M., & Jakovics, A. (2021). Numerical Model for Prediction of Indoor COVID-19 Infection Risk Based on Sensor Data. *Journal of Physics: Conference Series, 2069* (1), 12189. doi: 10.1088/1742-6596/2069/1/012189

sciendo

LATVIAN JOURNAL OF PHYSICS
AND TECHNICAL SCIENCES
2023, N 6

DOI: 10.2478/lpts-2023-0043

MODELLING OF METHANOL PRODUCTION FROM BIOGAS

V. Kharitonov[2,3] *, V. Geza[2], L. Rodin[2,3], M. Shorohov[1]

[1]Encata LLC,
Riga, Pulka Str. 3, LV-1073, LATVIA
[2]University of Latvia, Riga,
Jelgavas Str. 3, LV-1586, LATVIA
[3]Chemical Technological Company LLC,
Shveykiv, Chortkivskyi Dst., Ternopil Rgn.,
Dobrovodivsky Cheremkhiv Str. 15, 48314, UKRAINE
*e-mail: viktor.kharitonov@chtc.com.ua

This article presents a computer model for the methanol production from biogas. The stages of autothermal and steam reforming of biogas and the methanol synthesis cycle are considered. A study has been performed on the influence of the composition of biogas and the method of its conversion on the amount of methanol produced. As a result of the computational experiment on the model, the optimal composition of biogas has been determined and the applicability of the methods of autothermal and steam reforming has been assessed. An assessment has been made of reducing the carbon pressure on the environment during the processing of biogas into methanol.

Keywords*: Autothermal reforming, biogas, climate change, methanol technology, steam reforming, synthesis gas.*

1. INTRODUCTION

The production and processing of biogas is an important element in the fight against the climate change. The composition of biogas includes mainly methane (up to 60 % by volume) and carbon dioxide – greenhouse gases that have the greatest impact on the environment. But, since biogas is produced from renewable natural materials and participates in the carbon cycle, its use does not contradict to the idea of a "green" transition and does not increase the carbon footprint. Intense development of the biogas production and the processing industry [1] over the past decades is associated with the

relative simplicity and low cost of biogas production, on the one hand, and high tariffs for electricity traditionally produced from biogas [2], due to the policy of a "green" approach to energy on the other.

However, the reduction in electricity tariffs is forcing biogas producers to look for other ways to use biogas. Processing biogas into chemical products is a good way to get a product with a higher added value from biogas. In addition, a significant part of the carbon contained in biogas passes into a bound state and is removed from circulation, thereby reducing the carbon pressure on the environment. Such processes are carbon-negative. Methanol production may be the best way in this sense, as methanol has a wide range of uses as a raw material in the production of a vast range of chemicals, from acetic acid to a variety of varnishes, resins and plastics. It can also be used in fuel cells and as motor fuel.

Considering the small unit capacity of biogas plants from 8000 to 30000 nm^3 per day, the production of methanol for biogas processing "on site" should be within 1–3...5 thousand tons of methanol per year. This allows for the use of compact and modular plants. In this work, the influence of the degree of purification of biogas from CO_2 and the method of obtaining synthesis gas on the composition of the converted gas has been studied in order to determine the optimal conditions for the synthesis of methanol. A comparative evaluation of autothermal and steam reforming methods has been carried out.

2. DEVELOPMENT OF A METHANOL PRODUCTION COMPUTER MODEL

A computer model was developed to perform the task of analysing the effect of the composition of biogas and the method of its conversion on the productivity of the methanol plant and its ability to reduce carbon pressure. A computer model was developed in the environment of the SATR-XTK[1] software, which has been used for many years to simulate stationary operating modes of chemical production. The main area of application is the production of methanol, ammonia, hydrogen and synthesis gas. With its help, many projects have been completed, both for the reconstruction and modernization of existing production facilities and projects for new production facilities. A distinctive feature of the SATR-XTK software is a wide range of modules for the simulation of complex technological equipment and a database of kinetic dependencies for calculating catalytic processes.

The computer model consists of a calculation scheme of the methanol production stages, a database of physical and chemical properties of substances, their mixtures, kinetic dependencies and SATR-XTK software. In the formulation of this paper, the stages of biogas conversion and the stage of methanol synthesis were considered.

Certain model representations of physical and chemical processes occurring in the units and apparatuses of the technological scheme were chosen when developing calculation schemes. Thus, in this formulation of the problem, the processes of heat transfer were represented by the simplest linear dependencies that determine the given heat load. Vapor-liquid mass transfer processes

[1] "https://en.chtc.com.ua/soft/"

were described using the thermodynamic approach. The non-ideal behaviour of the phases was taken into account by the Redlich-Kwong equation of state in the Soave modification [3].

The main processes in methanol production are catalytic reforming and catalytic methanol synthesis. The methanol synthesis process is carried out on a copper catalyst with heat release. The reaction mechanism is represented by the following equations:

$$CO + H_2O = CO_2 + H_2 \quad (I)$$

$$CO_2 + 3H_2 = CH_3OH + H_2O \quad (II)$$

Since, due to thermodynamic limitations, the drawdown of raw materials does not exceed 10 % under industrial conditions, a circulation scheme of synthesis is used. The methanol synthesis reactor can be made in the form of a shaft, shelf or tubular apparatus.

Synthesis gas obtained from biogas conversion is used for the synthesis of methanol. The process can be represented by the following reaction equations:

$$CH_4 + H_2O = CO + 3*H_2 \quad (III)$$

$$CH_4 + 0.5*O_2 = CO + 2*H_2 \quad (IV)$$

$$CO + H_2O = CO_2 + H_2 \quad (V)$$

$$2CO = CO_2 + C \quad (VI)$$

In the case of autothermal reforming [4], the initial mixture consists of methane, oxygen, and water vapor. The heat required for reaction (III) is provided by the oxidative reaction (IV). At certain ratios of the reacting components, the process becomes autothermal, i.e., self-sustaining. The autothermal converter is usually a shaft-type reactor.

During steam reforming, methane and water vapor enter into the reaction [5]. The heat for reaction (III) is provided by an external heat source. The reactions of autothermal and steam reforming take place on different modifications of the nickel catalyst. The undesirable phenomenon of soot formation (VI) is suppressed by the steam content in the mixture. Steam reforming is carried out, as a rule, in tubular reactors. The heat of the reaction is supplied through the wall of the reaction tubes. When choosing a model representation of the processes occurring in the catalytic layer, the following assumptions were made:

- steady heat exchange and flow movement;
- homogeneous and isotropic catalyst bed in all directions;
- the physical characteristics of the flow are constant throughout the layer (do not depend on time);
- the layer size is much larger than the grain diameter;
- grain temperature is equal to the flow temperature at the same point of the layer.

In this case, the catalytic layer flow model becomes the plug flow model [6], and the mathematical description of the chemical transformation in the catalytic layer can be written as:

$$w \cdot \frac{dC_i}{dl} = -V_c \cdot W_i(C,T) \quad (1)$$

$$w \cdot \rho \cdot c_p \cdot \frac{dT}{dl} = Q \cdot W_i(C,T) \quad (2)$$

with boundary conditions:

$$l = 0; \quad C_i = C_{io}; \quad T = T_o \quad (3)$$

where w is the flow rate, ρ is the density, c_p is the heat capacity, C_{i0}, C_i are the initial and final concentration of the component i, l is the axial coordinate, Q is the heat of reaction, T is the flow temperature, T_0 is the initial flow temperature, $W_i(C, T)$ is the reaction rate per unit volume of the catalyst, V_c is the volume of the catalyst.

Thus, the mathematical description is reduced to a system of ordinary differential equations and can be solved by one of the well-known numerical methods, such as the 4th-order Runge-Kutta. To describe the chemical reactions under conditions of heat transfer through the reactor wall, the system of equations was supplemented by the heat transfer equation. In order to reduce computational costs, the phenomenon of radial thermal conductivity of the layer was not taken into account, the diameter of the reaction tubes was determined based on the experience of industrial operation.

To calculate the rate of reactions (I-II), the Rozovsky kinetic equation [7] was used, and the rate of reaction (III) was calculated using the Froment kinetic equation [8]. Equations (IV-V) were calculated in the equilibrium approximation.

The methanol synthesis reactor is a tubular type apparatus with reaction heat removal through the pipe walls and steam generation. The autothermal converter is a shaft-type apparatus, and the steam reforming reactor is a tubular apparatus with fire heating of the reaction tubes.

Figure 1 shows the calculation scheme for the production of methanol, and Figs. 2 and 3 are for the schemes to obtain synthesis gas by autothermal and steam reforming methods, respectively.

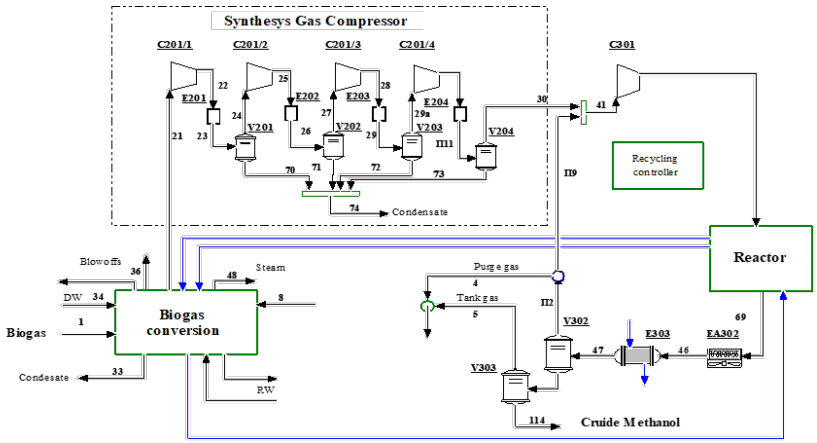

Fig. 1. The methanol production calculation scheme.

The calculation scheme for methanol production combines the calculation blocks of the stages of biogas conversion and methanol synthesis and allows the calculation of the material and heat balance of the entire production. The methanol synthesis cycle consists of a C301 circulation compressor, a methanol synthesis reactor with a vaporization system, a circulation gas cooling and condensation system, EA302 and E303 heat exchangers, a V302 separator and a V303 raw methanol collector. Synthesis gas from the conversion stage is compressed to the required pressure and injected into the synthesis cycle by a C201 compressor.

The calculation scheme for the conversion of biogas into synthesis gas by the method of autothermal reforming is shown in Fig. 2. The scheme includes an autothermal reforming reactor R101, a system of heat exchange equipment for cooling synthesis gas and generating steam in a boiler E101 with a steam collector D101, heating a vapour-gas mixture, feed gas and oxygen in heat exchangers E102–E104, heating feed and demineralized water in heat exchang-

ers E102, E104 and final cooling of the converted gas in a water cooler E107. The condensate is separated in separators V101, and V102. The boiler water treatment system includes a deaerator D102 and a feed water pump P101.

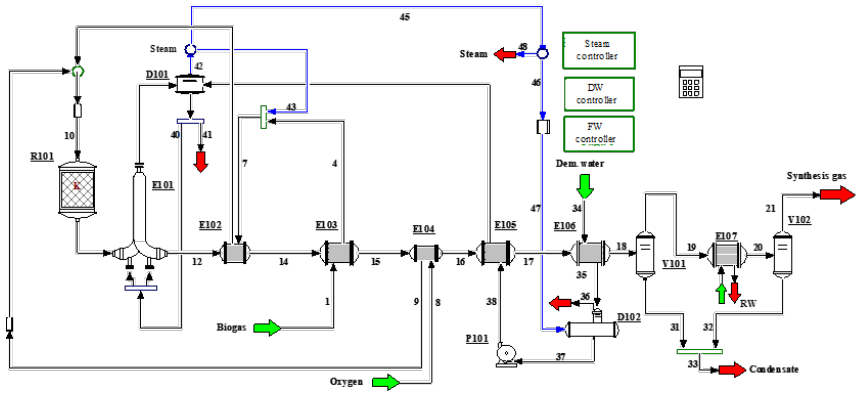

Fig. 2. The autothermal reforming stage calculation scheme.

To analyse the operating modes of methanol production with biogas conversion by steam reforming, a design scheme was developed for the conversion stage with a tubular methane conversion reactor with fired heating of the working mixture. The scheme is shown in Fig. 3.

The scheme includes F101 tubular reactor, in which the conversion of biogas into synthesis gas takes place due to the heat of flue gases, a block of heat-using equipment (E101-E106) used to utilise the heat of flue gases to heat process streams and generate low-pressure steam, heat exchange equipment on the line converted gas E107-E111 for heat recovery, heating of process streams and generation of medium pressure steam.

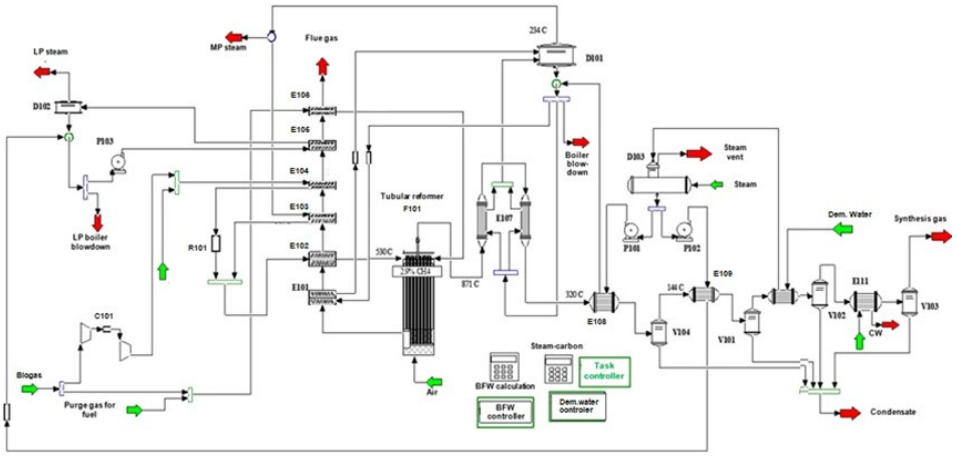

Fig. 3. The biogas steam reforming stage calculation scheme.

3. RESULTS AND DISCUSSION

The analysis of the methanol production technology from biogas was carried out by modelling the stationary operating modes of the scheme for the following conditions: synthesis pressure 80 atm., circulation ratio from 3 to 6.9, and space velocity from 2400 h^{-1} to 6000 h^{-1}. Biogas was used as feedstock in 1000 Nm^3/h (CH_4 60% by volume, CO_2 40 % by volume). To analyse the consumption coefficients, the need for steam is taken into account both for the conversion of biogas and as a heat carrier for rectification. Steam consumption for rectification is used in the amount of 2500 kg of steam per 1000 kg of methanol. It is taken into account that steam is also produced in the synthesis section, and the production of the missing amount of steam will require additional biogas for fuel.

The dependence of technological parameters on the degree of purification of biogas from carbon dioxide was determined during the computational experiment. The modelling of the process was carried out for two variants of the biogas conversion stage: the autothermal method and the steam reforming method. To estimate the composition of the synthesis gas, the following criteria were used:

$$F=\frac{X_{H2}-X_{CO2}}{X_{CO2}+X_{CO}},$$

where X_{H2}, X_{CO2}. X_{CO} – volume concentrations of H_2, CO_2 and CO. If the functional F takes values close to 2, then the composition of the synthesis gas is optimal from the point of view of methanol synthesis [9].

The results are presented in Tables 1 and 2 for autothermal reforming and steam reforming, respectively. The dependence of plant performance indicators depending on the degree of biogas purification is presented, as well as a quantitative assessment of the ability to sequester carbon.

Table 1. Dependence of Process Parameters on CO2 Content in Biogas for Autothermal Conversion Reforming

	CO_2, %vol	Criteria F	Rate of biogas per kg. CH_3OH, m^3/kg	CH_3OH output per m^3 of biogas, kg/m^3	C bounding, %
1	40	0.7	1.598	0.625	43.8
2	25	1.15	1.442	0.693	48.5
3	15	1.438	1.392	0.718	50.3
4	10	1.583	1.378	0.725	50.7
5	5	1.727	1.373	0.728	50.9
6	0	1.872	1.368	0.731	51.1

Table 2. Dependence of Process Parameters on CO2 Content in Biogas for Steam Reforming

	CO_2. %vol	Criteria F	Rate of biogas per kg. CH_3OH, m^3/kg	CH_3OH output per m^3 of biogas, kg/m^3	C bounding, %
1	40	1.33	1.563	0.640	44.8
2	30	1.74	1.538	0.650	45.5
3	25	1.947	1.532	0.653	45.7
4	20	2.15	1.543	0.648	45.3
5	15	2.36	1.562	0.640	44.8
6	10	2.59	1.579	0.633	44.3
7	0	3.01	1.609	0.623	43.5

A comparison of autothermal reforming with a steam reforming process is shown in Fig. 1. The dependence of the amount of methanol produced per unit of time on the degree of biogas purification is presented. The influence of additional factors related to the consumption of biogas for fuel and the production of steam for rectification was not taken into account. Figure 1 serves as an illustration for comparing the chemistry of processes. Of practical importance is the comparison of the specific characteristics of production facilities implemented by different methods. Thus, Fig. 2 shows the cost of biogas per unit of methanol produced, taking into account the cost of fuel and steam generation for rectification. Unlike Fig. 1, an analysis of flow coefficients shows that autothermal reforming is more economical. However, in addition to the cost factors, the capital costs necessary for the implementation of the project are of great importance for the technology.

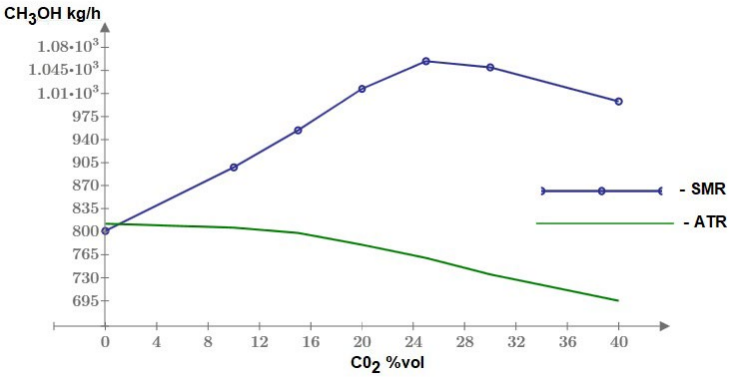

Fig. 1. Methanol production from 1000 m^3 of biogas depending on the degree of biogas purification (excluding biogas consumption for fuel and steam generation for rectification). SMR steam reforming. ATR – autothermal reforming.

Capital cost differences for the considered conversion methods are the presence of an oxygen plant and a more complex CO2 removal unit for autothermal reforming, and a simpler CO2 removing and a rather complex and expensive conversion reactor for steam reforming.

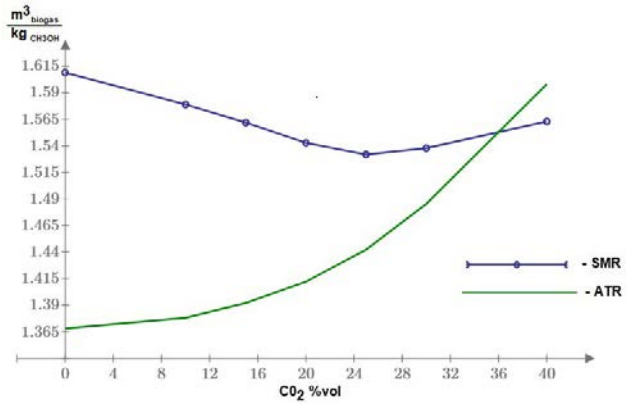

Fig. 2. Specific consumption of biogas for the production of 1 kg of methanol, taking into account the consumption of biogas for fuel and steam generation for rectification. SMR steam reforming. ATR – autothermal reforming.

The scope of this work does not include an analysis of capital and operating costs. In the literature [10], one can find evidence that the pros and cons of autothermal and steam reforming methods, with certain technical solutions, can compensate each other. For compact plants with a capacity of up to 5 thousand tons of methanol per year with autothermal reforming, such solutions are very attractive and lie mainly in the field of separation technologies. However, the technical issues of the implementation of the reactor are of great importance. Thus, high demands are for the homogeneity of the resulting reaction mixture to the reactor mixing unit. The development of such a mixer is the subject of permanent research. In this field, methods for the numerical solution of hydrodynamic equations have recently been widely used to develop and optimise such devices. An example of such a study can be found in [11].

4. CONCLUSIONS

The results of the work allow us to compare two methods of obtaining synthesis gas for methanol production and evaluating the effect of residual CO_2 after biogas purification on the productivity of methanol synthesis. Based on the data presented in Fig. 1 it can be concluded that in the case of autothermal reforming, it is necessary to completely remove CO_2 from biogas. While in steam reforming, there is maximum productivity at a carbon dioxide content of the order of 25 % vol.

Conclusions about the availability of one or another biogas conversion method for a particular production must be made on a comprehensive basis, depending on the technological conditions in the course of a feasibility study.

Another important aspect of methanol production has been considered in this paper. As already mentioned, the technology for the production of methanol from biogas makes it possible to bind carbon and remove it from cyclic circulation in nature. Analysis of the simulation results has shown that steam reforming allows you to bind up to 45 % of carbon in the original biogas, and the method of autothermal reforming over 50%. Thus, both methods have attractiveness in terms of combating climate change.

ACKNOWLEDGEMENTS

The research has been funded by the European Regional Development Fund under the contract “Development of Syngas Production Method for Innovative Methanol Obtainment in Compact Plant Using Mathematical Modelling of Technological Processes” (project number: 1.1.1.1/20/A/110).

REFERENCES

1. Ghosh, P., Shah, G., Sahota, S., Singh, L., & Vijay, V.K. (2020). *Bioreactors, Sustainable Design and Industrial Applications in Mitigation of GHG Emissions.* Amsterdam: Elsevier.
2. Houdkova, L., Boran, J., & Pecek, J. (2008). Biogas: A Renewable Source of Energy. *Therm. Sci., 12* (4), 27–33.

3. Redlich, O., & Kwong, J. N. S. (1949). On the Thermodynamics of Solutions. *Chem. Rev., 44* (1), 233–244.
4. Leibush, A., Semenov, V., Kazarnovsky, Y., & Karhov, N. (1971). *Process gas production for the synthesis of methanol and ammonia from hydrocarbon gases*. Moscow: Chemistry [in Russian].
5. Stepanov, A. (1982). *Hydrogen and hydrogen-containing gases production.* Kyiv: Nauk. Dumka.
6. Conesa, J. A. (2020). *Chemical Reactor Design (Mathematical modelling and application)*. Wiley-VCH Weinheim, Germany.
7. Rozovskii, A. Ya., & Lin, G. I. (2003). Fundamentals of Methanol Synthesis and Decomposition. *Top. Catal., 22*, 137–150.
8. Xu, J., & Froment, G.F. (1989). Methane Steam Reforming, Methanation and Water-Gas Shift: I. Intrinsic Kinetics. *AIChE Journal., 35*, 88–96.
9. Karavaev, M.M., Shepelev, E.T., Leonov, V.E., & Popov, I.G., (1984). *Tekhnologiya sinteticheskogo metanola (Synthetic Methanol Technology)*. Moscow: Khimiya.
10. Noelker, K., & Johanning, J. (2010). Autothermal reforming: A flexible syngas route with future potential. In *NITROGEN & SYNGAS Int. Conf.* 28 February–3 March 2010, Bahrain.
11. Klevs, M., Geza, V., Jakoviès, A., & Rodin, L. (2023). Optimization of the performance of a cross-flow gas mixer for a partial oxidation reactor through numerical modelling. In *CONECT 2023 XVI International Scientific Conference of Environmental and Climate Technologies*. 10–12 May 2023, Riga: Riga Technical University.

sciendo

LATVIAN JOURNAL OF PHYSICS
AND TECHNICAL SCIENCES
2023, N 6

DOI: 10.2478/lpts-2023-0044

NUMERICAL INSIGHTS INTO GAS MIXING SYSTEM DESIGN FOR ENERGY CONVERSION PROCESSES

M. Klevs, G. Zageris, A. A. Ziemelis,
V. Dzelme, V. Geza*, A. Jakovics

Institute of Numerical Modelling, University of Latvia
3 Jelgavas Str., Riga, LV-1004, LATVIA
*e-mail: vadims.geza@lu.lv

Uniform gas mixing is important in various scientific and engineering domains, particularly in a chemical reactor design employing pre-mixed gases for processes. Assessing the performance of different mixer designs through physical prototypes can be resource-intensive and time-consuming. Consequently, this study underscores the significance of numerical simulations to optimize gas mixing and distribution systems in energy conversion applications.

The research primarily focuses on varying the base mixer geometry by modifying the configuration of cross-flow inlets alongside the chambers. By employing numerical simulations, critical factors influencing mixing uniformity are identified, and innovative solutions are proposed to enhance system performance. Additionally, this work extends its application to improving the operational conditions of an industrial biomass gasifier, underlining the practicality of numerical modelling in addressing complex engineering challenges.

Keywords: *Computational fluid dynamics, gas mixing, partial oxidation, syngas production.*

1. INTRODUCTION

Gas mixing devices play a crucial role in various chemical reactor designs, particularly in the production of synthesis gas, which finds applications in hydrogen production, methanol and DME synthesis, and synthetic fuel production [1]. Synthesis gas production methods often involve partial oxidation (POX) of natural gas or hydrocarbon feedstocks [2] [3], which can be either non-catalytic or catalytic, including autothermal reforming (ATR).

While biomass gasification and POX

differ in many aspects, they share common requirements for oxidizer input and gas mixing. The issue of slag formation in gasification, caused by ash deposits on gasifier walls, poses challenges to equipment production [4]. Despite its significance, the phenomenon of slagging remains insufficiently explored, especially concerning its link to the gas flow behaviour. Most modelling attempts look at one or two-dimensional models [5], thus not taking into consideration important spatial behaviour of the slagging process.

In all of these syngas production types, the mixing device is an important part of the equipment, regardless of what type of process is implemented in a particular case, catalytic or in free volume, and in what ratio the initial components react. Its development is always accompanied by special studies [6], and the results are protected by copyright.

In POX processes, the risk of free carbon formation is associated with localized changes in reactant concentrations, especially when it comes to the partial oxidation of natural gas, rather than pure methane. C2+ hydrocarbons contained in natural gas are more likely to produce soot than pure methane [7]. Another problem is that in order to achieve an optimal ratio of H_2:CO:CO_2 in the resulting mixture used for further processing (e.g. methanol synthesis), the original mixture must have a small oxidant:fuel ratio [8]. In this case, the mixture becomes difficult to ignite, and the presence of local irregularities in the composition as a result of poor mixing can lead to zones where reactions do not occur.

Catalytic POX of natural gas also requires uniform mixing of feedstocks. This is due to the fact that, in contrast to non-catalytic oxidation and ATR conversion, after mixing, the gas does not ignite, but enters the catalyst, where oxidative conversion occurs. In the case of inhomogeneous mixing, spontaneous ignition may occur [9]. The probability of this increases due to the high temperatures of the source gases. Spontaneous ignition after mixing can lead to soot formation and deterioration of the catalyst, on the one hand, and to a violation of the technological regime and stopping the unit, on the other. Also, homogeneous mixing leads to stable operation of the catalyst without local overheating.

Thus, the main task of the mixing device simulation is to optimize the mixing unit to produce a homogeneous flow after mixing. This raises the problem of determining the mixer optimality criterion. This raises the question of what constitutes an acceptable concentration gradient and what does not. The solution to this challenge seems to be a comparative analysis of different design options and the choice of the least concentration gradient. The technical characteristics of the mixer, such as the length of mixing tubes, their diameter, diameter and arrangement of injection holes, and other parameters, should be independent variables of this optimization task. Besides optimal mixing, it is also important that the mixing device generates hydraulic resistance that does not exceed the limits imposed by other reactor components.

The other device considered in this paper is a ring collector in biomass gasification equipment. Here we take a closer look at the impact of gas input to the gasifier and the role of asymmetry of the flow through the inlets in slag formation. This study has been done in partnership with a company that experienced problems with asymmetrical slag formation in their gasification, thus the study is done in the scope of their gasification apparatus. This puts very tight constraints on what can be changed in the existing geometry.

2. OVERVIEW OF THE GAS MIXING SYSTEMS

2.1. Chambered Gas Mixer

The gas mixer is located above the reactor and consists of several chambers. The mixing takes place in several small vertical pipes where one gas is passed at the start of the pipe and the rest of the gases are added through small holes on the sides of the pipes.

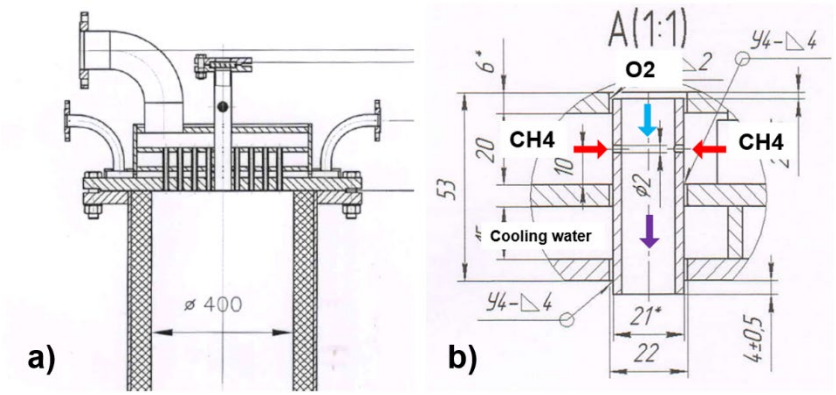

Fig. 1. Cross section of the gas mixer on top of the reactor: a) full view, b) close-up of a single pipe.

Figure 1a shows the cross section of the examined methane-oxygen mixer. Figure 1b shows an illustrative example for how a cross section of a single pipe can look like for a two-gas mixer. The two perpendicular flows create turbulence in the pipe flow that mixes both gases while they travel down the pipe. These pipes lead directly into the reactor where the mixed gases react with each other. The mixer is intended to mix steam, oxygen and methane and distribute the mixture in the reactor. The goal of the parameter study is to maximize the uniformity of the mixed gases at the exit of the mixer. The optimizable parameters are the number of injection holes at the top and bottom chambers and the angles of the holes (more detailed description in Section 4).

2.2. Ring Collector

The gas collector is a gas injection part of an approximately eight meters high industrial entrained flow gasifier with dimensions, inlet pipe positions and inlet parameters taken from the technical specification of the gasifier. During the study, it was determined that the gas flow characteristics would be the ones that would eventually determine the presence of asymmetrical slag. Therefore, modelling of particle-gas reactions has been neglected, deeming gas-gas reactions in the gasifier as sufficient to give a representative picture of the flow. This assumption is eventually verified by comparisons with the real-life gasifier data. Furthermore, we only consider the area around the inlets, neglecting parts above it. The geometry is given in Fig. 2.

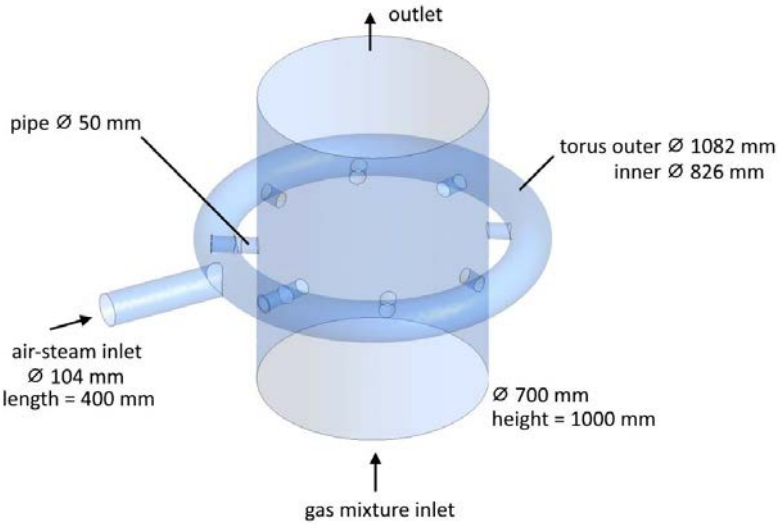

Fig. 2. A sketch of the ring collector model.

At the bottom of the model in Fig 2, a gas mixture (CO – 45 %, N_2 – 26 %, CO_2 – 16 %, H_2O – 6 %, CH_4 – 6 %, H_2 – 1 %) at 873 °C is introduced at a constant mass flow rate consistent with operating conditions. This gas flow drives the co-current flow of the gasifier. Additionally, a mixture of air and steam is introduced at 1073 °C from the pipe that connects to the collector ring, also at a constant mass flow rate. The mixing of these two flow sources and the resultant velocity field determines the flow through the gasifier, modelled as the cylinder in the middle. The collector ring has eight symmetrically located inlet pipes that connect to the gasifier. These pipes will be subject to modifications throughout the study.

3. DESCRIPTION OF THE MATHEMATICAL MODEL

3.1. Governing Equations

The dynamics of the gas flow is described by the compressible Navier Stokes equation:

$$\frac{\partial}{\partial t}\rho\vec{u} + \nabla\cdot(\rho\vec{u}\otimes\vec{u}) = \nabla\cdot\left(\mu\left(\nabla\vec{u} + (\nabla\vec{u})^T - \frac{2}{3}(\nabla\cdot\vec{u})I\right)\right) - \nabla p + \rho\vec{g},$$

where ρ – density, $\vec{u}$ – velocity, μ – dynamic viscosity, p – pressure, $\vec{g}$ – acceleration of gravity, I – identity tensor. Here we use the Stokes hypothesis where the bulk viscosity is set to zero. The gas density is calculated by using the ideal gas relation:

$$\rho = \frac{1}{RT} p,$$

where R – ideal gas constant, T – temperature, p – pressure. The inlet gases are expected to be at different temperatures; therefore, the temperature is also solved by using an energy transport equation. The gas species are transported, and they experience turbulent mixing. The diffusivity of the gases is taken as a sum of the regular diffusivity and turbulent diffusivity that is calculated using a turbulence model. The gas species are transported by using a transport equation that uses the flow velocity.

3.2. Numerical Models

3.2.1. Ring Collector Model

Calculations for the ring collector were done by using ANSYS Fluent 18. The gases were modelled as ideal gases, where the viscosities, diffusivities, thermal conductivities, specific heats, and molar masses were taken from the built-in Fluent database. Turbulence was modelled using the model.

For the ring collector model, chemical reactions of the gas are also considered, with the reaction rates determined by the Arrhenius equation. A summary of the chemical reactions is given in Table 1.

In this model, temperature iso-surfaces are examined to estimate the reaction fronts, with the aim of characterising slag deposition.

Table 1. Summary of Chemical Reactions Implemented in the Ring Collector Model

Reaction type	Reaction equation	A	E, J/kmol	Reference
volumetric	$CO + 0.5O_2 \rightarrow CO_2$	2.239×10^{12}	1.67×10^{8}	[12]
volumetric	$CO + H_2O \rightarrow CO_2 + H_2$	9.87×10^{8}	3.1×10^{7}	[13]
volumetric	$CO + 3H_2 \rightarrow CH_4 + H_2O$	5.12×10^{-14}	2.73×10^{4}	[2]
volumetric	$H_2 + CO_2 \rightarrow CO + H_2O$	1.785×10^{12}	3.26×10^{8}	Equilibrium with reaction #2
volumetric	$CH_4 + 1.5\ O_2 \rightarrow CO + 2H_2O$	5.012×10^{11}	2×10^{8}	[14]
volumetric	$CH_4 + H_2O \rightarrow CO + 3H_2$	5.922×10^{8}	2.09×10^{8}	[15]

3.2.2. Gas Mixer Model

Preliminary calculations for the gas mixer were also performed using ANSYS Fluent 18. $k-\epsilon$ turbulence model was used for the steady-state calculations and Large Eddy Simulation (LES) [10] with the WALE sub-grid model [11] for transient simulations.

The model of gas mixer was also implemented in OpenFOAM-v2112 [16], which is an open-source library that specialises in modelling fluid dynamics. It uses the finite volume method to discretize the governing equations. The *reactingFoam* module is used as the solver for the fluid flow, with the combustion disabled. This solver is used because it can model turbulent mixing for any number of gases. The viscosity of each species is calculated by using a variation of the Sutherland's law:

$$\mu = \frac{A_S\sqrt{T}}{1+T_S/T},$$

where A_S – Sutherland coefficient, T_S – Sutherland temperature. The coefficients

were calculated by using the least-squares regression for the viscosity formula, where the ground truth data was taken from the NIST Chemistry webbook [17]. The specific heat of each species is calculated by using the JANAF thermochemical data [18] where the coefficients are taken from the GRI-mech 3.0 [19]. Thermal conductivity is calculated using the Eucken approximation [20]:

$$\kappa = \mu \cdot C_v \cdot \left(1.32 + 1.77 \cdot \frac{R}{C_v}\right),$$

where κ – thermal conductivity, C_v – specific heat.

The sub-grid turbulence was modelled using the LES k-equation model [21]. The species transport equation has a turbulent diffusion term that uses the turbulent viscosity as the local turbulent diffusivity value.

In this model, various types of standard deviations (which will be described in the next chapter) are being utilized to characterise the quality of mixing.

4. RESULTS OF THE MIXER MODEL

The first section of this chapter provides an overview of the standard deviation types used in the analysis of our study results. Next sections describe the results of the numerical simulations for two and three gas mixing cases. The last section of this chapter attempts to analyse the varying levels of mixing efficiency observed within the context of our research.

4.1. Description of the Standard Deviation Types

There are different standard deviation types used across the results sections of the gas mixer model. Here they are briefly defined. The regular mean is defined as

$$\bar{x} = \frac{\sum_i^N x_i}{N},$$

where x_i – field value, N – number of values. The regular standard deviation is defined as

$$\sigma = \sqrt{\frac{\sum_i^N (x_i - \bar{x})^2}{N-1}},$$

where $\bar{x}$ – the regular mean, N – number of values. The area-weighted mean is defined as

$$\bar{x}_w = \frac{\sum_i^N a_i x_i}{\sum_i^N a_i},$$

where x_i – the field value in the i-th cell, a_i – the cell area, N – the number of cells. The area-weighted standard deviation is defined as

$$\sigma_w = \sqrt{\frac{\sum_i^N a_i (x_i - \bar{x}_w)^2}{\frac{M-1}{M}\sum_i^N a_i}},$$

where $\bar{x}_w$ – area-weighted mean, M – the number of non-zero-weights (cell areas). In our case there are no non-zero weights; therefore, M is equal to N.

The gas concentration data is sampled on OXY planes that slice the pipe. The mixing uniformity is quantified in three ways:

The mean value of the spatial standard deviation at each point in time:

$$\frac{1}{K}\sum_j^K \sigma_w^j,$$

where j – timestep index, K – the number of timesteps, σ_w^j, the area-weighted standard deviation for the j-th timestep.

The regular standard deviation for the area-weighted spatial mean in each point in time:

$$\sqrt{\frac{\sum_j^K \left(\overline{x}_w^j - \overline{x}_w^*\right)^2}{K-1}},$$

where j – the timestep index, K – the number of timesteps, $\bar{x}_w^*$ – the mean value of the weighted spatial mean over all timesteps.

The area-weighted mean value of the regular standard deviation of over time for each cell:

$$\frac{1}{\sum_i^N a_i}\sum_i^N\left(a_i\sqrt{\frac{\sum_j^K\left(x_i^j - \bar{x}_i\right)^2}{K-1}}\right),$$

where j – timestep index, K – number of timesteps, $\bar{x}_i$ – the mean value over time for the i-th cell, x_i^j – the value in the i-th cell in the j-th timestep.

4.2. Mixing of Two Gases

The full gas mixer has a geometry with many places that require a high-resolution mesh to accurately model the fluid flow. The mixing process takes place in many identical pipes (Fig. 1a); therefore it was decided to examine a single one of these pipes (Fig. 1b) instead of the whole reactor. From the geometry of the mixer, it is expected that the pressures near the inflows of the pipes are very similar for each pipe. This leads us to the belief that all these pipes behave in a similar way, which justifies considering only one pipe.

In the geometry shown in Fig. 3d, there are two gases that are introduced. Before modelling the mixing of three gases it is useful to see the qualitative behaviour of the mixing of two gases. Oxygen is injected through the top part of the central cylinder, and methane is injected from the outer surface of the surrounding chamber. The outlet is the bottom surface of the central cylinder.

The initial calculations presented in Figure 4 were done in ANSYS Fluent. Figure 4 shows a comparison of a steady state solution and a snapshot of a transient solution using LES, where both cases have the same flow parameters. There are clear differences between both cases – the steady state solution shows that both gases mix quickly and have a very uniform distribution in the pipe, however the transient solution shows that there are turbulent pulsations near the top that cause the concentrations to fluctuate both in the transverse and lengthwise directions. This comparison demonstrates that steady state RANS models overestimate the uniformity of mixing, because they do not account for transient changes in velocity and concentration.

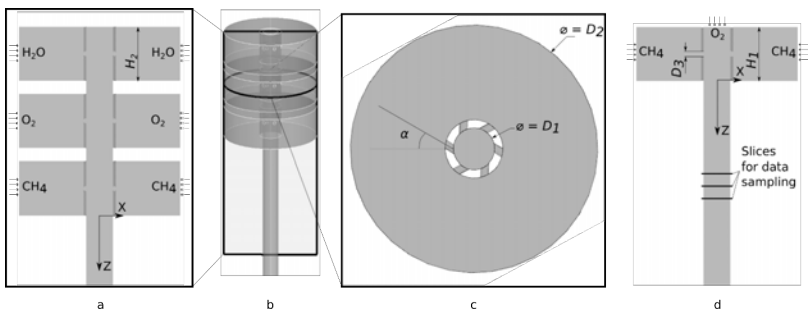

Fig. 3. Simulation domain for a single mixer pipe with 6 holes: a) three gas model, vertical cross section, b) three gas model, 3D view, c) three gas model, horizontal cross section, d) two gas model, vertical cross section. D_1 = 18 mm, D_2 = 60 mm, D_3 = 2 mm, H_1 = 20 mm, H_2 = 40 mm. Drawings are not to scale.

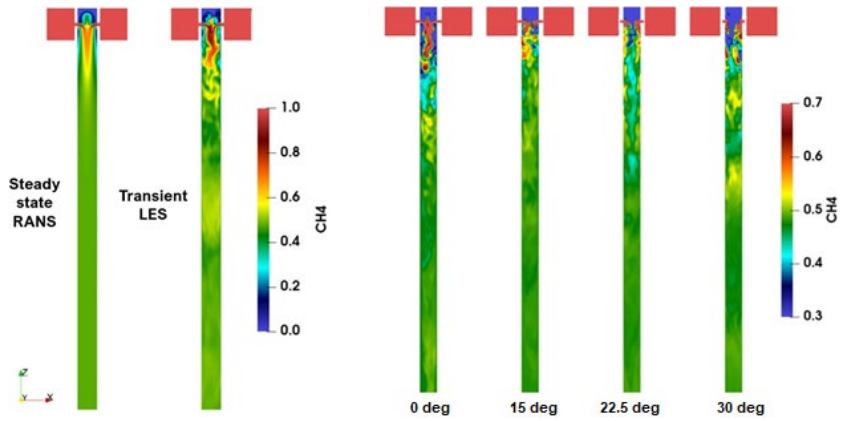

Fig. 4. On the left: Comparison between the CH_4 mass fraction in a vertical cross section for solutions in ANSYS Fluent: a steady state RANS () solution and a transient LES solution at a randomly chosen timestep. On the right: Comparison between CH_4 mass fractions in a vertical cross section for transient LES simulations in OpenFOAM for different hole angles for 6 holes: 0 degrees, 15 degrees, 22.5 degrees, 30 degrees.

It is important to note that the mixing takes place not only inside the mixer zone, but all the way further down the central pipe. The gas flow is highly turbulent which leads to intense mixing. Figure 5 shows the relative standard deviations for different distances from the bottom chamber. The distance from the bottom chamber is the Z coordinate shown in Fig. 3. As expected, the mixture becomes more uniform as it flows down the pipe and mixes due to the turbulence. The highest of the observed deviation types is the temporal, meaning that changes over time are more pronounced than over cross section of the main pipe. For this case, the data were collected starting from distance of 10 cm from the bottom chamber. The variations are below 3 % for all deviation measures at the distance of 10 cm.

It is also useful to see whether the angle of the holes influences the result in a meaningful way. The azimuthal hole angle is taken as the angle between the axis of the hole and normal of the main cylinder surface (α in Fig. 3c). Here the hole positioning stays the same, but each of the cylindrical holes gets rotated in place. Figure 4 (right) shows snapshots of transient simulations for varying azimuthal hole angles.

The data are sampled on an OXY plane that slices the pipe 15 cm below the last chamber (see Fig. 3d). The mixing uniformity is quantified in three ways which have been described in the previous section.

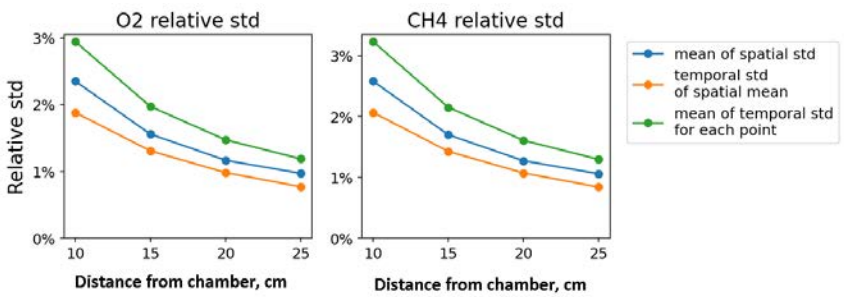

Fig. 5. The relative standard deviations for the O_2 and CH_4 mass fractions at horizontal section planes at different distances from the bottom chamber. The two gas mixer.

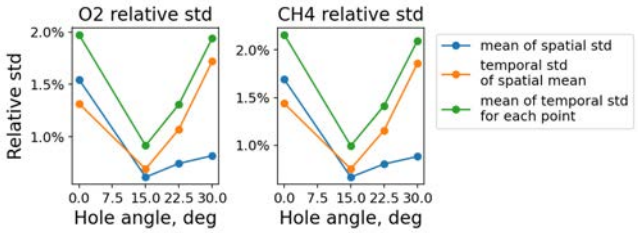

Fig. 6. The relative standard deviations for the O_2 and CH_4 mass fractions at the section plane for a varying azimuthal angle.

Figure 6 shows the relative standard deviations for varying azimuthal angles. It is noticeable that there is a clear optimal angle at which all of the standard deviations of the methane mass fraction are the lowest. Increasing the angle further leads to poorer mixing, which can be explained by the fact that a larger angle directs the injected gas more towards the outer part of the pipe. If the angle is too large, then the injected gas gathers on the outer part of the pipe which leads to less mixing.

4.3. Mixing of Three Gases

The full mixer geometry mixes three gases – steam, oxygen and methane. Figure 3 a-c shows the geometry of a mixer pipe for three gases. Steam flows in through the top chamber, oxygen flows through the middle chamber and methane flows through the bottom chamber. Unlike before, the topmost gas is pumped in through a chamber that is directly connected to the central pipe.

The initial geometry starts with 6 evenly spaced holes that are perpendicular to the cylinder for both the middle and bottom chambers. The data are sampled the same way as in the two-gas case. To see how the length of the mixing pipe influences the result, the data were sampled on multiple OXY slices at different distances from the last chamber.

Figure 7 shows the relative standard deviations for the different distances from the last chamber. As expected, the mixture becomes more uniform as it flows down the pipe and mixes due to the turbulence. The distance of interest for our mixer geometry is 15 cm; therefore, the optimisation will be based on the values at that slice. It is expected that the optimum mixer shape for the slice at 15 cm will also be the optimum mixer shape for distances further along the pipe.

For the three gas mixer the spatial deviation dominates over temporal deviation. It is mostly visible at the beginning of the main pipe, close to bottom chamber. The difference to two gas mixing model, where temporal deviation dominates, is likely due to different gas inflow conditions. For the two gas mixer, O_2 was supplied from the top face of the model, whereas in three gas model – via middle chamber.

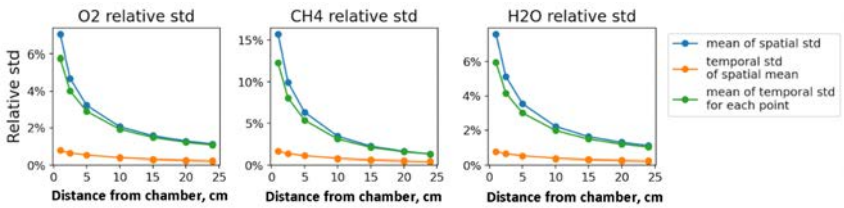

Fig. 7. The relative standard deviations for the O_2 and CH_4 mass fractions at horizontal section planes at different distances from the bottom chamber. The three gas mixer.

It is expected that the number of holes at the bottom chamber plays the biggest role on the mixing because it is at the point where all three gases meet. The number of holes is also inversely proportional to the cross-flow jet velocity which in turn influences the distribution of gases and the turbulence in the central pipe near holes. The number of holes on the bottom chamber is varied from 3 to 8.

Figure 8 shows the relative standard deviations for the number of holes at the bottom chamber. For 5 holes, the spatial relative standard deviations are at a minimum. The temporal relative standard deviations decrease until 5 holes and have negligible changes for larger hole counts. Next the number of holes on the top chamber are varied from 3 to 12. The flow near the top holes is expected to be slower than the flow at the bottom holes; thus, more holes might be needed to reduce the cross-flow velocity.

Figure 9 shows the relative standard deviations for the number of holes at the top chamber. The results are less clear than for the bottom holes as there is no clear minimum across the three gases. The spatial standard deviation changes unpredictably, with a slight positive trend, and the temporal standard deviations increase if the number of holes is too small. A value of 6 holes is chosen as an optimal value, judging from the O_2 and H_2O (steam) graphs. The CH_4 standard deviations are less affected by varying the number of holes, which is explained by the fact that it is being injected by the holes at the bottom chamber and not at the top.

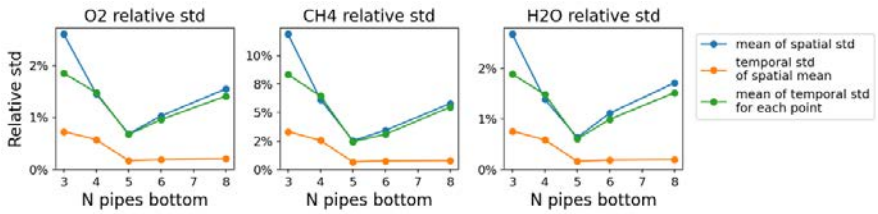

Fig. 8. The relative standard deviations for the O_2, CH_4 and H_2O (steam) mass fractions at the section plane for varying number of holes for the bottom chamber.

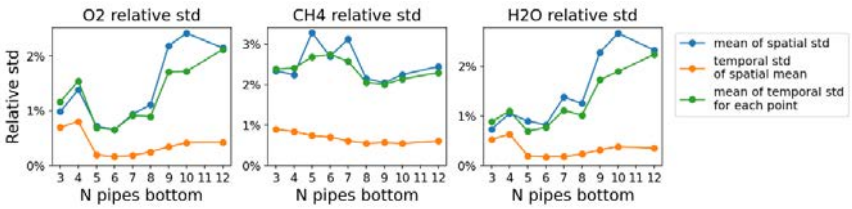

Fig. 9. The relative standard deviations for the O_2, CH_4 and H_2O (steam) mass fractions at the section plane for varying number of holes for the top chamber.

Comparing the effects of the number of holes at the bottom and top chambers it is apparent that the bottom number of holes has much greater effect on the mixing uniformity. This can be explained by the fact that the introduced CH_4 cross-flow is also surrounded by partially mixed H_2O and O_2 that are then mixed a second time. The bottom cross-flow essentially mixes all three gases instead of just two.

Figure 10 shows the relative standard deviations for varying azimuthal angles of

the holes at the bottom chamber. The results show that increasing the azimuthal angle reduces the mass fraction standard deviations for all three species, and for large angles above 45 degrees the standard deviation increases again. The measured differences for varying angles are only within one percent. Compared to varying the number of holes, varying the azimuthal angle of the holes gives a smaller effect on the mixing uniformity. This might be because the optimum number of holes for the top and bottom chambers has already been chosen, thus varying the azimuthal angle at a chamber gives less of an improvement.

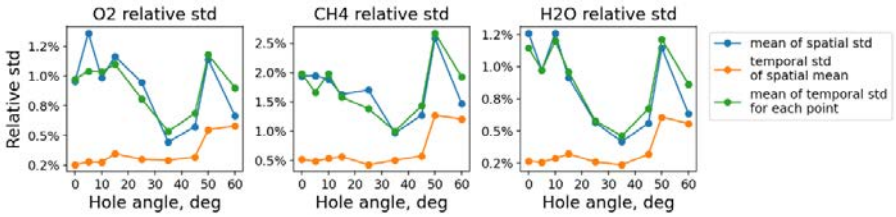

Fig. 10. The relative standard deviations for the O2, CH4 and H2O (steam) mass fractions at the outlet for varying azimuthal hole angles at the bottom chamber.

4.4. Discussion on the Different Mixing Efficiencies

Figure 11 shows iso-contours for methane for the mixer with 3, 5 and 8 holes. The key difference is that the number of holes influences the velocity at which the gas gets injected into the central pipe. In the 3-hole case the velocities are large, and the methane gets shot to the centre of the pipe while the other gases flow on the outside. In the 8-hole case the velocities are lower and the methane gets immediately pulled by the other gases downwards while it is still on the outer part of the pipe. In the 5-hole case, the scenario is somewhere in between where methane gets distributed more evenly throughout the volume.

Figure 12 shows iso-surfaces for different hole angles. The angle adds rotation to the flow which can smooth out any radial asymmetries in the concentrations, however making the angle too big will push the gas to the outer wall of the pipe and impede mixing.

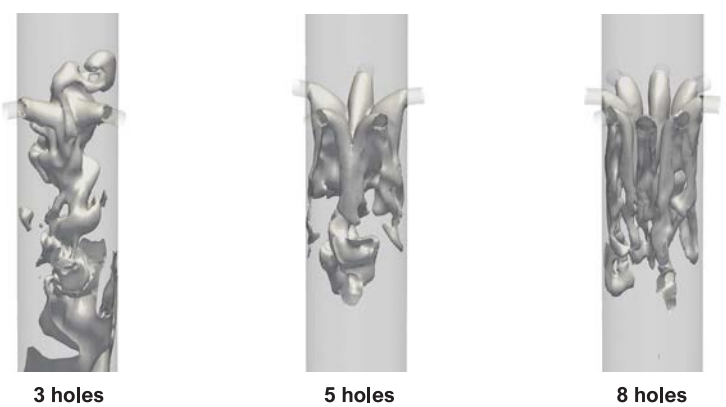

Fig. 11. CH_4 iso-surfaces near the chamber for a different number of holes.

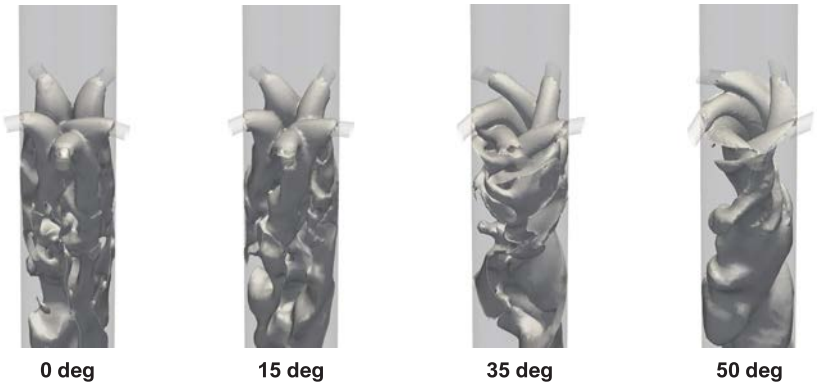

Fig. 12. CH_4 iso-surfaces for different hole angles in the azimuthal direction.

5. RING COLLECTOR RESULTS

At the start, a simulation was run for the default geometry of the gasifier, which simply included eight inlets symmetrically located around the collector ring. As asymmetric slag deposition had been observed in the gasifier, the aim was to determine the cause for this asymmetry. Upon conducting simulations, it was determined that a constant mass flow through the collector pipe did not supply a uniform mass flow throughout the inlet pipes to the gasifier. The inlet pipe numbering and the mass flow distribution is shown in Fig. 13.

One can immediately notice that the flow is severely weaker through inlets 1 and 8. This eventually causes asymmetry in the system, as the remaining inlets push the entire flow towards the wall where inlets 1 and 8 are located. This is well illustrated with the temperature iso-surface in Fig. 14. The iso-surface is tilted towards one side of the gasifier. In terms of slag formation, this is undesirable, as different temperatures along the walls of the gasifier also mean different levels of the ash melting intensity and thus different rates of slag deposition.

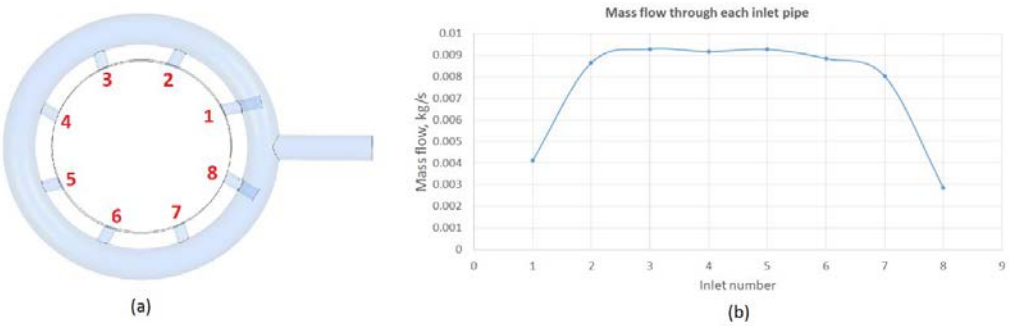

Fig. 13. (a) The numbering convention for inlets, (b) mass flow distribution for the inlet pipes for the default geometry.

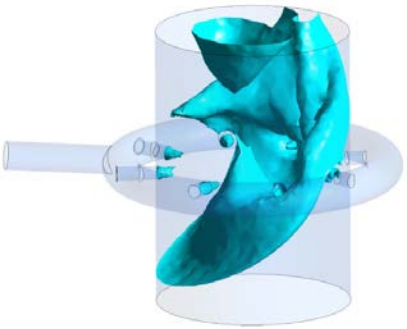

Fig. 14. Temperature iso-surface (900 °C) for the default case.

To combat this, the flow from the inlet pipes should be as close to uniform as possible. In practice, this means modifying the collector ring. The reason for the mass flow rate drop at inlets 1 and 8 is mainly the high velocity of the gas flow that arrives from the main collector pipe. Therefore, the flow before these inlets should be broken up to achieve higher uniformity.

Multiple solutions were tested, and the best results were obtained with one of the two modifications – a small obstacle added to the inner wall of the collector directly before inlets 1 and 8 (Fig. 15a), or the extension of inlet pipes inside the collector with holes inside those extensions (Fig. 15b).

Upon implementing these solutions, the symmetry of the flow improved significantly. Even though the mass flow through the inlets was not entirely uniform, it was markedly improved from the initial case as shown in Fig. 16 b, and the flow was sufficiently symmetrical to no longer have any tilt of the temperature iso-surface (Fig. 16a).

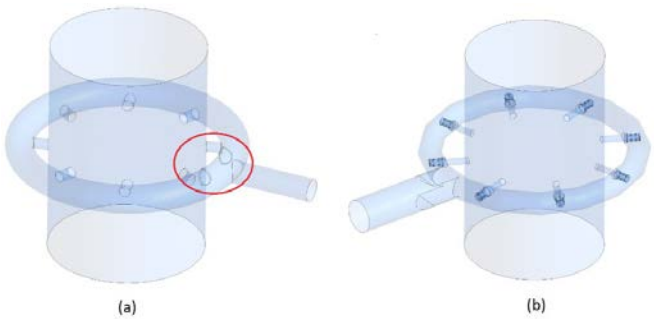

Fig 15. Geometry for (a) an obstacle for collector inner wall, (b) inlet pipe extensions.

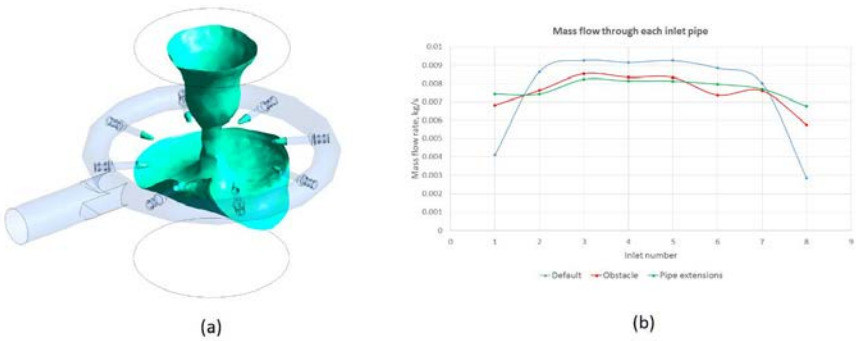

Fig. 16. (a) Temperature iso-surface (900 °C) for the improved geometry, (b) mass flow distributions for the improved geometries in contrast to the default geometry.

The obtained improvements for mass flow distributions can be explained by two factors. In the model with obstacle (Fig. 15a), local high-pressure spots were reduced. These were caused by the fluid flow, which after the 90-degree turn was

pushed towards the region of closest pipes (1 and 8). Obstacles did not allow flow to be pushed towards the pipes, thus improving the uniformity.

The second factor leading to the uniformity of the mass flow through pipes is the ratio of hydraulic resistance of pipes (R_p Fig 17) to that of the collector ring sectors (R_S in Fig. 17). The hydraulic resistance is estimated using an approximation of the Colebrook-White equation developed by Bellos et al. [22]. Here we neglected the relative roughness factor, leaving an expression for smooth pipes:

$$f = \left(\frac{64}{Re}\right)^{a}\left(0.75\ ln\left(\frac{Re}{5.73}\right)\right)^{2(a-1)}$$

$$a = \frac{1}{1+\left(\frac{Re}{2712}\right)^{8.4}},$$

where f is the friction factor in the equation for head loss:

Using these data, the ratio R_p/R_S = 0.602, meaning that the hydraulic resistance of the sector is larger than that of the pipe. The pipe extensions increase the length and decrease the diameter of the pipe, leading to the increased ratio R_p/R_S = 3.680.

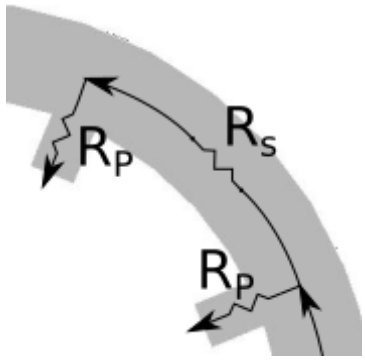

Fig. 17. Schematic illustration of hydraulic resistances in the collector ring model. R_s is the resistance to flow along one sector of the ring. R_p is the resistance of one pipe.

Eventually, the solution with pipe extensions was implemented in the real-life version of the gasifier. After running a test with the new inlet configuration, it was indeed determined that asymmetrical slagging had significantly decreased. This proves the premise that the flow regime was what caused the asymmetrical slagging in the first place, and that ensuring a uniform flow through the inlets is crucial to prevent undesirable slagging.

6. CONCLUSION

In summary, this research underscores the effectiveness of numerical simulations in explaining the flow characteristics within gas mixing systems crucial for energy conversion processes. The following aspects have been concluded during this study:

1. The study has exposed the limitations of steady-state RANS models in assessing gas mixing uniformity. These models, by neglecting transient flow changes, can overestimate the mixing uniformity, failing to capture the dynamic variations in local gas concentrations over time.
2. Critical factors affecting gas mixing uniformity have been identified – the number of holes along the mixing pipe's circumference and the azimuthal angle of these holes relative to the central cylinder. The number of holes impacts the cross-flow velocity, while the azimuthal angle influences gas distribution within the cross-flow region.

3. The gas mixer model has revealed that mixing occurs along the pipe length, with turbulence introduced at the holes near chambers enhancing uniformity. It is important to note that the pipe length must be carefully considered, as overly short pipes may yield uneven mixtures, while longer ones often face design constraints.
4. Contrasting the idealised gas mixer model, the industrial ring collector calculation has shown varying flow rates through the holes. Importantly, we have demonstrated that solving these issues can be accomplished without major equipment modifications.
5. For the ring collector, it has been concluded that the asymmetrical slag deposition can be sufficiently explained by the asymmetrical flow of the gas in the gasifier and gas-gas reactions. Particle-gas reactions were observed to have a relatively minor impact, with flow characteristics playing a more dominant role in this asymmetrical slag deposition. It has also been shown that ensuring the hydraulic resistance of pipes to be larger than that of the collector ring can enhance the uniformity of the gas flow.
6. To remove the undesirable asymmetrical slag deposition, it is necessary to construct inlet configurations that promote the axi-symmetrical flow.

ACKNOWLEDGEMENTS

The research has been funded by European Regional Development Fund under contract "Development of Syngas Production Method for Innovative Methanol Obtainment in Compact Plant Using Mathematical Modelling of Technological Processes" (project number: 1.1.1.1/20/A/110).

REFERENCES

7. Aasberg-Petersen, K., Bak Hansen, J.-H., Christensen, T.S., Dybkjaer, I., Seier Christensen, P., Stub Nielsen, C., & Winter, S.E.L. (2001). Technologies for Large-Scale Gas Conversion. *Applied Catalysis A: General, 221* (1), 379–387. https://doi.org/10.1016/S0926-860X(01)00811-0.
8. Bolívar Caballero, J.J., Zaini, I.N., & Yang, W. (2022). Reforming Processes for Syngas Production: A Mini-Review on the Current Status, Challenges, and Prospects for Biomass Conversion to Fuels. *Applications in Energy and Combustion Science, 10,* 100064. https://doi.org/10.1016/j.jaecs.2022.100064.
9. Keiski, R. L., Ojala, S., Huuhtanen, M., Kolli, T., & Leiviskä, K. (2011). Partial Oxidation (POX) Processes and Technology for Clean Fuel and Chemical Production. *Advances in Clean Hydrocarbon Fuel Processing: Science and Technology*, 262–286. https://doi.org/10.1533/9780857093783.3.262.
10. Lu, X., & Wang, T. (2015). Simulation of Ash Deposition Behavior in an Entrained Flow Coal Gasifier. *International Journal of Clean Coal and Energy, 4,* 43–59. https://doi.org/10.4236/ijcce.2015.42005.
11. Bhuiyan, A.A., & Naser, J. (1015). Modeling of Slagging in Industrial Furnace: A Comprehensive Review. *Procedia Engineering, 105*, 512–519. http://dx.doi.org/10.1016/j.proeng.2015.05.084.
12. Christensen, T., & Primdahl, I.I. (1994). Improve Syngas Production Using Autothermal Reforming. *Hydrocarbon Processing*.

13. Wang, Y., Gu, M., Wu, J., Cao, L., Lin, Y., & Huang, X. (2021). Formation of Soot Particles in Methane and Ethylene Combustion: A Reactive Molecular Dynamics Study. *International Journal of Hydrogen Energy, 46* (73), 36557–36568. https://doi.org/10.1016/j.ijhydene.2021.08.125.
14. Cañete, B., Gigola, C.E., & Brignole, N.B. (2014). Synthesis Gas Processes for Methanol Production via CH4 Reforming with CO2, H2O, and O2. *Industrial & Engineering Chemistry Research, 53* (17), 7103–7112. https://doi.org/10.1021/ie404425e.
15. Ma, R., Xu, B., & Zhang, X. (2019). Catalytic Partial Oxidation (CPOX) of Natural Gas and Renewable Hydrocarbons/Oxygenated Hydrocarbons—A Review. *Catalysis Today, 338*, 18–30. https://doi.org/10.1016/j.cattod.2019.06.025.
16. ANSYS. (n.d.). *ANSYS FLUENT 12.0 Theory Guide - 4.11.2 Filtered Navier-Stokes Equations*. Available at https://www.afs.enea.it/project/neptunius/docs/fluent/html/th/node94.htm
17. Nicoud, F., & Ducros, F. (1999). Subgrid-Scale Stress Modelling Based on the Square of the Velocity Gradient Tensor. *Flow, Turbulence and Combustion, 62* (3), 183–200.
18. Westbrook, C.L., & Dryer, F.L. (1981). Simplified Reaction Mechanisms for the Oxidation of Hydrocarbon Fuels in Flames. *Combust. Sci. Technol., 27*, 31–43.
19. Bustanmante, F., Enick, R.M., Killmeyer, R.P., Howard, B.H., Rothenberger, K.S., Cugini, A.V., … & Ciocco, M.V. (2005). Uncatalyzed and Well-catalyzed Forward Water-Gas Shift Reaction Kinetics. *AIChE J., 51*, 1440–1454.
20. Gomez, M.A., Porteiro, J., Patino, D., & Miguez, J.L. (2014). CFD Modelling of Thermal Conversion and Packed Bed Compaction in Biomass Combustion. *Fuel, 117*, 716–732. http://dx.doi.org/10.1016/j.fuel.2013.08.078
21. Hou, K., & Hughes, R. (2001). The Kinetics of Methane Steam Reforming over a Ni/α-Al2O Catalyst. *Chemical Engineering Journal, 82,* 311–328.
22. Openfoam. (n.d.). *OpenFOAM v2112*. Available at https://www.openfoam.com/news/main-news/openfoam-v2112
23. NIST Chemistry WebBook. (n.d.). *Thermophysical Properties of Fluid Systems.* Available at https://webbook.nist.gov/chemistry/fluid/
24. Openfoam. (n.d.). *OpenFOAM v10 User Guide - 7.1 Thermophysical Models.* Available at https://doc.cfd.direct/openfoam/user-guide-v10/thermophysical
25. Smith, G.P., Golden, D.M., Frenklach, M., Moriarty, N.W., Eiteneer, B., Goldenberg, M., … & Qin, Z. (n.d.) *GRI-Mech 3.0*. Available: http://combustion.berkeley.edu/gri-mech/version30/text30.html
26. Cox, K. R., & Chapman, W. G. (2001). *The Properties of Gases and Liquids* (5th ed.). McGraw-Hill: New York.
27. Yoshizawa, A. (1986). Statistical Theory for Compressible Turbulent Shear Flows, with the Application to Subgrid Modelling. *The Physics of Fluids, 29* (7), 2152–2164. https://doi.org/10.1063/1.865552
28. Bellos, V., Nalbantis, I., & Tsakiris, G. (2018). Friction Modeling of Flood Flow Simulations. *Journal of Hydraulic Engineering, 144* (12), 04018073. https://doi.org/10.1061/(ASCE)HY.1943-7900.0001540.

sciendo

LATVIAN JOURNAL OF PHYSICS
AND TECHNICAL SCIENCES
2023, N 6

DOI: 10.2478/lpts-2023-0045

BUILDING VENTILATION OPTIMIZATION THROUGH OCCUPANT-CENTERED COMPUTER VISION ANALYSIS

J. Telicko*, K. Bolotin

Institute of Numerical Modelling
University of Latvia,
3 Jelgavas Str., LV-1004, LATVIA
*e-mail: jevgenijs.telicko@lu.lv

Buildings consume about 40 % of all energy. Ventilation plays a significant role in both the energy consumption of buildings and the comfort of occupants. To achieve energy efficiency and comfort, smarter ventilation control algorithms can be employed, such as those with feedback based on CO_2 levels. Furthermore, by knowing the current number of people in a space, ventilation can theoretically be adjusted to maintain a constant CO_2 level without wasting energy when people are not present. An additional benefit of such control could arise due to occupants' habits. For example, if a person senses elevated CO_2 levels, even if the ventilation system has started operating more intense, they might choose to open a window, potentially compromising energy efficiency. Therefore, if the control algorithm were to maintain a constant CO_2 level, occupants may be less likely to open windows.

In our work, we explore a model in combination with a custom monitoring system based on computer vision to implement such control. The monitoring system combines outside and inside CO_2 sensors with precise people counting based on computer vision to provide data to the model. The model relies on the mass balance equation for CO_2 and considers the historical data of the number of occupants and their activities to estimate the overall CO_2 generation in indoor spaces. The results suggest that the model can effectively forecast CO_2 dynamics with an absolute deviation of 40 ppm. However, it was observed that the analysis of the actual air exchange level could be compromised by several factors.

***Keywords**: Air exchange, CO2, computer vision, HVAC, people count.*

1. INTRODUCTION

Buildings account for approximately 40 % of total energy consumption [1]. Ventilation holds a crucial role in both the energy usage of buildings and the well-being of occupants. To enhance energy efficiency and comfort, implementing intelligent ventilation control algorithms, such as those incorporating feedback based on CO_2 levels, is essential [2]. For the practical application of such control, defining multiple CO_2 threshold levels is suggested. After surpassing these thresholds, the ventilation mode can be adjusted to maintain the CO_2 level within an acceptable range [3]. Studies suggest that integrating CO_2 sensors with a smart ventilation control algorithm could result in up to 23 % energy savings on ventilation, contingent on occupancy patterns [2].

However, this approach has its drawbacks. First, the system may consume energy even when rooms are unoccupied. Second, the system might alter ventilation rates after CO_2 levels have already changed. Establishing low CO_2 thresholds may lead to unnecessary ventilation, while high thresholds could result in uncomfortable conditions due to insufficient ventilation. Additional energy losses may occur due to occupants' habits. For instance, if individuals perceive elevated CO_2 levels, they might opt to open windows, potentially compromising energy efficiency [4].

In [5] and [6], authors used different pre-trained models to detect the number of people in a room and their activity type. Subsequently, they use these data to simulate a ventilation control system, demonstrating the effectiveness of such an approach. It is important to note that in both papers, the proposed method involves adjusting the ventilation level based on the ASHRAE standard [7] that provides information on the required air flow rate depending on the number of people in the room. In other words, control models do not perform any additional calculations to predict CO_2 concentration, compare it to the required value, and adjust the air exchange accordingly. In earlier investigations, it was determined that employing fish-eye cameras for people counting offers distinct advantages, primarily attributed to their broader field of view. This advantage translates into the feasibility of using fewer cameras [8]. Simultaneously, authors of ventilation control models, incorporating people counting, rely on neural network models trained on the COCO dataset [9]. However, previous research indicates that these models exhibit lower performance when applied to fish-eye cameras, especially in comparison with a custom dataset tailored to the specific location [10]. Notably, some of the neural network models used in the past have newer versions boasting improved accuracy [11]. Consequently, refining these strategies is plausible by opting for a more precise method of people counting.

Therefore, if the control algorithm was to maintain a constant CO_2 level, occupants might be less likely to open windows and intense ventilation would be used only when it was needed. To achieve that potentially, combination of outside inside CO_2 sensors with precise people counting sensing could be used. Knowledge of the history of the number of people and their activity can help assess the overall amount of CO_2 generated in indoor spaces. In turn, knowing the history of the concentration of incoming gas and the history of changes in CO_2 levels in conjunction with knowledge of the integral CO_2 can estimate the current

air exchange indoors. It is important to note that air exchange depends not only on the current operating mode of HVAC system but also on ventilation caused, for example, by door drafts or open windows. In turn, knowledge of current ventilation can help assess the future dynamics of CO_2 indoors and the required ventilation rate needed to achieve a specific CO_2 level, assuming that the number of people remains constant.

The goal of this study is to evaluate combination of monitoring system with model for air exchange and CO_2 dynamic forecast. To achieve the goal, in the Methodology Section, a model based on the mass balance of CO_2 was employed, assuming that the only source of CO_2 was occupants in the room. For evaluation of the model, we build our custom monitoring system and discus its fine-tuning to obtain better results. Finally, results and conclusions are provided in the last two sections.

2. METHODOLOGY

2.1 Experimental Setup

For experimental verification and future integration, to building management system (BMS) the custom monitoring system was developed. For communication of system elements, light for Internet of Things (IoT) protocol and Message Queuing Telemetry Transport (MQTT) were chosen. The system obtains data from several sensors with direct and indirect measurements.

For indirect measurement, people counting, MQTT cameras based on ESP32 are used in combination with post-processing. Due to the limited computational resources of the ESP32, images intended for further processing are transmitted to a central module for subsequent analysis utilizing neural networks. In this scenario, MQTT in conjunction with TLS is employed for securing the personal data transfer. The central module employed is the NVIDIA Jetson AGX Xavier, which is capable of simultaneously processing data from multiple rooms and even entire buildings, thanks to its integrated graphics processing unit. YOLOv8 is chosen for human detection within the images, as this architecture has demonstrated superior performance in prior research studies [10]. To achieve more precise people counting for model training, the custom dataset built from images taken in the experimental space was used [10]. After counting the people in the image, Jetson AGX Xavier sends the result via MQTT, and the data is then stored in a MongoDB database. Subsequently, the model can retrieve the data from there.

For direct measurements such as CO_2 indoors and outdoors custom solutions were also developed. For the indoor CO_2 measurement, the extension board for M5Stack core was designed, see Fig. 1.

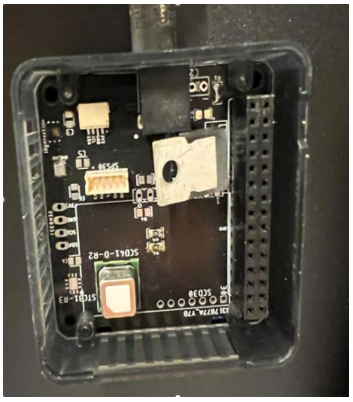

Fig. 1. M5Stack add-on for the CO_2 measurements.

As CO_2 measurement sensor is used, scd41 with measurement error is ±(50 ppm + 2.5 % of reading). This sensor was installed approximately 1 m distance from room wall. M5Stack was powered through an add-on board, which at the same time was connected to the grid. As in this case, board is not dependent from the battery, and the measurement interval was selected 30 seconds.

For the outside CO_2 measurements, the CO_2 sensor is used with ±30 ppm ±3 % of reading measurement error. In this case, the sensor is connected to the M5stack with wire. To protect the sensor from weather conditions, a 3D printed case is used. The sensor is installed 0.1 m from the wall, see Fig. 2.

Fig. 2. CO_2 sensor outside installation.

However, after some time it became clear that in such a configuration, the sensor measured a lot of nonphysical spikes, see Fig. 3.

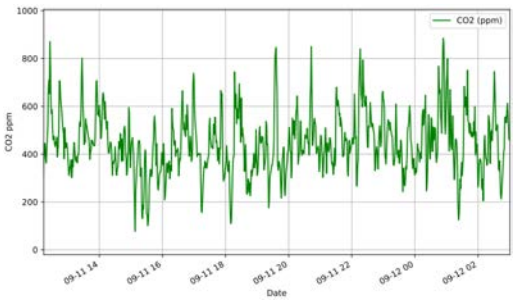

Fig. 3. CO_2 *initial outside measurements.*

To improve the measurement results, air access to the CO_2 sensor from the bottom of 3D printed case is limited with the M5 filter, see Fig. 4.

Fig. 4. CO_2 sensor outside installation improvement.

These changes in the sensor case significantly improved measurements during the night; nevertheless, some spikes during the day were still present, but they became lower, see Fig. 5.

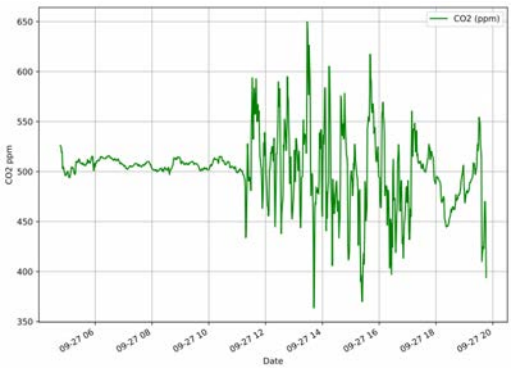

Fig. 5. CO_2 sensor readings after filter installation.

To validate the model, it is necessary to have a historical record of the actual ventilation values over a certain period. For such measurements, it is not sufficient to measure air speed only in ventilation channels, as ventilation can occur through windows, doors, and even via technical engineering openings. That is why the special measurement tool Inova 1412i was used to obtain

the actual ventilation rate. The methodology for the air exchange measurement is based on the constant dosing of the marker gas and the acquisition of its concentration changes in the room. To obtain better results, the marker gas was dosed to an electric fan to ensure a better mixture of gases.

2.2 Calculation of the Indoor CO_2 Concentration and Air Exchange

The model is based on the mass balance equation for the situation, when the indoor source of carbon dioxide comes only from occupants in the room. It can be expressed as [12]:

$$V_R \frac{dC_{in}}{dt} = Q(C_{str} - C_{in}) + N \cdot G_{CO_2},$$

where C_{in} is the indoor concentration of CO_2 (g/m^3); G_{CO2} is the emission rate of CO_2 by one occupant (g/n*h); N is the number of people inside room (n); Q is the ventilation rate of the room (m^3/h); C_{str} – concentration of carbon dioxide in the ventilation air equal to concentration on the street (g/m^3); and V_R is the volume of the investigated room (m^3). For calculations, it is necessary to describe the change of CO_2 concentration during the time interval (Δt) with equation:

$$\Delta C = \frac{\Delta t}{V_R} \cdot \left(N \cdot G_{CO_2} + Q \cdot \left(C_{str} - C_{in,0}\right)\right),$$

where ΔC is the change of the CO_2 concentration (g/m^3); Δt is the time interval (h); and $C_{in,0}$ is the indoor CO_2 concentration at the beginning of the time interval. To calculate the concentration of carbon dioxide at the end of the time interval $C_{in,1}$, the following expression should be used:

$$C_{in,1} = C_{in,0} + \Delta C.$$

To obtain a comprehensive picture, this calculation needs to be performed for each time interval. Initially, constant values of the outdoor CO_2 concentration, the air exchange rate, the room volume, and the amount of CO_2 generated by the occupants were used. Subsequently, to improve the accuracy of the model, additional measurements of the outdoor concentration and the room air exchange rate were conducted. In addition, a crucial component of the developed methodology is the ability to determine the current air exchange rate using the measured values of CO_2 concentration and the number of people in the room. To achieve this, ΔC and $C_{in,1}$ equations were transformed as follows:

$$K_e = \frac{\frac{C_{in,1} - C_{in,0}}{\Delta t} - \frac{N \cdot G_{CO_2}}{V_R}}{C_{str} - C_{in,0}},$$

where K_e is air exchange (h^{-1}) which equals to:

$$K_e = \frac{Q}{V_R}.$$

3. RESULTS AND DISCUSSION

3.1 Experimental Results

As previously mentioned, the measurements were taken for four parameters: the indoor CO_2 concentration, the number of people and the air exchange rate, as well as the outdoor CO_2 concentration. For ease of processing, all results were passed through two filters. Both are median smoothing filters with a sliding window, differing only in the method and the window size. In the first case, this includes all data points within

180-second intervals, while in the second case, it involves 5 data points regardless of time.

For convenience, the results of measuring the air exchange and people count in the room are presented first, since they have a significant influence on the CO_2 concentration. As can be seen in Fig. 6, the ventilation in the room operates from 7 AM to 7 PM. The windows were closed throughout the experiment, so fluctuations in the values are attributed to the measurement system itself, as well as uncontrolled external factors, such as movement of people and variations in the ventilation system performance.

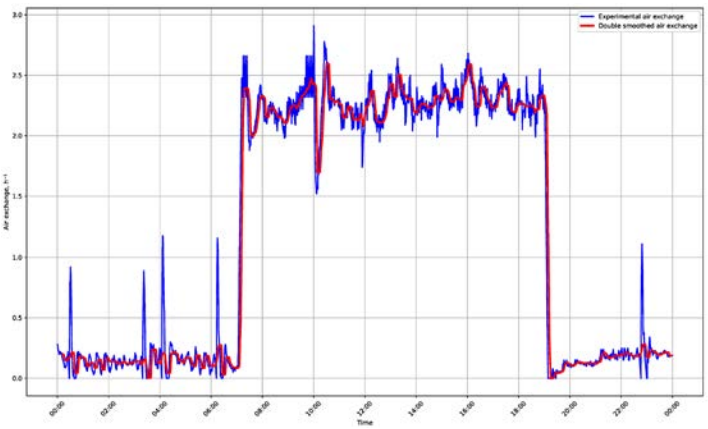

Fig. 6. Experimental results of the air exchange measurements inside the room, as well as smoothed versions of the data.

Figure 7 demonstrates the number of people in the room throughout the day. First employees arrive at 7 AM, last ones leave at 7:40 PM. The changes observed during the day generally align with the work processes. Presence of fractional numbers of people in the smoothed data is due to the omission of rounding, as its application can significantly distort the actual people count [10].

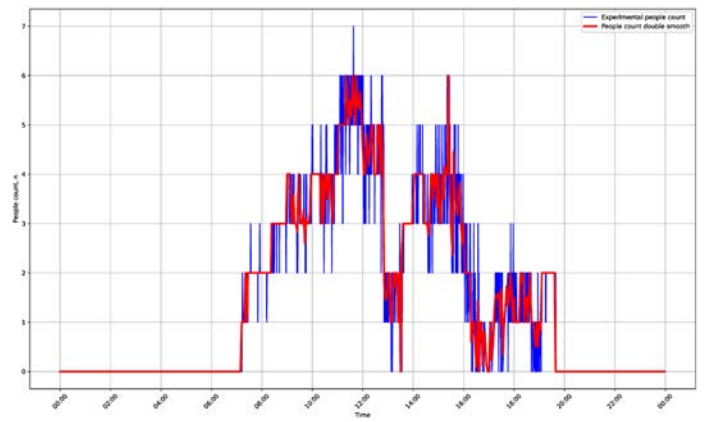

Fig. 7. Experimental results of the people count measurements inside the room, as well as the smoothed versions of the data.

Results of the CO_2 concentration measurements inside and outside the room are shown in Fig. 8.

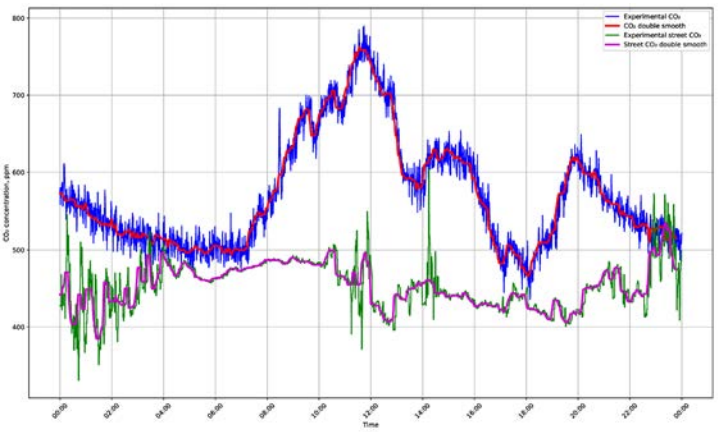

Fig. 8. Experimental results of the CO_2 measurements inside and outside the room, as well as the smoothed versions of the data.

The reason for both graphs to be displayed on a single image will be explained later in the Modelling Results Section. As can be observed, there is a strong correlation between the indoor CO_2 concentration, the number of people, and the ventilation. The increase in concentration begins when the first workers arrive, with several peaks corresponding to changes in their numbers, followed by a gradual decrease in the level of the outdoor concentration after the room becomes empty.

3.2 Calculation Results

At the initial stage, calculation of CO_2 concentration in the room was performed using constant values for the outdoor CO_2 concentration C_{str} = 475 ppm, the air exchange rate K_e = 2.1 h^{-1}, and the CO_2 generation rate per one person engaged in the low activity G_{CO2} = 18 L/n*h [13]. The results are presented in Fig. 9.

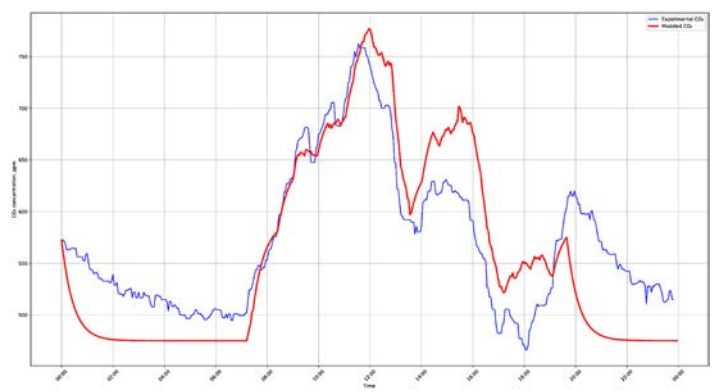

Fig. 9. Smoothed experimental and calculated CO_2 concentration calculated with constant values of air exchange and street CO_2 concentration.

Since ventilation does not operate from 7 PM to 7 AM, a significant discrepancy can be observed during this period. However, this period is not considered significant for the study. In the first half of the day (from 7 AM to 12 PM), the average absolute deviation does not exceed 30 ppm. However, afterwards, the deviation in the data increases to 100 ppm, with particularly significant differences observed from 2 PM to 4 PM and from 7 PM to 8 PM. In the latter case, this is attributed to the ventilation being turned off while people are still present in the room. For the first case, an assumption was made regarding its correlation with changes in the outdoor CO_2 concentration.

Based on these findings, the decision was made to keep only the CO_2 production per person as a constant, while replacing the other two parameters with the experimentally measured data. The new results are presented in Fig. 10.

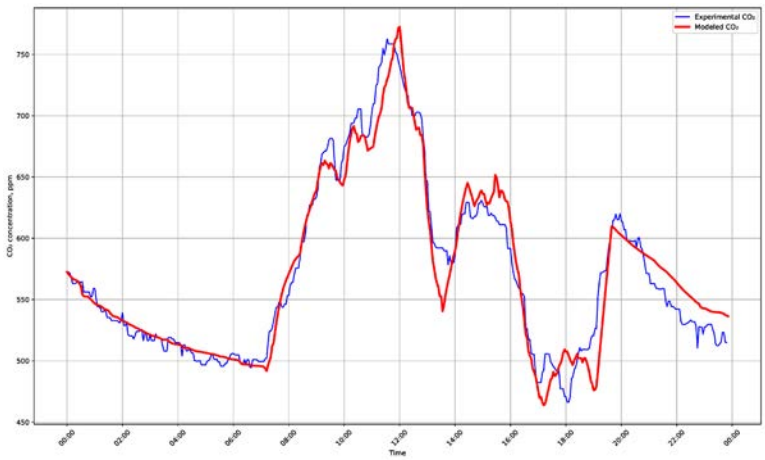

Fig. 10. Smoothed experimental and calculated CO_2 concentration calculated with experimental values of air exchange and street CO_2 concentration.

As can be seen, the deviation of calculated values from experimental ones became more consistent throughout the day, with an average deviation not exceeding 40 ppm. The areas with larger discrepancies are associated with the measurement precision and smoothing. Additionally, variations in CO_2 emissions from individuals based on their activities may also contribute to these differences.

Based on these results, the conclusion is drawn that the selected model is sufficiently accurate, provided that dynamic data for the CO_2 concentration, the air exchange rate, and the number of people are used.

In the next stage, the hypothesis was put forward that by using a reverse model that calculates air exchange based on measured concentrations and the number of people, it would be possible to determine external ventilation sources (such as open windows, doors, etc.), thereby increasing control over the indoor environment. Equation for K_e is used for this purpose, and the obtained results are presented in Fig. 11.

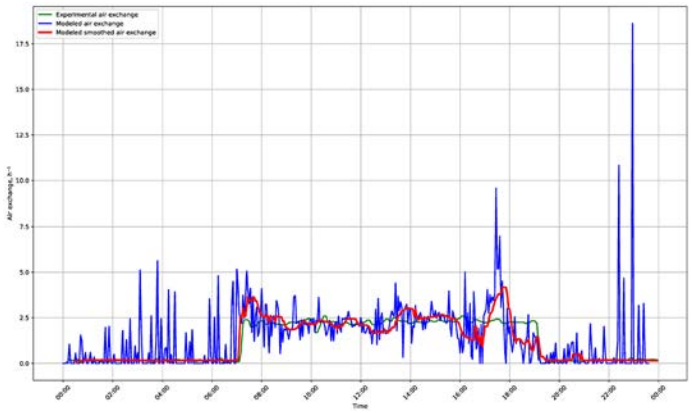

Fig. 11. Smoothed experimental, base calculated and smoothed calculated results of air exchange.

The initial calculated data (blue line) had a significant deviation from the experimental values. It was hypothesized that this discrepancy occurred in areas where the difference between the outdoor and indoor CO_2 concentrations did not exceed 65 ppm. To eliminate these peaks, a logical filter and median smoothing were applied: if abs(C_{in} - C_{str}) < 65 ppm then K_e = 0.2 h^{-1}. Also, the median smoothing by 5 points was used, too. Red line illustrates the results.

To validate this approach, a re-calculation of indoor CO_2 concentration was performed, and the results are shown in Fig. 12.

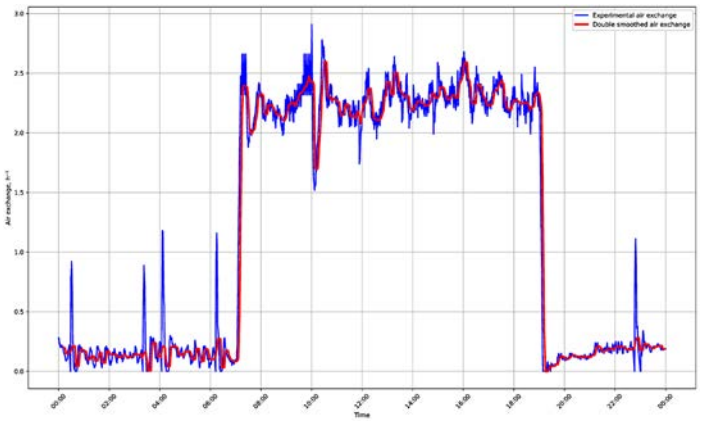

Fig. 12. Smoothed experimental, base calculated and smoothed calculated results of the air exchange.

As can be seen, the smoothing did not lead to significant changes, and both graphs have a minimal deviation from each other. Therefore, in the future, by knowing the parameters of controlled ventilation, it will be possible to calculate air exchange and, by comparing it, draw conclusions about the presence of external sources of air. Additionally, by varying the air exchange rate in the calculations of CO_2 concentration, it will be possible to predict its behaviour and choose the most effective room ventilation programme.

4. CONCLUSIONS

In the first stage, it was demonstrated that using constant values for the air exchange rates and the CO_2 concentrations in the outdoor air does not accurately predict the indoor CO_2 concentration. As a result, additional measurements of the necessary parameters were conducted, and after these adjustments, the average deviation between the simulated and experimental CO_2 concentration values did not exceed 40 ppm. Thus, it was shown that by measuring the number of people and the outdoor CO_2 concentration, along with having data on the air exchange rates, it is possible to predict the indoor CO_2 concentration with high accuracy and control ventilation.

In the second stage, it was proposed to not only analyse the CO_2 concentration but also compare it with the measured value to identify external sources of outdoor air, such as open windows or doors. For this purpose, the air exchange rate in the balance equation was expressed as a function of both the indoor and outdoor CO_2 concentrations and the number of people.

The results of modelling in the second stage demonstrate that predicting the air exchange rate is highly dependent on the accuracy of the parameter measurements and is strongly influenced by the difference between the indoor and outdoor CO_2 concentration values. Significant deviations (up to 10 h^{-1}) from experimental data were observed when the concentrations difference was below 65. Therefore, several logical filters were applied to eliminate excess peaks, and the overall error in the results was reduced to 2 h^{-1}.

Afterwards, a reverse modelling was conducted. Using the measured people count, the CO_2 concentration outside the room, and the simulated data on air exchange, the calculation of the CO_2 concentration inside the room was calculated. Comparison with experimental data yielded an absolute deviation of 40 ppm, which can be considered a sufficiently accurate result.

In summary, it has been demonstrated that through computer vision monitoring of people count, sensors measuring CO_2 concentrations inside and outside the room, and access to ventilation parameters, it is possible not only to build a control system by modelling the indoor CO_2 concentration but also to predict external sources of fresh air to improve the indoor environmental control. To obtain even better results, construction of the indoor CO_2 sensor could be improved. However, further research is required to develop such a control system based on the developed model with potential improvements of CO_2 measurement.

ACKNOWLEDGEMENTS

The research has been supported by the European Regional Development Fund project “Development and Approbation of Complex Solutions for Optimal Inclusion of Capillary Heat Exchangers in Nearly Zero Energy Building Systems and Reduction of Primary Energy Consumption for Heating And Cooling” (1.1.1.1./19/A/102).

REFERENCES

1. Ahmad, A., Hassan, M., Abdullah, M., Rahman, H., Abdullah, F.H., & Saidur, R. (2014). A Review on Applications of ANN and SVM for Building Electrical Energy Consumption Forecasting. *Renewable and Sustainable Energy Reviews, 33*, 102–109.
2. Nassif, N. (2012). A Robust CO2-Based Demand-Controlled Ventilation Control Strategy for Multi-Zone HVAC Systems. *Energy and Buildings, 45,* 72–81.
3. Fisk, W.J., Sullivan, D.P., Faulkner, D., & Eliseeva, E. (2010). *CO2 monitoring for demand-controlled ventilation in commercial buildings.* Available at https://eta-publications.lbl.gov/sites/default/files/lbnl-3279e.pdf
4. Howard-Reed, C., Wallace, L.A., & Ott, W.R. (2002). The Effect of Opening Windows on Air Change Rates in Two Homes. *Journal of the Air & Waste Management Association, 52*, 147–159.
5. Wei, S., Tien, P.W., Chow, T.W., Wu, Y., & Calautit, J.K. (2022). Deep Learning and Computer Vision Based Occupancy CO2 Level Prediction for Demand-Controlled Ventilation (DCV). *Journal of Building Engineering, 56*.
6. Yang, B., Liu, Y., Liu, P., Wang, F., Cheng, X., & Lv, Z. (2023). A Novel Occupant-Centric Stratum Ventilation System Using Computer Vision: Occupant Detection, Thermal Comfort, Air Quality, and Energy Savings. *Building and Environment, 237.*
7. American Society of Heating, Refrigerating and Air Conditioning Engineers. (2019). *Ansi/Ashrae Standard 62.1-2019, Ventilation for Acceptable Indoor Air Quality.*
8. Telicko, J., Vidulejs, D., & Jakovics, A. (2021). A Monitoring System for Evaluation of Covid-19 Infection Risk. *Journal of Physics: Conference Series, 2069*, 012192.
9. Lin, T.-Y., Maire, M., Belongie, S., Bourdev, L., Girshick, R., Hays, J. …& Doll´ar, P. (2014). *Microsoft Coco: Common Objects in Context*. Available at https://arxiv.org/abs/1405.0312
10. Telicko, J., & Jakovics, A. (2023). Comparative analysis of yolov8 and mack-rcnn for people counting on fish-eye images. In *the 3rd International Conference on Electrical, Computer, Communications and Mechatronics Engineering (ICECCME),* (pp. 1–6), 2023.
11. Hussain, M. (2023). Yolo-v1 to Yolo-v8, the Rise of Yolo and its Complementary Nature toward Digital Manufacturing and Industrial Defect Detection. *Machines and Tooling, 11*, 677.
12. Heidt, F., & Werner, H. (1986). Microcomputer-Aided Measurement of Air Change Rates. *Energy and Buildings, 9*.
13. Persily, A, & de Jonge, L. (2017). Carbon Dioxide Generation Rates for Building Occupants. *Indoor Air, 27,* 868–879.

sciendo

LATVIAN JOURNAL OF PHYSICS
AND TECHNICAL SCIENCES
2023, N 6

DOI: 10.2478/lpts-2023-0046

THE USE OF RENEWABLE ENERGY AND CAPILLARY HEAT EXCHANGERS FOR ENERGY SAVINGS IN THE EXISTING APARTMENT

S. Gendelis[1], A. Jakovics[1], O. Pulkis[2], I. Bukans[2]

[1] Institute of Mechanics and Mechanical Engineering
[1]Faculty of Physics, Mathematics and Optometry,
University of Latvia,
3 Jelgavas Str., Riga, LV-1004, LATVIA
[2]Hydrokapillar Tech, Ltd.,
158 Brīvības Str., Riga, LV-1012, LATVIA
*e-mail: stanislavs.gendelis@lu.lv

The use of capillary heat exchangers with a large area means the lowest heat carrier temperature – typically less than 30 °C for heating. This determines the very efficient use of the installed heat pump due to an increase in the coefficient of performance (COP) with a decrease in the provided water temperature. The aim of the study was to find out whether renewable energy sources and radiant capillary heat exchangers increase energy efficiency. In order to achieve the maximum energy efficiency during the renovation of the existing apartment, a combination of two green approaches was used. One of them is the replacement of the existing high-temperature radiator heating system with radiant capillary mats. The same system is also used for cooling, which was not possible with the existing system. The necessary energy is provided from renewable aerothermal energy by installing a heat pump together with PV panels to ensure electricity consumption.

The measurements were made in the apartment to determine the thermal transmission properties of all boundary structures and an air exchange rate using long-term monitoring. Experimental data were used to create the heat balance, to estimate the heating and cooling powers, as well as the seasonal energy needs. The amount of capillary heat exchangers and the size of the heat pump were chosen accordingly.

The very first energy consumption data allow concluding that the planned improvement of the energy efficiency has been successfully achieved by using technology combination described without improvement of the thermal properties.

Keywords*: Energy efficiency, heat pump, radiant heat exchanger, renewable energy source.*

1. INTRODUCTION

Due to the recent increase in the energy prices, the issue of usage of renewable energy sources has become highly important. It is critical not only to alter energy sources, but also to minimize end-user energy requirements by enhancing building energy efficiency and utilizing highly efficient heating and cooling systems.

Heat pumps are the most widely used renewable and very efficient energy source for heating, with costs equivalent to natural gas and district heating systems [1]. Their efficiency described as coefficient of performance (COP) increases when the temperature difference between the energy source and the heat exchanger in the room decreases [2], [3]. Traditional convectors have heat carriers with temperatures above 50 °C, the use of an underfloor water-based heating system reduces the temperature to 40 °C due to a larger area. However, radiant capillary heat exchangers (RCHE) [4] with the biggest surface areas are the most effective heat exchanger options, allowing one to decrease the water temperature to 26–30 °C with the same amount of power. Another advantage of RCHE is that it may be used in both heating and cooling modes. Therefore, the most effective way to reduce the heating costs without doing anything with the boundary structures is a combination of the efficient heat pump with as low heat carrier temperature as possible.

The aim of the study is to experimentally show the possibility to reduce to minimum or even to avoid the externally supplied energy by installation of combination of modern technical systems and technologies (Fig. 1), with the focus on efficiency and renewable energy sources. It is important to note that the study is carried out in an old non-insulated building without improvement of its boundary structures.

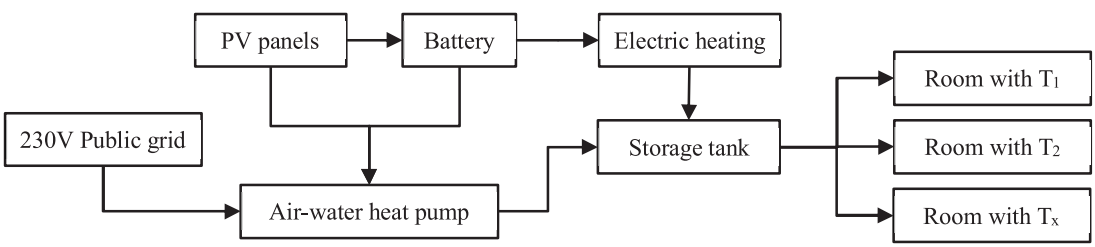

Fig. 1. Planned energy flows in a studied apartment.

2. MATERIALS AND METHODS

In order to achieve the maximum energy efficiency during the renovation of the heating system only in an existing apartment with four rooms and heated floor area of 47 m^2 (Fig. 2), a combination of three modern and energy effective approaches was used. One of them is the replacement of the existing high-temperature radiator heating system with radiant capillary mats (Fig. 3, left); the same system is also used

for cooling, which was not possible with the existing system. The other is to use an air-water heat pump technology for the needed energy production (Fig. 3, centre). The third component is photovoltaic (PV) panel system with batteries for production of electricity, which is necessary to operate the heat pump (Fig. 3, right). A comprehensive scheme showing all installed components is illustrated in Fig. 4.

Before starting the experiment, the required power and annual energy demand for the apartment was determined to select the most appropriate heat pump, the number of PV panels and the necessary number of capillary mats to be installed. Two calculation methods – a complex and precise approach based on the ISO 52016-1 standard [5, 6] and a simplified calculation tool with capillary mats plugin [7] developed at the Institute of Numerical Modelling of the University of Latvia – were used.

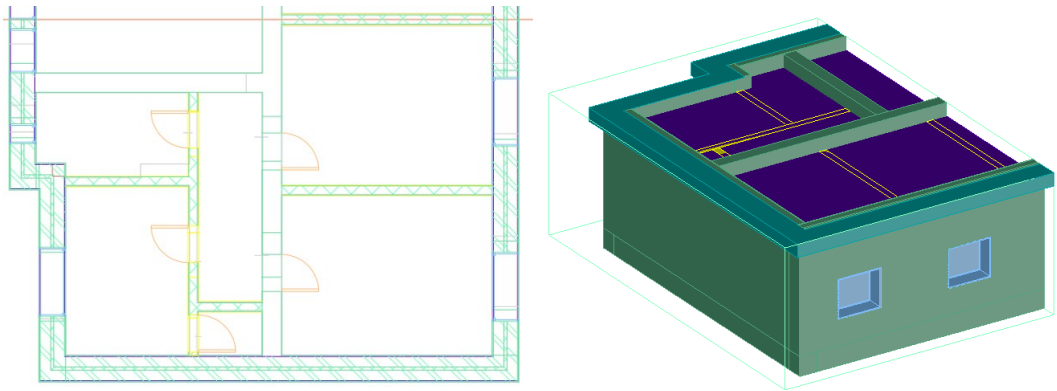

Fig. 2. Plan (left) and 3D model (right) of the apartment with installed components.

Fig. 3. The main used components – capillary mats, heat pump and battery (see also Fig. 4).

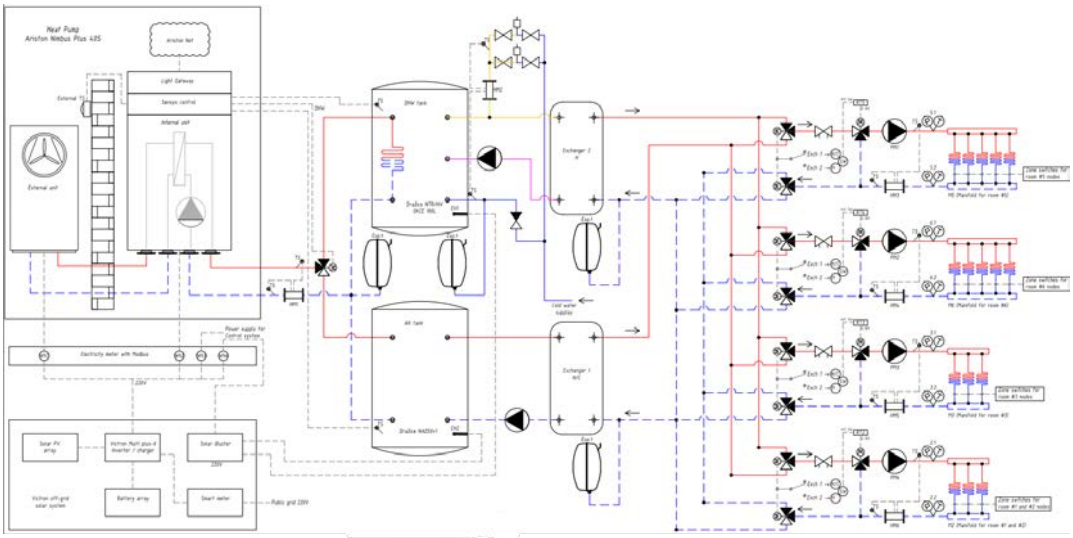

Fig. 4. Schematic principle of the installed combination of technical systems (see Figs. 1, 3).

The main parameters to determine heat losses from the apartment – thermal transmission (U-values) of all boundary structures, incl. walls, ceiling and floor, as well as air exchange rate describing convective heat losses – were established experimentally using long-term measurements (Fig. 5). The obtained results are used in the above-mentioned simplified and detailed calculation heat balance models – resulting energy demand for both approaches produces very similar results (9200 kWh per year), but the estimated heating power value differs by more than 20 %; therefore, 4 kW value is taken from the standard-based (as the most detailed and verified) model.

In the next step, the power of the heat pump and the appropriate model Ariston Nimbus Plus 40 S was matched to provide full heating needs and potential domestic hot water demand. Its maximum heat output for water temperature regime in a capillary mats 35/30 °C is 5.7 kW at air temperature of 7 °C; rated COP at this temperature reaches 5.1 (in accordance with EN 14511), which is typical of modern air-water heat pumps [8]. Available studies on the application potential and possibilities of air-to-water heat pumps in Latvian climate [9], [10] show the estimation of overall seasonal efficiency (COP) reaching 3.6…4.5 at high outdoor temperatures depending on various parameters, e.g., building energy demand.

The parameters of the installed PV system are selected in such a way as to maximally cover the electricity need of the heat pump compressor throughout the 24-hour cycle. The following parameters were obtained as a result of the modelling [11]: 3.75 kWp total installed peak power (10 modules); 6kWh LFP-type battery; 2kW additional electric water heating device.

Radiant capillary heat exchangers are installed in the rooms using different installation methods (Fig. 6): on the ceiling using KNAUF D112 gypsum board suspended ceiling system [10], on the walls – using wood wool panels [12] and on the floor made of the dry expanded clay – with self-levelling floor mix.

Fig. 5. Measurements of thermal transmittance and air change rate.

Fig. 6. Capillary heat exchangers installed on the ceiling, walls and floor.

Installed capillary heat exchangers system (Fig. 4) allows providing the set temperature in each room independently, regardless of the heating or cooling need and heat sources like different solar intensity of the opposite facades and variable occupancy. This type of solution is especially useful in cases of temperature fluctuations during the spring/autumn seasons. For this purpose, two water tanks are installed in the system (Figs. 4 and 7). Hot water is prepared in one of them (incl., also domestic hot water for shower and kitchen), and cold water in the other. Three-way valve is used for switching between heating/cooling and domestic hot water preparation. Accordingly, two heat exchangers (see Fig. 4) are also installed in the system, which can optionally be connected to the manifold of any room with the help of a motorized 3-way switch valve. Dozens of temperature, air humidity and pressure sensors are installed for monitoring, control and management of the heating/cooling modes. For cooling mode dew point sensors are very critical. Ultrasonic heat energy meters are installed on the water pipes in each room; the different energy loops (incl., heat pump and PV system) are equipped with the electric energy meters.

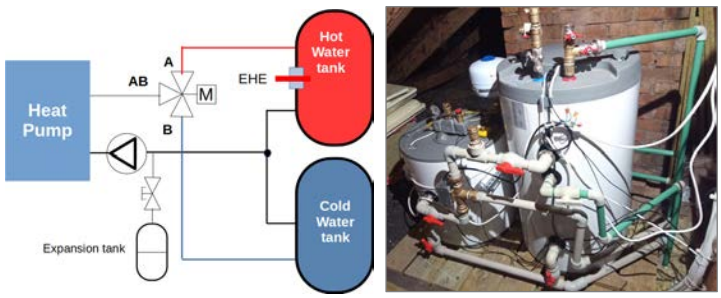

Fig. 7. Schematic principle and a photo of hot and cold-water tanks for simultaneous heating and cooling in different rooms.

3. RESULTS AND DISCUSSION

Since the installation of the system components in the experimental apartment was completed in the spring of 2023, the quantitative measurement data of the overall system would be available only after one full year of operation. However, it is possible to approximately estimate the expected minimum (guaranteed) reduction in the energy consumption under real operating conditions determined using two renewable resources (air-water heat pump and PV panels) in combination with low temperature heat exchanger (capillary mats).

As mentioned above, the manufacturer declares the coefficient of performance of the installed heat pump as 5.1 if the temperature of the used heat carrier does not exceed 35 °C at the external temperature or 7 °C. However, it should be taken into account that the average outdoor temperature in Riga, Latvia, during the heating season is 1.1 °C [14], which means lower efficiency of the heat pump. The practical long-term operation experience from 2014 of more than 100 of various air-to-water heat pump systems installed in Latvia [15] shows that the experimentally measured seasonal COP (SCOP) value is approximately 30 % lower than widely used declared values [16] – depending on the installation type, heat pump power and heat carrier temperature, which varies between 3 and 4. According to statistics [15], typically, at outdoor temperature within -5…0 °C, COP for air-to-water heat pumps is experimentally estimated as 2.9 (Fig. 8), but with the temperature increase up to +7 °C, the measured real efficiency reaches the value of 4.2 (within 0…7 °C) [9], [15]. Therefore, during the heating season, it can be guaranteed that the consumption of primary energy (electricity) using an air-water heat pump in combination with low-temperature heating system will decrease by at least three times.

The cooling demand of buildings in the climatic condition of Latvia [14] (especially with massive external walls and relatively small glazing part) is significantly smaller than the heating need; therefore, the use of installed heat pump is not analysed in detail. It is important to highlight, that the power of installed PV modules with a maximum power of 3.8 kWp together with 6 kWh battery is sufficient to provide more than 75 % of the necessary heating energy and all the energy needed for shorter cooling periods during summer. Energy production from the installed PV system in combination with hot water tank and additional electric heater can also fully ensure the supply of domestic hot water needs. The energy production from the installed PV panels from October to February [17] is relatively small (Fig. 9) and approx. 25 % of the needed energy must be bought from the public grid, but it is fully compensated by the energy produced during the summer months.

Monitoring data from the installed PV system in an apartment during the first five experiment months (April–August 2023) show that most of the energy is delivered to the public grid, and only approx. 40 % is used in the apartment (Fig. 10). This allows concluding that the planned energy efficiency improvement can be successfully achieved using a combination of heat pump with low temperature heat exchanger and PV panels with battery, without changing the thermal properties of the boundary structures.

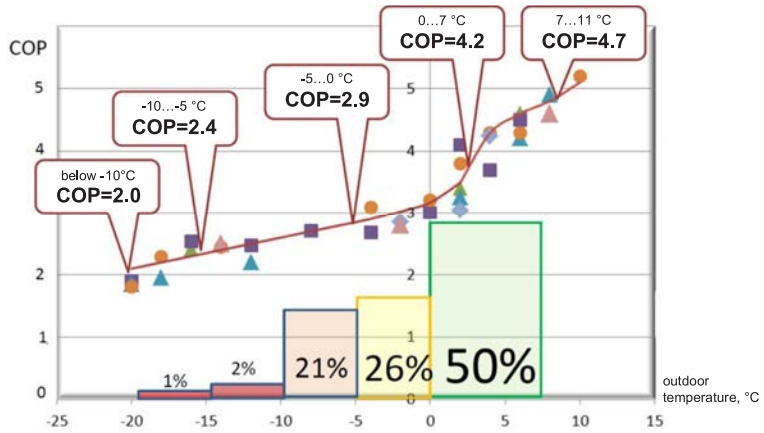

Fig. 8. Distribution of experimentally estimated COP of installed air-water heat pumps [15].

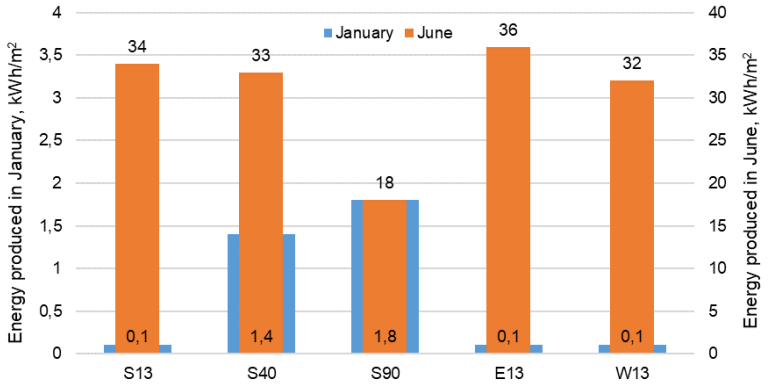

Fig. 9. Monthly energy produced by different oriented PV panels in winter/summer (2022).

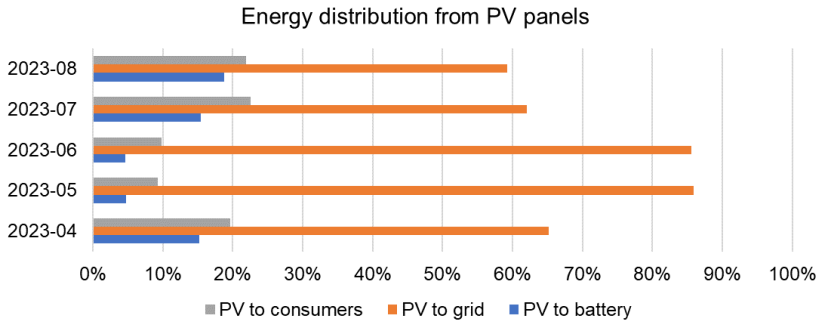

Fig. 10. Distribution of energy produced by PV panels (2023).

Estimation of the heating energy for the apartment based on the heat balance approach results in 9200 kWh annually (final energy) or 196 kWh/m^2 that corresponds well to the average performance of a non-insulated building. Considering that

an average outdoor temperature during the heating season is 0 °C and assuming the seasonal COP for the heat pump as 3.5 (Fig. 8), the electricity consumption (delivered energy) is determined as 2630 kWh.

In the next step, let us determine the amount of electricity produced by the PV panels installed on the roof. Assuming that the 3.8 kWp PV system produces 3420 kWh annually with 28 % during the 7 months (October–April) of a heating season [17], the energy produced both – directly and using battery – is calculated as 962 kWh.

Considering the electricity price as 0.2 €/kWh and the naturas gas price as 0.12 €/kWh, it is possible to evaluate the potential savings in the studied apartment after installation of the described technical systems (see Table 1) – the heating costs per year for the apartment with gas boiler are approx. 1100 €, but after installation of low temperature capillary heat exchangers and combination of PV system and heat pump the heating costs are reduced three times – to 380 €. The part on renewable energy sources in the heating energy need exceeds 80 % (Fig. 11).

Table 1. Heating Energy Costs Using Renewable Energy Sources and Capillary Heat Exchangers

Apartment	Final energy	Delivered energy	Renewable energy		Heating costs, €/year
	kWh annually			%	
Before improvement	9200	9200	0	-	1100
After improvement	9200	2630	6570	80	380

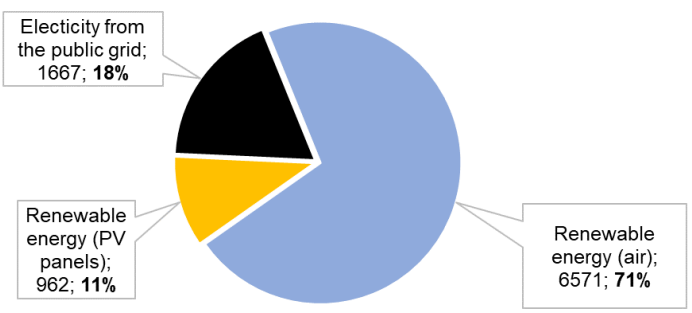

Fig. 11. Distribution of energy needs in the studied apartment (kWh annually).

4. CONCLUSIONS

The first recorded heat energy consumption data from the spring/summer of 2023, as well as the electricity production from the photovoltaic panel system, are in good agreement with the theoretically expected values. This allows concluding that the planned energy efficiency improvement can be successfully achieved using an implemented combination of heat pump with low temperature heat exchanger and PV panels

with battery system, without changing the thermal properties of the boundary structures. The potential cost reduction is three times with the share of renewable energy resources usage up to 80 %.

As a result, an important conclusion can be drawn that increasing the energy efficiency and reducing the heating cost in an existing apartment can be successfully achieved even without changing the thermal properties – by using a combination of low-temperature heat exchangers, high-efficiency heat pump and solar energy system with energy storage.

ACKNOWLEDGEMENTS

The research has been supported by the European Regional Development Fund project "Development and Approbation of Complex Solutions for Optimal Inclusion of Capillary Heat Exchangers in Nearly Zero Energy Building Systems and Reduction of Primary Energy Consumption for Heating and Cooling" (1.1.1.1./19/A/102).

The project is co-financed by REACT-EU funding for mitigating the consequences of the pandemic crisis.

REFERENCES

1. Song, J., Li, H., & Wallin, F. (2017). Cost Comparison Between District Heating and Alternatives During the Price Model Restructuring Process. *Energy Procedia, 105*, 3922–3927. doi: 10.1016/j.egypro.2017.03.813.
2. Goldschmidt, VW. (1984). Heat Pumps: Basics, Types, and Performance Characteristics. *Ann. Rev. Energy, 9,* 447–72.
3. Arpagaus, C., Bless, F., Uhlmann, M., Schiffmann, J., & Bertsch, S.S. (2018). High Temperature Heat Pumps: Market Overview, State of the Art, Research Status, Refrigerants, and Application Potentials. *Energy 152*, 985–1010, doi:10.1016/j.energy.2018.03.166.
4. Nemethova, E., Krajcik M., & Petras D. (2019). Performance of the Building with Three Different Radiant Systems. *IOP Conf. Series: Materials Science and Engineering, 471*, 062013. doi: 10.1088/1757-899X/471/6/062013.
5. International Organization of Standards. ISO 52016-1:2017. (2017). Energy Performance of Buildings – Energy Needs for Heating and Cooling, Internal Temperatures and Sensible and Latent Heat Loads – Part 1: Calculation Procedures.
6. HeatMod. (n.d.). *Application for Calculating of the Building Energy Performance in Accordance with LVS EN ISO 52000 Series Standards*. Available at http://www.heatmod.lv
7. Gendelis, S., Teličko, J., Jakovičs, A., & Bukans, I. (2023). Radiant Capillary Heat Exchangers – Power Calculation for Optimal Heating and Cooling. *Journal of Physics: Conference Series, 2423* (1), 012011. doi: 10.1088/1742-6596/2423/1/012011.
8. O'Hegarty, R., Kinnane, O., Lennon, D., & Colclough, S. (2022). Air-to-Water Heat Pumps: Review and Analysis of the Performance Gap between In-use and Product Rated Performance. *Renewable and Sustainable Energy Reviews, 155*, 111887. doi:10.1016/j.rser.2021.111887.
9. Zajacs, A., Lebedeva, K., & Bogdanovičs, R. (2023). Evaluation of Heat Pump Operation in a Single-Family House. *Latvian Journal of Physics and Technical Sciences, 60* (3), 85–98. doi:10.2478/lpts-2023-0019.

10. Bogdanovičs, R., Borodinecs, A., Zajacs, A., & Šteinerte, K. (2018). Review of heat pumps application potential in cold climate. In Vera Murgul, & Zdenka Popovic (eds.), *International Scientific Conference Energy Management of Municipal Transportation Facilities and Transport EMMFT 2017. EMMFT 2017. Advances in Intelligent Systems and Computing, 692*. Springer, Cham. doi: 10.1007/978-3-319-70987-1_58.
11. Gendelis, S. (2022). Experimental Studies of a Long-Term Operation of Different Batteries Used in PV System. *International Multidisciplinary Scientific GeoConference Surveying Geology and Mining Ecology Management, SGEM, 22* (4.1), 89–96. doi: 10.5593/sgem2022/4.1/s17.12.
12. KNAUF. (n.d.). *Ceiling Systems*. Available at http://knauf.iq/en/systems/ceiling/
13. CEWOOD. (n.d.). *Wood Wool Panels*. Available at https://www.cewood.com
14. Latvian Cabinet of Ministers. (2019). *Regulations regarding the Latvian Building Code LBN 003-19 "Construction Climatology"*. Riga.
15. RIKON AC. (n.d.). *Heat Pump Operation Statistics in Latvia*. Available: http://www.gaiss-udens.lv/lv/siltumsuknu-eksplutacijas-statistika
16. Zirngibl, J. (2020). Heat Pump Standard EN 15316-4-2 – From Compliance to Real Consumption. *REHVA Journal, 06/20205* (9), 5–9.
17. Gendelis, S., Heincis, D., & Telicko, J. (2021). Measurements of the Actual Efficiency of PV Panels Depending on their Orientation and Environmental Temperature. *International Multidisciplinary Scientific GeoConference Surveying Geology and Mining Ecology Management, SGEM, 21* (6.2), 75–82. doi: 10.5593/sgem2021V/6.2/s26.13.

sciendo

LATVIAN JOURNAL OF PHYSICS
AND TECHNICAL SCIENCES
2023, N 6

DOI: 10.2478/lpts-2023-0047

APPLYING DYNAMIC U-VALUE MEASUREMENTS FOR STATE FORECASTING IN BUILDINGS

J. Telicko[1], A. Jakovics[1]

[1] Institute of Numerical Modelling
University of Latvia,
3, Jelgavas Str., LV-1004, LATVIA
*e-mail: jevgenijs.telicko@gmail.com

In the present day, monitoring and automated control stand as pivotal factors for the energy-efficient and comfortable operation of buildings. As the demand for indoor climate control grows, building management systems have become more intricate, making their control challenging due to the increasing number of controllable elements. Replacing manual human analysis of complex systems can be achieved through the utilization of algorithms like model-based control. It is important to note that performance of this method usually relies on the accuracy of neural network-based building state forecasts. Studying the internal dynamics of climate as influenced by temperature changes necessitates a brief record of measurements, whereas evaluating structural modifications through moisture transfer demands data covering a more extended period. Neural networks such as Long Short-Term Memory have the potential to lose information within lengthy time-series data, and the intricate nature of moisture transfer further adds complexity to the task of approximating functions, ultimately leading to a reduction in energy efficiency. In order to improve the precision of indoor climate predictions, our suggestion involves not only assessing changes in temperature but also considering alterations in U-values triggered by temperature variations and moisture transfer. Our preliminary assessment of the influence of U-value, conducted through numerical simulations using WUFI6, exposes variations of up to 10 % of U-value in certain scenarios. Dealing with these computations in real time using physical models proves to be demanding due to computational requirements and limited data availability. To tackle this issue, we present an innovative preprocessing approach for on-the-fly evaluation of U-values. Empirical trials involving three years of monitoring data indicate that the suggested technique led to an approximate 8 % reduction in the average mean squared error of climate predictions based on neural network models, in specific instances.

Keywords*: Artificial intelligence, model-based predictive control, moisture transfer, neural networks, WUFI.*

1. INTRODUCTION

According to previous research [1], buildings contribute to 39 % of total greenhouse gas emissions and approximately 40 % of global energy consumption [2]. Furthermore, statistics [3] reveal that people spend 87 % of their time inside various types of buildings. As a result, buildings significantly impact the quality of human life and Earth's ecology. A key factor in ensuring energy-efficient and comfortable use of buildings is monitoring with automated control.

As early as the last century, people began to optimize building control using scheduled control techniques [4]. However, this approach has several disadvantages. First, it requires a significant amount of human labour to analyse a building behaviour. Second, due to the fluctuating behaviour of buildings, which is influenced by factors such as changes in material properties, environmental conditions, and building system characteristics, constant human involvement is necessary to modify the control schedule.

As demand for the indoor climate grows, the complexity of building control rises due to the increased number of controlled systems within the building. Therefore, manual analysis and implementation of the building control program can be subject to errors, associated with human factors. That is why control methods that are capable of assessing the dynamics of a task and controlling a building independently are gaining popularity [5], [6]. Unfortunately, studies that compare the effectiveness of classical methods with methods in which artificial intelligence (AI) tools are used indicate that, at the moment, classical methods are slightly more effective [4]. This motivates research to improve control tools based on AI.

One of the methods capable of independently evaluating the dynamics of a building is model-based predictive control (MPC). Like many other AI-based building control algorithms, MPC uses forecasts of one or several parameters. In a detailed manner, the MPC forecasts different building states under different building management system (BMS) control configurations and then chooses the BMS configuration which will most closely achieve the target building state [7]. In such systems, energy efficiency and the quality of the indoor climate are highly dependent on the accuracy of the forecast [8]. Unfortunately, the usage of verified computational fluid dynamic models for the real-time forecast is almost impossible due to the high computational resources required, as well as several building properties not always being available. To solve this problem, several authors used neural networks (NN) that are capable of operating with noisy data and in an undefined space [9], [10]. To create a qualitative forecast of the internal climate of a building, it is important to supply the NN with a set of data, which would contain as much information on the state of the building as possible. Usually, recurrent neural network architectures are used for building state forecasting as time-series data are required to evaluate the dynamics of a building [11], [12]. To analyse changes in the dynamics of the internal climate of a building caused by temperature changes, a relatively short history of measurements is required. However, the analysis of changes in structural properties caused by moisture transfer requires much longer historical data. It is known that even architectures with large core memory such as Long Short-Term memory could lose information with large time-series data [13]. In addition, from a mathematical point of view, moisture transfer is more complex than heat transfer. As a result, the approximating

function for a neural network becomes more complicated, which leads to a decrease in forecast accuracy. In theory, measurements such as heat flux, combined with exterior and interior temperatures, could provide neural networks with knowledge about U-value changes in materials. These changes are caused by moisture transfer and temperature fluctuations within the building construction, which influence the thermal conductivity properties of the wall materials and lead to different heat transfer behaviour.

In this paper, to improve the accuracy of indoor climate forecasts within a building, we suggest evaluating not only temperature changes but also changes in the U-value caused by temperature fluctuations and moisture transfer. Since neural networks are not transparent algorithms, at the initial stage, we numerically evaluate the influence of changes in the U-value on heat transfer in the building. To assess the impact of this variable on a specific construction example, we use numerical simulation in WUFI. After that, we use different neural networks in combination with pre-processed data from sensors to assess the impact of the U-value on the indoor climate forecast.

In Section 2, a verified numerical simulation in WUFI is employed to assess U-value changes in a specific construction. In Section 3, heat flux pre-processing techniques for obtaining a reference U-value are discussed. In Section 4, the dynamic U-value input parameter is experimentally evaluated using two different neural network models. Finally, results and discussions are provided in Section 5, and conclusions are outlined in Section 6.

2. U VALUE CHANGE EVALUATION BY WUFI

Nowadays, building constructions are typically inspected before they are built to predict potential mould growth in thermal insulation layers. Mould can be harmful to human health, and its growth depends on factors such as the material biological properties, humidity, and temperature [14]. To obtain humidity data in thermal insulation layers, moisture transfer must be considered.

Several numerical simulation tools, such as WUFI, Delphin, and others, are available for this purpose. For this research, WUFI was chosen to evaluate seasonal changes in material properties.

A real experimental building at the Botanical Garden of the University of Latvia was selected as a reference construction for evaluating moisture transfer impact. This building features a simple geometry, with interior room dimensions of 3x3 meters. Additionally, each wall of the building is composed of the same combination of materials, allowing for the analysis of one wall to be easily applied to the others. The distribution of wall materials for the chosen construction is as shown in Fig. 1.

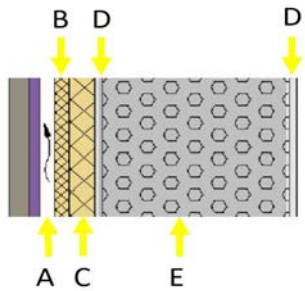

Fig. 1. Distribution of materials in walls, where: (A) is a ventilated facade, (B) is Roxul FacadeRock stone wool with a thickness of 30 mm, (C) is Roxul Plus stone wool with a thickness of 50 mm, (D) is cement-lime plaster with a thickness of 15 mm and (E) is aerated concrete with a thickness of 375 mm.

For the formulation of the numerical simulation task, it is crucial to define the initial boundary conditions of the buildings. One of the greatest advantages of WUFI is its comprehensive material database. The software provides the necessary material properties and property functions, such as the dependence of thermal conductivity (λ) on moisture content. The starting water content level plays a significant role, as the material thermal conductivity is highly dependent on it. Unfortunately, measuring the physical state of the building is not possible, as it requires samples of materials from all layers. Therefore, when creating the simulation, this parameter was determined iteratively, using humidity data from the Roxul Plus layer sensor as a reference signal.

For the interior and exterior environment boundary conditions, monitoring data collected from a system installed in the building and from a weather station located on the roof were used. WUFI results provide information on changes in several parameters.

To verify the numerical simulation, parameters such as humidity could be compared to measured values. For this purpose, a temperature/humidity sensor (SHT35) was positioned within a wall, nestled between the stone wool and the cement-lime plaster (see Fig. 1). WUFI provides the opportunity to deploy virtual sensors to obtain simulation results from specific points within a wall. To verify simulation, a virtual sensor in WUFI was also placed between the stone wool and the cement-lime plaster. The comparison of humidity trends between the simulation and the physical sensor is depicted in Fig. 2.

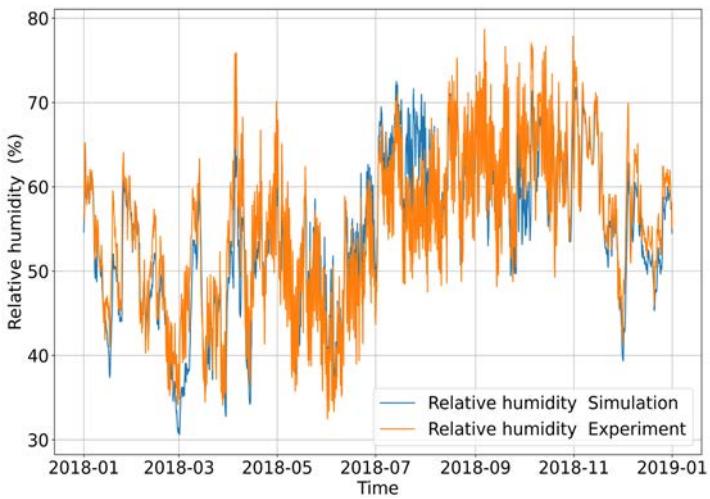

Fig. 2. Comparison of humidity numerical simulation with experimental data.

Since the mean absolute error is less than 3.49 and considering that the accuracy of the sensor (model sht75) is ±1.8, additional measurements could be affected by imprecise placement in a given material as well. It can be assumed that the simulation represents well the building dynamics.

The simulation allows evaluating how the temperature and water content change in each building wall layer, even where sensors are not installed. For example, the simulation in Fig. 3 provides information on how the water content changes in cement-lime plaster in the middle of the wall.

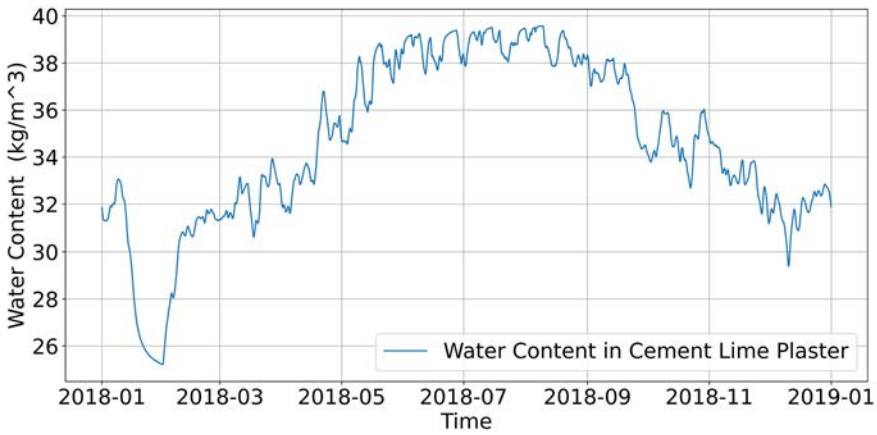

Fig. 3. Cement-lime plaster water content change.

The moisture content change is ~13$\frac{kg}{m^3}$ depending on external conditions. In turn, by analysing the temperature results, the software indicates that the temperature change for this layer is from 0 to 26 degrees.

As mentioned earlier, WUFI material database has defined behavioural functions λ (T, w) (where T is temperature and w is moisture content) for each material (see Fig. 4) as an example.

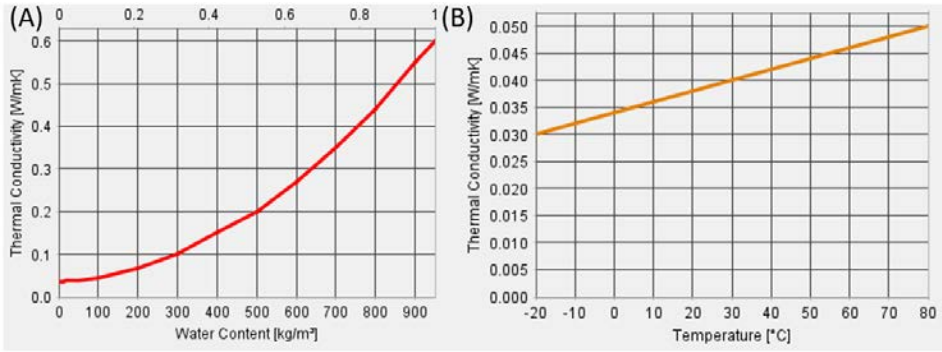

Fig. 4. Dependencies of λ defined in WUFI for Roxul Plus, where:
(A) represents λ as a function of water content at 10 °C and
(B) represents dry material λ as a function of temperature.

Knowing the changes in temperature and water content, based on the behavioural functions of materials defined in WUFI, λ can be calculated at the minimum λ_(min) and at the maximum λ_{max} thermal conductivity for each layer according to Eq. (1) [15].

$$\lambda(T, w) = \lambda_{dry}(T) * (1 + c_1(w) * w), \qquad (1)$$

where in our case $c_1(w)$ is a constant representing the ratio of thermal conductivity supplement to the bulk density of dry building material [15]. Then, to evaluate the impact of λ change in each material, the material thickness must be considered. Since the thickness of each layer is known, it is possible to calculate how the thermal resistance (R) of each layer changes (see Table 1).

Table 1. The Change in Heat Resistance of the Wall Layers in Each Material

Material	Roxul Facaderock	Roxul Plus	Plaster	Aerated concrete	Plaster
λ_{max}	0.0398	0.0334	0.04573	0.1155	0.0453
λ_{min}	0.0306	0.0325	0.03754	0.107	0.0422
$R_{min}\left(\frac{m^2K}{W}\right)$	0.7533	1.4968	0.32799	3.2478	0.3309
$R_{max}\left(\frac{m^2K}{W}\right)$	0.9804	1.5384	0.3995	3.5047	0.3554

By summarising all results from Table 1, it can be concluded that the thermal resistance of a given wall can vary from $6.156\left(\frac{m^2K}{W}\right)$ to $6.778\left(\frac{m^2K}{W}\right)$, a difference of close to 10 %. U value change is linearly proportional to thermal resistance. It is known that heat flux inside the walls in the stationary case can be described as:

$$Q = \Delta TU. \quad (1)$$

This means that heat flux in the building in the given case could change by up to 10 % simply due to changes in the material properties of the building construction.

It is important to note that this structure is well designed to prevent moisture accumulation. However, in older buildings, especially after renovation, moisture accumulation could be even bigger and, as a result, seasonal changes in U will be even greater [16].

3. HEAT FLUX DATA PRE-PROCESSING

For U value measurements in a building, several authors used heat flux measurements in combination with temperature sensors [17], [18]. For the dynamic evaluation of U value changes, heat flux sensors (W 150-s) were installed on the wall, whose properties were evaluated in the previous paragraph. The details about monitoring system for heat flux measurements could be found in [19]. For delta temperature evaluation, the temperatures used were the weather station temperature and the temperature from sensor (sht35) located in the middle of the room. The monitoring system time resolution is 1 min. If the U value is computed for one year, at each point, according to Eq. (1), high nonphysical values appear on the plot (see Fig. 5).

Knowing the thermal resistance, we can calculate U value – in our case, the maximum and minimum U are 0.162 and $0.147\left(\frac{W}{m^2K}\right)$. As can be seen in Fig. 5, large peaks occur during the summer, and several values are also negative. This is because heat flow can reverse direction in summer. In addition, situations may occur where the temperature difference is very small, but the building has inertia and, therefore, the flow inside the structure might still change – resulting in very high values. This is why some authors use averaging for U value measurements and choose time periods across which heat flow is more or less stable [18]. Unfortunately, such a processing method is not suitable for building control since dynamic data are necessary for MPC.

At the same time, usage of data with pronounced peaks is also ineffective. After normalization, smaller values that carry important real information for the NN model will be difficult to notice because they are significantly lower than the peak values – as a result, the range of the activation function data that carry the information will be very small. Therefore, another data processing method is required.

To remove high values, absolute values of temperature difference and heat flow could be used to avoid negative values. To smooth out the curve, an average moving window of one week is applied, and the result can be seen in Fig. 6.

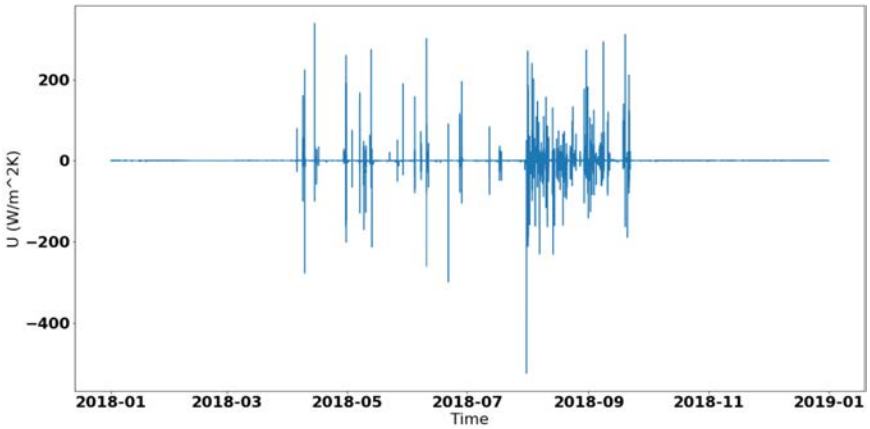

Fig. 5. Instant U value.

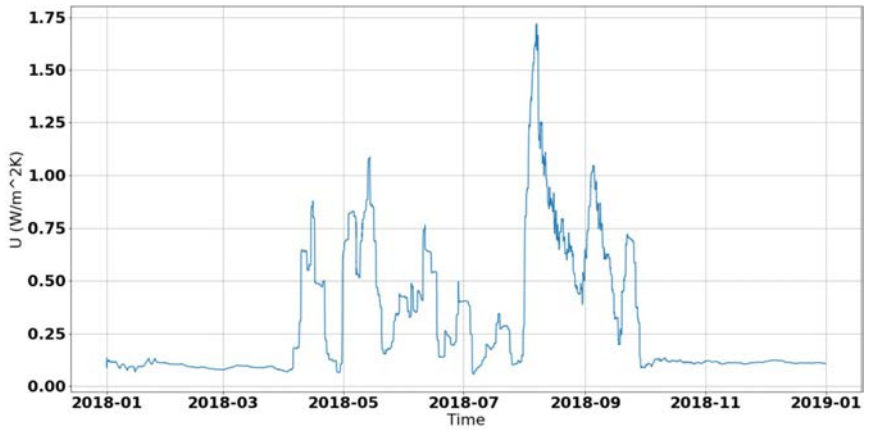

Fig. 6. Absolute U value result with sliding window.

In Fig. 6, the value of U now exhibits a much lower amplitude. During the heating season (October to April), U is close to physical values. On the other hand, during periods when there is no heating, the values are far from those calculated previously due to spikes in the data.

The data intervals in which the flow direction has stabilized may be taken into account to filter out noise. To do this, data

with a temperature difference greater than 3 degrees were selected. Calculating the average moving value with a window over the week gave the result shown in Fig. 7.

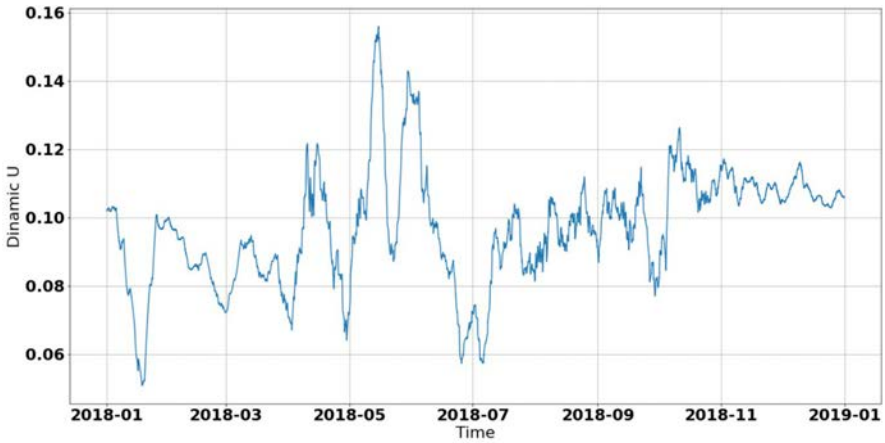

Fig. 7. Absolute U value result after filtration of small values.

After processing, the amplitude of U is ~ 14 times lower. Although the calculated dynamic value of U is not the same as U calculated in the stationary case, the theoretical mean value of U 0.15 ($\frac{m^2K}{W}$) is close to the mean dynamic value of 0.11 ($\frac{m^2K}{W}$). It is known that a large number of input parameters can negatively impact both NN training time and accuracy [20]. It is important to note that this value is represented by one number, which requires a large matrix (in this case it has more than ~ 10^4 elements), as well as a function, which in the case of NN needs to be determined. Thus, the method significantly reduces the input data array and simplifies the function which NN is fitting.

4. EVALUATION OF DYNAMIC U WITH NN

Determining the optimal NN hyperparameters is still an unresolved problem in neural networks. The universal approximation theorem states that an NN with a linear output layer and at least one hidden layer with any activation function (e.g., a sigmoid activation function) can approximate any function from one finite dimensional space to another with any desired non-zero error value, if enough hidden units are allocated [19]. In turn, only linear functions can be approximated by NN with only one layer. It is known that the number of neurons in the output layer must be equal to the desired number of predictive values.

4.1. Fully Connected NN

For the initial test of proposed input parameter, a fully connected architecture was chosen. Such an architecture usually provides a smoother convergence curve comparing to the recurrent neural network architectures, which would require training

a higher number of models to obtain objective average results. Looking at the articles describing the newly developed NN models for the evaluation of building dynamics, it was noticed that for similar purposes, full-layer models with 3–5 layers are used, in which the number of input neurons is equal to the number of input parameters [21]–[24]. For future tests, a model with one hidden layer was selected. The number of hidden units was chosen as the average of input and output parameter quantities. Since even non-deep fully connected models can contain a large number of optimized parameters, the input data length was limited to 3 hours. As a target forecast value, the inner temperature data from the sensor located at the middle of the room were selected. The forecast length was defined as 30 minutes. Mean squared error was used as the optimization metric.

During the evaluation, it is important to keep the same architecture, otherwise it could lead to an incorrect evaluation output. It is therefore important keep the same amount of input data to NN to evaluate the impact of a proposed input parameter on the forecast. For this purpose, to compare NN performance with and without a proposed input parameter, a random value was used in place of the dynamic U value. In this comparison, data from several sensors were used, as illustrated in Fig. 8.

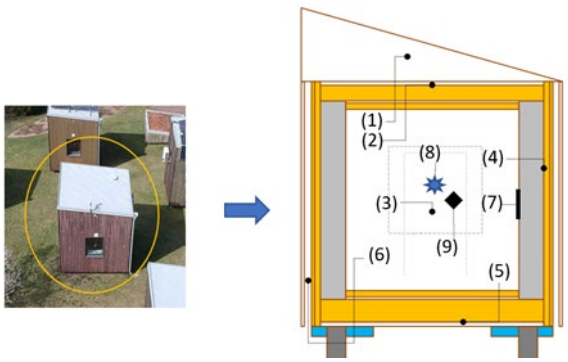

Fig. 8. Distribution of sensors in the building, where: (1–6) are temperature/humidity sensors; (7) is a heat flux sensor, (8) is a solar radiation sensor placed at the front of the window, and (9) is an anemometer.

The heat flux sensor data were used only for dynamic U value calculation. Other sensor data in combination with the weather station data (temperature, humidity, wind speed, direction, and solar radiation) were used as input parameters in both models: with dynamic U value and when it was replaced by random values.

Before model training, wind data from the weather station were pre-processed for better representation to NN. For this purpose, wind direction and wind speed were combined and represented as x and y wind components. Then, all values were normalized between 0 and 1.

It is known that the initial weight initialization could impact the final result given by the NN [25]. Thus, the mean values of several modes must be evaluated in order to obtain objective results. For this reason, for each input parameter configuration, ten models were trained.

One of the common problems with the training of neural networks is overfitting [26]. To evaluate overfit of models, all three years of monitoring data were split into two

years of training data and one year of validation data. To prevent model overfitting, an early stopping function was defined. The function stops training if loss metrics stop getting better by the 300th epoch, and save the best weights based on validation dataset performance.

The mean results of several models training on the validation dataset with a dynamic U value and one replaced with random values are seen in Fig. 9.

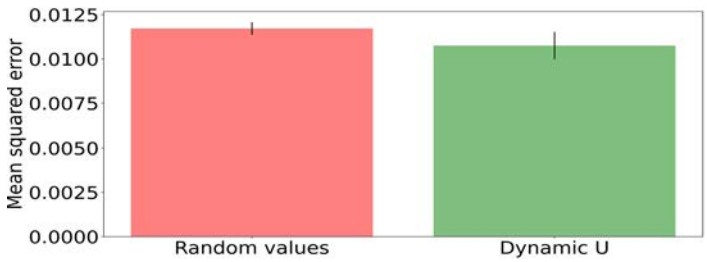

Fig. 9. Evaluation of dynamic U with a fully connected NN.

The presented results are calculated when inlet air enters perpendicular to the front side of inlet ventilation. The results of simulation analysis are shown for a physical time of 5 seconds with all the elements having the same set of boundary conditions and the values as those described in the previous section. Longer physical time in the analysis will require longer computations time to get the results because this is a transient phenomenon. This means time will have influence on the results but since it is comparison the change will be approximately similar for all the cases. Hence, a smaller physical time of 5 seconds is chosen for the study in order to save computation time because the differences in the results would be nearly identical at any given time. The results are obtained in terms of pressure and surface temperature of the body. These results are discussed and presented below.

4.2. Temporal Convolution Model

The model observed hereinabove does not consider data sequence. For time-series data, a recurrent neural network (RRN) is often used [27]. Unfortunately, even RNN architectures such as long short-term memory (LSTM) could miss information in case of a long input data sequence [13]. One of the modern trends for long time series data processing is the usage of 1D convolution. Results from other authors have shown that architectures such as temporal convolution networks (TCNs) could have better inner memory and outperform techniques such as LSTM [13]. This architecture was selected for the evaluation of a proposed input parameter when a much longer data sequence is used as input.

In contrast to the previous experiment, the selected input data length was 1 week (the length of each measurement vector is more than ~ 10^4 elements). Since this model is not as sensitive to the number of input parameters, the decision was made to use a dynamic U value sequence instead of a single value as previously. Because in this case the input data sequence is long enough to evaluate U value by itself, three evaluations were performed, which, apart from

all other measurements, included: heat flux data, dynamic U value and vector with random values.

Since this architecture does not converge with stochastic gradient descent (SGD), the Adam adaptive optimizer was chosen. The Adam convergence curve has large fluctuations, compared to previously used SGD. To obtain objective results, the decision was made to train 30 models for each input configuration. An early stopping function was defined as described above. The results are shown in Fig. 10.

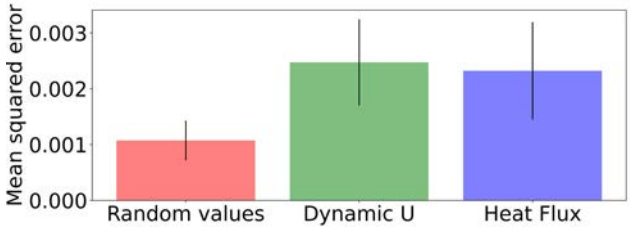

Fig. 10. Evaluation of dynamic U and heat flux data input with a TCN architecture.

Looking at the results in Fig. 10, one can conclude that in case of TCN architecture, dynamic U and heat flux data do not improve the inner climate forecast. It is important to note that if these values did not contain any beneficial information for NN, it would provide the same result as with random values. However, results in Fig. 10 show that the mean squared error becomes higher when these values are used as input. One possible explanation for this is that additional input parameters do not provide useful information in all cases, and NN could not detect cases where this information must be used.

5. RESULTS AN DISCUSSION

An initial evaluation using numerical simulation in WUFI Pro demonstrated that, for the chosen construction, heat flux in the walls could vary by up to 10 % given the same temperature difference due to U-value changes as a function of temperature fluctuations and moisture transfer. Since the mean absolute error of the numerical simulation humidity forecast in the specific building construction layer is 3.49 % compared to physically measured values, it can be assumed that the numerical simulation accurately represents the building dynamics.

To measure the U-value in real time, data processing techniques for temperature and heat flux measurements were introduced. The average dynamic U-value, 0.11 ($\frac{m^2K}{W}$), obtained from the processing of annual measurements, is close to the result from the numerical simulation, 0.15 ($\frac{m^2K}{W}$). It is important to note that, due to the chosen data processing technique, the dynamic U-value does not represent the real U-value of the construction, but rather indicates its change over time.

To evaluate the dynamic U-value as an input parameter for neural networks (NN), two NN architectures were employed. The average result of a fully connected model

trained 10 times with different starting weights suggested that the use of dynamic U-values reduced the mean squared error to approximately 8.5 % on average. Meanwhile, the average result of 30 trained temporal convolutional network (TCN) models indicated that the use of dynamic U-values, as well as raw heat flux data, only increased the mean squared error to 0.00125 and 0.0014, respectively.

6. CONCLUSIONS

The results obtained through numerical modelling indicate the feasibility of using dynamic U-value measurements, as it can point to changes that significantly affect heat transfer in a building. To obtain the U-value in real time, a data pre-processing method was introduced for filtering out large values. Notably, the resulting dynamic heat transfer coefficient value does not represent the actual value of the construction heat transfer coefficient but may reflect its change over time.

To evaluate the impact of the proposed input parameter on the building indoor climate forecast, fully connected and temporal convolution neural networks were used. The results showed that, in the case of the fully connected neural network, the mean squared error decreased by more than 8 % when the dynamic U-value was used. However, with temporal convolution neural networks, using the dynamic U-value and raw heat flux data results in a higher mean squared error compared to when random values are employed instead. This neural network behaviour may be due to its inability to discern when to utilize this information. This finding motivates further research towards developing modifications to the temporal convolution model for analysing building dynamics, as this architecture exhibits a lower mean squared error according to the results obtained.

ACKNOWLEDGEMENTS

This study has been conducted with the financial support of ERAF project "Development and Approbation of Complex Solutions for Optimal Inclusion of CHE in Nearly Zero Energy Building Systems and Reduction of Primary Energy Consumption for Heating and Cooling" (1.1.1.1./19/A/102). The authors would also like to express gratitude to Mihails Birjukovs for consultations about moisture transfer.

REFERENCES

1. Lallouche, A., Kolodyaznaya, V., Boulkrane, M. S., & Baranenko, D. (2017). Low Temperature Refrigeration as an Alternative Anti-Pest Treatment of Dates. *Environmental and Climate Technologies*, *20*, 24–35. https://doi.org/10.1515/rtuect-2017-0008.
2. Cao, X., Xilei, D., & Liu, J. (2016). Building Energy-Consumption Status Worldwide and the State-of-the-Art Technologies for Zero-Energy Buildings during the Past Decade. *Energy and Buildings*, *128*, 6.

3. Klepeis, N., Nelson, W., Ott, W., Robinson, J., Tsang, A., Switzer, P., … & Engelmann, W. (2001). The National Human Activity Pattern Survey (Nhaps): A Resource for Assessing Exposure to Environmental Pollutants. *Journal of Exposure Analysis and Environmental Epidemiology, 11*, 231–52.
4. Lee, D., & Cheng, C.-C. (2016). Energy Savings by Energy Management Systems: A Review. *Renewable and Sustainable Energy Reviews, 56*, 760–777.
5. Wabersich, K.P., & Zeilinger, M.N. (2020). Performance and Safety of Bayesian Model Predictive Control: Scalable Model-Based RL with Guarantees. *ArXiv,* abs/2006.03483.
6. Abioye, S., Oyedele, L., Akanbi, L., Ajayi, A., Davila Delgado, M., Bilal, M., … & Ahmed, A. (2021). Artificial Intelligence in the Construction Industry: A Review of Present Status, Opportunities and Future Challenges. *Journal of Building Engineering, 44, 103299.*
7. Kolokotsa, D., Pouliezos, A., Stavrakakis, G., & Lazos, C. (2009). Predictive Control Techniques for Energy and Indoor Environmental Quality Management in Buildings. *Building and Environment, 44 (9), 1850–1863.*
8. Oldewurtel, F., Parisio, A., Jones, C.N., Gyalistras, D., Gwerder, M., Stauch, V. … & Morari, M. (2012). Use of Model Predictive Control and Weather Forecasts for Energy Efficient Building Climate Control. *Energy and Buildings, 45, 15–27.*
9. Kalogirou, S.A. (2001). Artificial Neural Networks in Renewable Energy Systems Applications: A Review. *Renewable and Sustainable Energy Reviews, 5 (4), 373–401.*
10. Afroz, Z., Shafiullah, G., Urmee, T., & Higgins, G. (2017). Prediction of Indoor Temperature in an Institutional Building. *Energy Procedia, 142, 1860–1866.*
11. Kalogirou, S.A. (2001). Artificial Neural Networks in Renewable Energy Systems Applications: A Review. *Renewable and Sustainable Energy Reviews, 5 (4), 373–401.*
12. Siami-Namini, S., Tavakoli, N., & Namin, A.S. (2019). The performance of LSTM and BiLSTM in forecasting time series. In *2019 IEEE International Conference on Big Data (Big Data)* (pp. 3285–3292). doi: 10.1109/BigData47090.2019.9005997.
13. Lara-Benítez, P., Carranza-García, M., Luna-Romera, J., & Riquelme, J. (2020). Temporal Convolutional Networks Applied to Energy-Related Time Series Forecasting. *Applied Sciences, 10, 2322.*
14. Vereecken, E., & Roels, S. (2012). Review of Mould Prediction Models and their Influence on Mould Risk Evaluation. *Building and Environment, 51*, 296–310.
15. Künzel, H. (1995). *Simultaneous Heat and Moisture Transport in Building Components: One-and Two-Dimensional Calculation*. Fraunhofer.
16. Prozuments, A., Staveckis, A., Zemitis, J., & Bajare, D. (2021). Evaluation of Heating and Cooling Loads for a Well-Insulated Single-Family House under Variable Climate Pattern. *Environmental and Climate Technologies, 25,* 750–763. 10.2478/rtuect-2021-0056.
17. Ficco, G., Iannetta, F., Ianniello, E., Romana d'Ambrosio Alfano, F., & Dell'Isola, M. (2015). U-Value in Situ Measurement for Energy Diagnosis of Existing Buildings. *Energy and Buildings, 104, 108–121.*
18. Márquez, J.A., Bohórquez, M.M., & Melgar, S. G. (2017). A New Metre for Cheap, Quick, Reliable and Simple Thermal Transmittance (U-Value) Measurements in Buildings. *Sensors, 17 (9).*
19. Telicko, J., Jakovics, A., & Drikis, I. (2019). A Low-Cost Wireless Sensor Network for Long-Term Monitoring of Energy Performance and Sustainability of Buildings. *MATEC Web of Conferences, 282,* 02039. 10.1051/matecconf/201928202039.
20. Goodfellow, I., Bengio, Y., & Courville, A. (2016). *Deep learning. Adaptive computation and machine learning.* MIT Press.
21. Dombaycı, A. (2010). The Prediction of Heating Energy Consumption in a Model House by Using Artificial Neural Networks in Denizli–Turkey. *Advances in Engineering Software, 41* (2), 141–147.

22. Gao, M., Sun, F.Z., Zhou, S.-J., Shi, Y.-T., Zhao, Y.-B., & Wang, N.-H. (2009). Performance Prediction of Wet Cooling Tower Using Artificial Neural Network under Cross-Wind Conditions. *International Journal of Thermal Sciences, 48* (3), 583–589.
23. Escamilla-García, A., Escamilla-Garc´ıa, G., Soto-Zarazúa, M., Toledano-Ayala, M., Rivas-Araiza, E., & Gastélum -Barrios, A. (2020). Applications of Artificial Neural Networks in Greenhouse Technology and Overview for Smart Agriculture Development. *Applied Sciences, 10* (11).
24. Kalogirou, S. A. (2001). Artificial Neural Networks in Renewable Energy Systems Applications: A Review. *Renew. Sustain. Energy Rev., 5*, 373–401.
25. Zhou, Q., & Ooka, R. (2021). Performance of Neural Network for Indoor Airflow Prediction: Sensitivity towards Weight Initialization. *Energy and Buildings, 246*, 111106.
26. Liu, Y., Starzyk, J.A., & Zhu, Z. (2008). Optimized Approximation Algorithm in Neural Networks Without Overfitting. *IEEE Transactions on Neural Networks, 19* (6), 983–995.
27. Hochreiter, S., & Schmidhuber, J. (1997). Long Short-Term Memory. *Neural Computation, 9 (8), 1735–1780.*

sciendo

LATVIAN JOURNAL OF PHYSICS
AND TECHNICAL SCIENCES
2023, N 6

DOI: 10.2478/lpts-2023-0048

POROUS MATERIAL FOR GAS THERMAL COMPRESSION IN SPACE CONDITIONS: THERMAL DESIGN ASPECTS

I. Ušakovs[1]

[1] Allatherm SIA,
3 Pulka Str., Riga, LV-1007, LATVIA
E-mail: igors.usakovs@allatherm.com

It is almost impossible to name a field of human activity where porous materials are not used. Filters, membranes, thermal insulators, fuel cells, catalysts, wicks of heat transfer devices, sorbents, textiles, and other examples of porous materials explain such an increased interest in the study of their properties, design of new materials, and development of technologies for their manufacture. The recent need for in-orbit spacecraft refuelling has led to the development of gas thermal compression technology based on the use of porous material as both a fuel retention mechanism and thermal interface. The present paper reveals the thermal aspects of porous material design for a device intended for pumping xenon, fuel for ion thrusters, in zero-gravity conditions – Xenon Refuelling Compressor.

Keywords*: Gas thermal compression, metal felt, metal fibres, nonwoven porous materials, porous media, porous media models, thermal conductivity of porous materials.*

1. INTRODUCTION

The gas thermal compression principle is easy to understand by considering the operational cycle of a gas thermal compressor (TC). The compressor function is to increase the pressure of fluid (for the sake of generalization, the author will further use the term “fluid” rather than “gas”) taken from Servicer (S) tank to a pressure exceeding the one in Client (C) tank, allowing for fluid transfer into the C tank.

Therefore, the compressor is switched on at the moment when the pressure P_s in the S tank becomes lower than the pressure P_c in the C tank and the fluid can no longer flow from S to C naturally, due to pressure head. TC operational cycles consist of alternating cooling (charging) and heating (discharging) stages. At the cooling stage,

thermal compressor (TC) is hydraulically connected to the S tank and disconnected from the C tank (Fig. 1a). Pressure in the compressor decreases below P_s with temperature decrease and fluid fills the compressor and condenses. The compressor is charging. At the following heating stage, TC is disconnected from the S tank and connected to the C tank. Pressure inside the compressor increases with temperature rise, becomes higher than P_c and fluid transfers into the C tank (Fig. 1b). The compressor is discharging. During the next step, the compressor disconnects from the heater and connects to the cooler again and returns to the initial state for transferring the next amount of fluid. It means that the compressor operates in repeated cycles transferring portions of fluid from the low-pressure tank to the high-pressure tank. Simplified, single cycle consists of two isobars and two isochores.

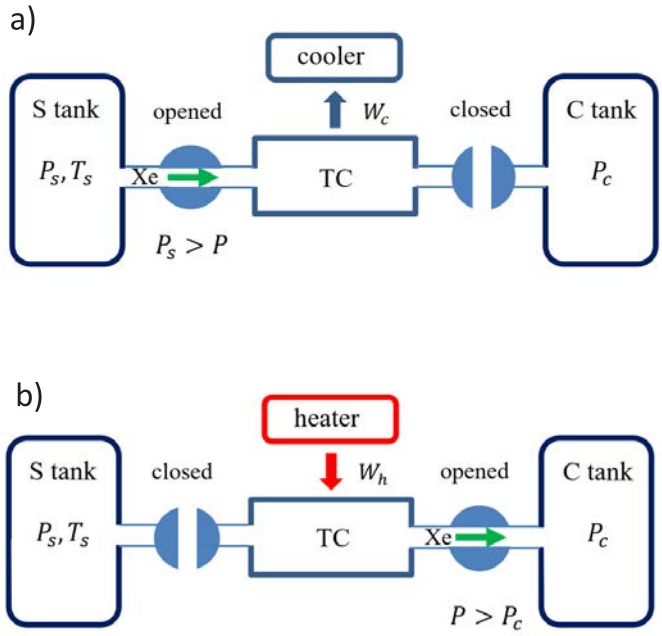

Fig. 1. Thermal compressor operation: a) charging stage, b) discharging stage.

2. GENERAL REQUIREMENTS FOR POROUS MATERIALS INTENDED FOR THERMAL COMPRESSORS

As it is clear from the description above, the compressor is essentially a heat exchanger (HX). Therefore, the design of the compressor should be guided by the characteristics of a good HX, considering the features of its operation in space. First, its internal structure must ensure the efficient heat exchange between the cooling/heating system and fluid. For that purpose, the heat exchange surface should be created inside the compressor. Second, taking into account that the compressor operation

is planned in zero-gravity conditions, there must be some arrangement inside the compressor, which will provide the fluid retention mechanism. A porous body (PB), for example, made of high thermal conductive material, can work in the capacity of such arrangement. On the one hand, pores have a large surface area available for heat transfer; on the other hand, they can hold fluid by capillary forces. In this case, the material must be well wetted by the fluid. The above leaves no alternative except for the use of a highly thermally conductive metal, such as copper, to produce the porous structure. The PB can be made of metal powder or metal fibres by sintering in vacuum. The leading parameter of porous materials is porosity φ, which is the fraction of pore volume V_p to the total volume V of the PB.

$$\varphi = \frac{V_p}{V} = \frac{V - V_m}{V} = 1 - \frac{m}{\rho_m \cdot V}, \quad (1)$$

where V_m, m, ρ_m – volume, mass and density of the pure material used for PB fabrication. In space, the mass and dimensions of the devices used are of great importance, so these parameters must always be optimized in the design. For a compressor, this means that the proportion of retained fluid per unit mass must be maximized. This means that the porosity of the PB must be high. With powders it is difficult to obtain porosity greater than 60 %, which is not the case with metal fibres. Fibre structures can reach porosities of more than 90 %. In this case, as it will be shown below, thermal conductivity and structural strength become the limiting factors. It was experimentally obtained that the optimal value of porosity was ~80 %. Several models of the compressor were manufactured with this structure inside [1]. The choice of thermal compression technology for pumping of fuel is also due to the extreme requirements for molecular and particulate contamination. The compressor in this case is a passive device that cannot introduce contamination unless its structural elements react chemically with the fuel or if some particle of the structure breaks off. The probability of particulate contamination for powder sintered material is significantly higher than for material made of metal felt. Also, the sintering of powder can form useless closed pores that are not accessible to filling of fluid, which is not possible for metal fibres. All these considerations do suggest that the PB should be made of metal felt with high thermal conductivity.

3. THERMAL PARAMETERS OPTIMIZATION

The parameters that determine the thermal characteristics of a porous material are specific heat capacity c, density ρ, and thermal conductivity λ. There is not much we can do with the first two, since they are determined by the chosen material and porosity, while the thermal conductivity is highly dependent on the PB structure. Density:

$$\rho = \rho_m \cdot (1 - \varphi). \quad (2)$$

Specific heat capacity is equal to the specific heat capacity of the felt material c_m :

$$c = c_m. \quad (3)$$

The production of a porous structure consists of three steps: selection of the material with the required parameters, moulding, and sintering. Each of the steps leaves its own mark on the final properties of the material. To obtain a material with the desired properties it would be good to

simulate these properties in one way or another. However, many conclusions can be drawn without complex modelling using a qualitative analysis based on general physical considerations. First, the problem is immediately simplified by its formulation. We need to design a material so that it has maximum thermal conductivity at a given porosity. The starting material should be copper fibres. Regardless of the structure, porous materials have the property that the upper limit of apparent thermal conductivity λ_{max} is determined by their porosity φ and the thermal conductivities of the material λ_m and the fluid filling the pores λ_p. (In reality, heat inside a PB can be transferred not only by heat conduction, but also by convection and radiation inside the pores. If the pores are small enough and there are no large temperature gradients inside the PB, as in the case of our interest, these types of heat transfer can be neglected.) The apparent thermal conductivity will reach its maximum value if the conductance of each phase simply adds up. Using Fourier's law this can be written mathematically as follows:

$$\lambda_{max} \cdot \frac{\Delta T}{L_0^2} \cdot L_0 \cdot S = \lambda_m \cdot \frac{\Delta T}{L_0^2} \cdot L_0 \cdot S_m + \lambda_p \cdot \frac{\Delta T}{L_0^2} \cdot L_0 \cdot (S - S_m). \quad (4)$$

Here, a piece of material with cross section S perpendicular to the heat flux and length L_0 is taken for the sample. Thus, the volume of the piece is $V = L_0 \cdot S$ and S_m is total cross sections of solid substance (copper). Taking into account that for copper the condition $\lambda_m \gg \lambda_p$ is fulfilled and the second summand in (4) can be neglected, expression (4) can be rewritten through volumes with help of (1) in the form:

$$\lambda_{max} \cdot \frac{\Delta T}{L_0^2} \cdot V \approx \lambda_m \cdot \frac{\Delta T}{L_0^2} \cdot (1 - \varphi) \cdot V. \quad (5)$$

(Here on purpose both sides are not reduced by $\frac{\Delta T}{L_0^2} \cdot V$, because in this form we will need expression (5) for further reasoning.) Thus, the maximum thermal conductivity that can be obtained from the fibre is determined only by the porosity:

$$\lambda_{max} \approx \lambda_m \cdot (1 - \varphi). \quad (6)$$

As can be seen from (1), the mass of the used fibres is also determined only by the porosity. Consequently, the structure with maximum thermal conductivity should only contain fibres oriented along the heat flow. Each fibre oriented transversely does not transfer heat but occupies useful volume. The pore space is formed by the gaps between the fibres, and they also serve as capillaries holding the condensed fluid. An ideal structure in this sense is shown in Fig. 3b. Over the last 150 years of study of porous materials, dozens of expressions for calculating frame thermal conductivity were derived ([2], [3]). Most of the expressions have a narrow field of applicability and represent thermal conductivity as a function of porosity and thermal conductivity of pure material. In fact, the expression for thermal conductivity must also contain microstructural parameters such as fibre thickness (diameter) and individual fibre length l. For example, in [4], a correlation of porosity and thermal conductivity on the fibre aspect ratio was established, from which it follows that longer and thinner

fibres are desirable. The influence of fibre length can be qualitatively explained by considering the skeleton of a porous structure sintered from randomly oriented fibres, which is the case for most metal-fibre materials. Heat is transferred through both the fibre body and the contact spots between them (see Fig. 3a). The contact thermal resistance of the contact spots is difficult to predict although there are various attempts of modelling them. It is determined by the sintering parameters. The shorter the fibres, the more contact points in the heat path, the worse the thermal conductivity. The influence of contact resistances is well described in [5]. It contains a rather extensive experimental and analytical study of porous copper and steel fibre materials of different porosity developed at the Fraunhofer Institute, including numerical modelling of the porous structure geometry based on micro-computed tomography (ICT) images of real material. The heat transfer was then modelled by Lattice Monte Carlo [6] and Finite Element methods. The thermal conductivity was also calculated using several analytical relationships. The experimental results showed a significant discrepancy with the models for porosity below 60 %, which was explained by not considering the contact resistance between the fibres, the number of which logically increased with decreasing porosity. Summarising the above, it can be concluded that in order to form a good structure, it is desirable to use a material with long, or better even continuous, fibres, such as the one shown in Fig. 2.

Fig. 2. Copper yarn with continuous 20 thick filament.

The second important parameter is the fibre diameter *d*. As mentioned above, it is necessary to create a heat exchange surface inside the compressor. It is not difficult to show that the heat exchange surface per unit volume S_h depends on the fibre diameter and porosity as follows:

$$S_h = \frac{4}{d}(1-\varphi). \tag{7}$$

The same relationship determines the length of the wetted perimeter, which is the guiding factor for the capillary properties of the material. As can be seen from (7), the above-mentioned material properties improve with decreasing fibre diameter. Thus, it is better to select a continuous fibre with the smallest possible diameter to fabricate the structure. We managed to find fibre

with a thickness of 20 microns. The experience of its use shows that this size is optimal, because with a thinner fibre there may be difficulties related to felting and the subsequent moulding of the structure for sintering, as well as with the strength of the PB.

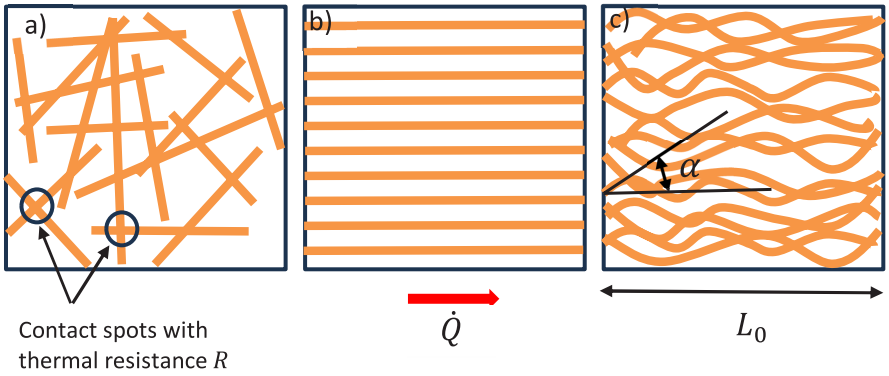

Fig. 3. Three patterns of fibrous porous structures: a) randomly oriented fibres, b) porous structure with maximum thermal conductivity, c) real structure with oriented felt direction.

Obviously, it is impossible to produce a PB corresponding to the ideal structure shown in Fig. 3b, consisting only of fibres directed in parallel of the heat flow. Some number of transverse fibres forming the structural skeleton must be present. By applying the technique of directional felting, it is possible to obtain a structure like the one shown in Fig. 3c, where the individual fibres are intertwined to form a spatial skeleton but retaining in general a given direction. The deviation of the fibres from the heat flow direction can be characterised by some angle α randomly distributed in some range $[0, \alpha_{max}]$, where $\alpha_{max} \leq {}^{\pi}/_{2}$ and can be controlled by the width of single strand. The thermal conductivity of the obtained structure will be less than the maximum (6) due to two reasons. First, as the fibre length L increases, the path passed by the heat through the PB increases, which can be written as:

$$L = \frac{L_0}{cos\,(\alpha)}. \tag{8}$$

Second, since the mass of fibres per unit volume for a given porosity is fixed, the number of fibres per unit volume will decrease with fibre elongation. Both factors will be automatically taken into account if L from (8) is substituted into the right-hand side of expression (5) instead of L_0. Reducing both sides by $\frac{\Delta T}{L_0^2} \cdot V$, we obtain an expression for thermal conductivity depending on the α angle:

$$\lambda = \lambda_m \cdot (1 - \varphi) \cdot cos^2(\alpha) = \lambda_{max} \cdot cos^2(\alpha)\,. \tag{9}$$

To obtain the final expression for the thermal conductivity of the material, it is necessary to average expression (9) over the α angle in the range of its variation:

$$\bar{\lambda} = \frac{\lambda_{max}}{\alpha_{max}} \cdot \int_0^{\alpha_{max}} cos^2(\alpha)\, d\alpha = \frac{\lambda_{max}}{2 \cdot \alpha_{max}} \left[\alpha_{max} + \frac{1}{2} sin\,(2 \cdot \alpha_{max})\right]. \tag{10}$$

In the worst case, assuming $\alpha_{max} = \pi/2$ we obtain the minimum value of thermal conductivity:

$$\bar{\lambda}_{min} = \frac{1}{2}\,\lambda_{max}. \quad (11)$$

4. MODELLING OF POROUS MEDIA

If the formalism described above gives the correct dependence of the thermal conductivity of PB on the angle α, this should be confirmed by calculations based on PB computer models. The construction of such a model is also of independent interest, since it allows modelling more complex processes than heat transfer along the PB frame, for example, fluid flow through pores or heat exchange between fluid and porous structure. In our particular case, the porous structure is a composition of continuous, oriented and bending fibres. Orientation is provided by constraining the angle α:

$$0 \le \alpha \le \alpha_{max}. \quad (12)$$

In addition to condition (12), the model must take into account the random arrangement of each fibre in space and the arbitrariness in the number of bends in each of the fibres. The presence of a random process in the formation of the structure suggests that in order to build an adequate material model it is necessary either to use a sufficiently large volume containing a sufficiently large number of fibres, or to create an ensemble of models with a small number of fibres. In the first case, the averaging of parameters will happen automatically. In the second case, the result must be averaged over the ensemble. Obviously, the choice between the approaches depends on the computational capabilities of used hardware. It is easy to calculate that, for example, an element of a structure with a volume of 1 mm^3 at a porosity of 80 % will contain > 300 fibres with a diameter of 20 microns (depending on the α_{max} angle). Therefore, a control volume of 0.25 mm^3 at a material porosity of 90 % was taken as a first approximation for PB model. This allowed us to limit the number of fibres to 50–80 pieces per control volume. To build the models, a script was written in the Python programming language, the interpreter of which was embedded in the SpaceClaim 3D CAD of the CAE ANSYS. As input parameters, the script received α_{max}, porosity φ, and the length L of the side of the cube simulating the control volume. Then the total length of fibres L_f in the volume will be equal to

$$L_f = (1-\varphi)\cdot\frac{4\cdot L^3}{\pi\cdot d^2}, \quad (13)$$

where d is a fibre diameter.

The process of porous structure generation is illustrated in Fig. 4. Here it is assumed that the fibres are oriented along the Z axis. Then each fibre starts at an arbitrary point M_0 of the XY plane. The coordinates of the point M_0 are calculated using a random number generator:

$$\begin{cases} M_{0,x} = rand[d, L-d] \\ M_{0,y} = rand[d, L-d] \end{cases}. \quad (14)$$

In (14), the offset from the edges by the fibre diameter is artificially introduced so that the beginnings of the fibres do not fall on the boundaries of the cube face. This assumption cannot spoil the result, since it is the number and length of the fibres that matters, not their location. Another simplification is made taking into account that we consider highly porous structures, so in the first approximation we can ignore the possible coincidence or intersection of fibres, which, of course, is impossible to obtain in practice.

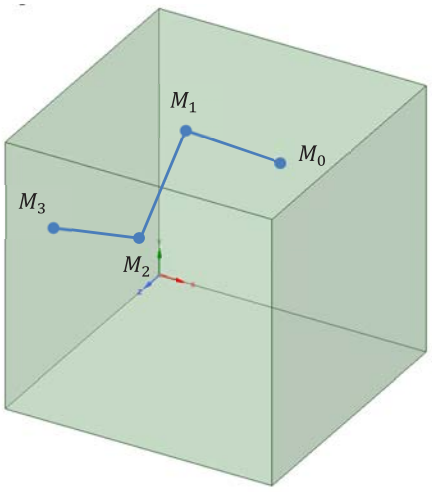

Fig. 4. Creation of a single fibre.

The points $M_1, M_2, M_3, \ldots$ correspond to the bending points of the fibre. The coordinates of point M_1 and subsequent points are obtained as follows. Let us introduce the notation $\overrightarrow{M_0M_1} = \vec{m}$. Then condition (12) can be written in the form

$$\cos(\alpha_{max}) \leq \frac{m_z}{m} \leq 1, \tag{15}$$

where the designation $m = |\vec{m}|$ is introduced and m_z means Z component of $\vec{m}$. Next, we will make the assumption that the length m of the section between two bends is also bounded by some interval, which can be reasonably measured in number of fibre diameters:

$$k_1 \cdot d \leq m \leq k_2 \cdot d, \tag{16}$$

where k_1 and k_2 are integers, some design parameters on which, if the theory in the previous paragraph is correct, thermal conductivity should not depend. However, their choice may affect other parameters of the structure, such as permeability. The measurement of length in diameter is also convenient for scaling the structure, for example, when going from one fibre diameter to another. The determination of k_i parameters is of separate interest and can be done by studying the morphology of real porous structures. Obviously, k_1 is greater than 1, and k_2 should be chosen so that the fibre makes at least several bends inside the chosen cell. The values chosen for the calculation are: $k_1 = 5$ and $k_2 = 10$. Thus, the length m can be found:

$$m = rand[k_1 \cdot d\,, k_2 \cdot d\,]. \tag{17}$$

Correspondingly from (15) we find m_z:

$$m_z = rand[m \cdot \cos(\alpha_{max})\,,\ m\,]. \tag{18}$$

Knowing m_z the other components of the vector are calculated as follows:

$$m_x = rand[-\sqrt{m^2 - m_z^2},\ \sqrt{m^2 - m_z^2}\,], \tag{19}$$

$$m_y = \pm\sqrt{m^2 - m_z^2 - m_x^2}. \tag{20}$$

Accordingly, the coordinates of the point M_i are:

$$\begin{cases} M_{i,x} = M_{i-1,x} + m_x \\ M_{i,y} = M_{i-1,y} + m_y \\ M_{i,z} = M_{i-1,z} + m_z \end{cases}. \tag{21}$$

If the point M_i is outside the cube, the intersection point of the vector $\vec{m}$ and the cube face is taken instead. This approach should not distort the picture, since the number of fibres entering the control volume

from other volumes should be balanced on average by the number of fibres leaving the control volume. The resulting set of points allows plotting a non-uniform rational B-spline (NURBS) curve by means of the standard SpaceClaim functional. The fibre is obtained by pulling a circle of diameter d along the obtained curve. The length of the curve is subtracted from the full length L_f of the fibre and the script proceeds to build the next fibre and so on until $L_f > 0$. The view of individual fibres and the resulting structure is shown in Fig. 5.

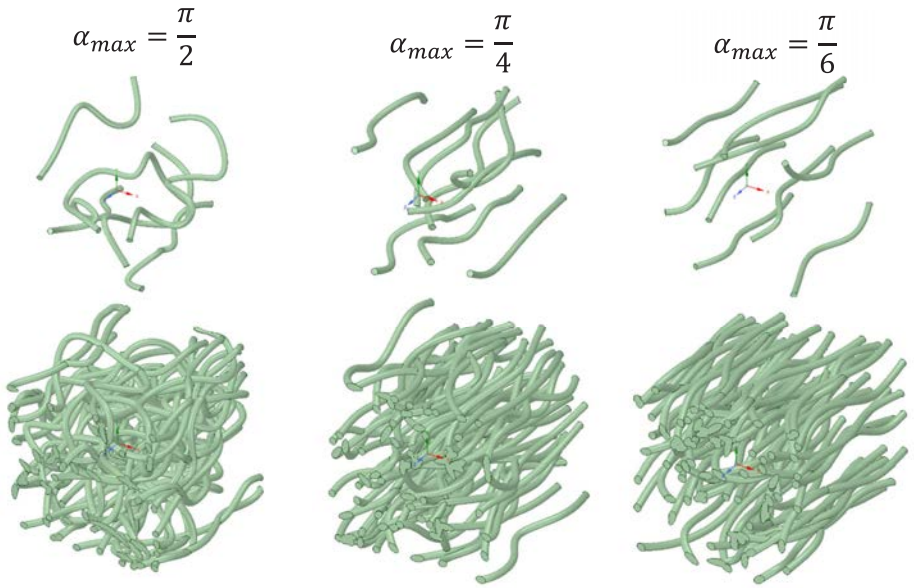

Fig. 5. Fibres and PB domains for $\alpha_{\max} \in \left\{\frac{\pi}{2}, \frac{\pi}{4}, \frac{\pi}{6}\right\}$ generated in SpaceClaim.

5. RESULTS AND DISCUSSION

The algorithm given in the previous paragraph allowed generating porous structures for different angles quickly. At the same time, the number of fibres in the control volume fluctuated around the average values within ± 1. For $\alpha_{max} = \frac{\pi}{2}$ there are 56 ± 1 fibres, for $\alpha_{max} = \frac{\pi}{4}$ - 75 ± 1 fibres and for $\alpha_{max} = \frac{\pi}{6}$ - 79 ± 1 fibres. This allows us to conclude that the selected volume should generally reflect the characteristics of the target PB (no needs to average over the ensemble). The geometry was exported to the ANSYS steady-state thermal solver. To simplify the setting of boundary conditions, two planes of dimensions LxL were added to the ends of the structures. Next, a tetrahedral mesh was constructed and the problem of finding the heat flow between the plates at given temperatures of their surfaces was solved using the FEA. From Fourier's law, the values of thermal conductivity of the porous structures were calculated. The theoretical value was calculated by formula (10) and λ_{max} by formula (6), assuming the thermal conductivity of copper was $\lambda_m = 394\ W/m \cdot K$. The calculation results are presented in Fig. 6.

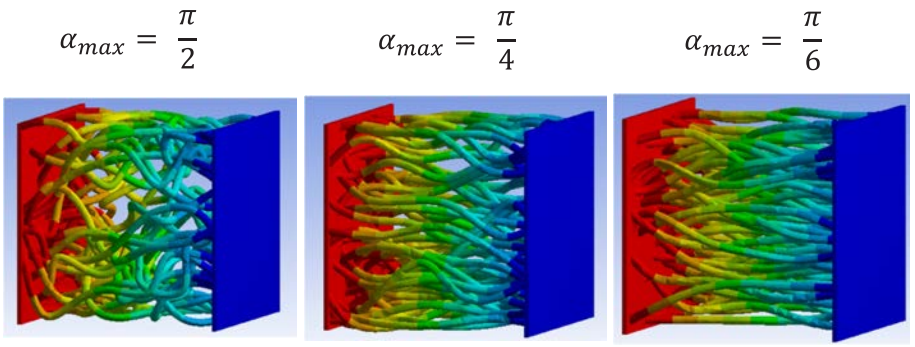

Fig. 6. Results comparison for $\alpha_{max} \in \left\{\frac{\pi}{2}, \frac{\pi}{4}, \frac{\pi}{6}\right\}$. Thermal conductivity of PB is calculated using theoretical relations and by FEA in ANSYS steady-state thermal solver.

As can be seen, the results agree with an accuracy of about 3 %.

6. CONCLUSIONS

The above rather simple analysis provides a practical guide to the development of a fabrication technique for the porous structure best suited for a TC. Using equations (6) and (11) for the thermal conductivity of a PB at a porosity of 80 %, we can get a value lying in the range: $39.4 \leq \bar{\lambda} \leq 78.8$. This is a very encouraging result, considering that for randomly oriented fibres the thermal conductivity is well described by the relation given in paper [7]:

$$\lambda = \frac{\lambda_m \cdot (1-\varphi)}{1+11 \cdot \varphi^2} = \frac{\lambda_{max}}{1+11 \cdot \varphi^2}, \tag{22}$$

which gives value to the thermal conductivity of just $9.8\ W/m \cdot K$ for the same porosity. In the previous stage of TC development, we obtained close results because we used structures with random fibre orientation. This significant gain in thermal conductivity suggests that the structure should be made of oriented fibres by developing an appropriate felting technology. Modelling of the porous structure has shown good agreement of the model with theoretical predictions, but its suitability for studying such parameters as transport characteristics of the PB requires further investigation. The model contains two arbitrary parameters k_1 and k_2 chosen intuitively. Their influence on the result and their correspondence to the characteristics of real materials require further study, including experimental validation.

ACKNOWLEDGEMENTS

The author would like to thank the Allatherm team, especially Dr. D. Mishkinis and Mr. L. Ivanovskis for fruitful cooperation in the development of the thermal compressor.

REFERENCES

1. Ušakovs, I., Mishkinis, D., Rohrbeck, M., Tijsterman, R., Bodendieck, F., & Aziz, S. (2022). Xenon refueling compressor: Engineering model development and testing. In *2nd International Conference on Flight Vehicles, Aerothermodynamics and Re-entry Missions & Engineering (FAR)*. 19–23 June 2022, Heilbronn, Germany.
2. Collishaw, P.G., & Evans, J.R.G., (1994). An Assessment of Expressions for the Apparent Thermal Conductivity of Cellular Materials. *Journal of Materials Science*, *29*, 486–498.
3. Mantle W.J., & Chang W.S., (1991). Effective Thermal Conductivity of Sintered Metal Fibres. *J. Thermophysics*, *5* (4).
4. Semena, M.G., & Zaripov, V.K. (1977). Influence of the Diameter and Length on Material Heat Transfer of Metal-Fibre Wicks of Heat Pipes. *Teploenergetika*, *24* (4), 82–84.
5. Veyhl, C., Fiedler, T., Andersen, O., Meinert, J., Bernthaler, T., Belova, I.V., & Murch, G.E. (2012). On the Thermal Conductivity of Sintered Metallic Fibre Structures. *International Journal of Heat and Mass Transfer, 55*, 2440–2448.
6. Belova, I.V., Graeme, E., Murch, G.E., Fiedler, T., & Öchsner, A. (2008). The Lattice Monte Carlo Method for Solving Phenomenological Mass and Thermal Diffusion Problems. *Defect and Diffusion Forum*, *279*, 13–22.
7. Koh, J.C.Y., & Fortini, A. (1973). Prediction of Thermal Conductivity and Electrical Resistivity of Porous Metallic Materials. *Int. J. Heat Mass Transfer.*, *16*, 1013–1022.

sciendo

LATVIAN JOURNAL OF PHYSICS
AND TECHNICAL SCIENCES
2023, N 6

DOI: 10.2478/lpts-2023-0049

INFLUENCE OF SURFACE WAVES ON LIQUID-TO-GAS MASS TRANSFER IN MOLTEN SILICON

G. Zageris*, V. Geza, S. Pavlovs

Institute of Numerical Modelling,
University of Latvia
3 Jelgavas Str., Riga, LV-1004, LATVIA
*e-mail: girts.zageris@lu.lv

The paper focuses on the numerical analysis of the mass transfer of impurities from the wavy surface of molten silicon to the gas phase. The mathematical model is described herein, with the modelling of a wavy silicon melt surface being done with the moving mesh technique. The model employs assumptions about the mass transfer process on the surface, namely, that it can be modelled with effective diffusion across the interface. The assumption is verified against limited experimental data for a stationary melt surface, and reasonable agreement is obtained. Thereafter, numerical studies are undertaken for a wavy melt surface. The dependence of impurity removal rate on the wave amplitude, wavelength and frequency is analysed. It is shown that the waves on the surface of the liquid increase the mass transfer rate in a certain parameter range. Finally, results are analysed to find an explanation for this increase and to determine technological factors that impact it. Surface enlargement due to waves and altered flow patterns near the silicon melt are determined as potential reasons for the improved impurity removal rate. A dimensionless criterion for the minimal wave amplitude required to obtain improved impurity removal is found and discussed.

Keywords*: Computational fluid dynamics, mass transfer, silicon refinement, surface waves.*

1. INTRODUCTION

The requirement for alternative energy sources, e.g., solar, wind, hydro, etc., is growing due to the exhaustion of fossil fuel resources, with growing energy consumption and global warming. One of the most attractive sources is solar power, which is divided in two types – direct conversion to electricity (photovoltaics – PV) and solar power concentration systems. PV systems are more popular because they can be used for applications of different scales. As shown in [1], the energy cost for solar power has rapidly fallen, but it is attributed mostly to PV module efficiency improvement, manufacturing optimisation and reduction in material intensity. However, the cost of raw silicon has seen an uptick since 2021, and PV cell costs are directly related to costs for raw materials, e.g., polysilicon. Reduction of energy consumption during production of polysilicon is one of the key steps towards solar power becoming more accessible.

In 2012, it was shown that production of polysilicon constituted approx. 14 % of the total solar cell costs [2]. This number can be reduced by lowering energy consumption during solar grade silicon (SoG-Si) production. Most silicon production starts with reduction of quartzite or sand with carbon materials [3]. Such a process can achieve a purity of up to 99 %. To achieve higher purity, there are two ways – the chemical and the metallurgical route. The metallurgical route consumes about 30 kWh/kgSi (kilowatt-hours per kilogram of silicon) of energy. In comparison, the chemical route such as the Siemens process, which is the most widely used refining process nowadays, consumes 65 kWh/kgSi [4].

In the metallurgical route for silicon production, directional solidification is used to remove metallic impurities. The most problematic elements are boron and phosphorus because their removal via the directional solidification method is limited due to their high segregation coefficients. In many investigations, phosphorus removal is found to be the most challenging task, since the purity threshold (<1 ppm) was not reached [5]. Although oxidation and slag refinement is a simple process for removing phosphorus from silicon, it is insufficient to reach the high purity threshold. The most popular approach for phosphorus removal is evacuation. In [6], it was shown that the rate for phosphorus evaporation corresponded to a first order reaction and that under medium vacuum conditions the evaporation rate was determined by chemical evaporation at the surface and gas phase mass transfer.

For boron removal, a well-known approach is blowing oxidizing gas on the free surface of the melt [7]. The highest boron refining rates can be achieved with plasma refining, but it has a high energy demand. In reactive gas refining, the concentration of boron changes according to a first order rate law:

$$\ln\left(\frac{C_{\mathrm{B},0}}{C_{\mathrm{B},t}}\right) = k_{\mathrm{B}}\frac{St}{V}, \tag{1}$$

where C_{B} is the boron concentration with indices after comma indicating time, S is the area of interfacial surface between oxidizing gas and silicon melt, V is the volume of silicon melt, t is time, k_{B} is the boron mass transfer coefficient at the surface, measured in μm/s (note that k_{B} does not denote Boltzmann's constant within this paper). In fact, the reaction occurring at the interface is of second order; however, the concentration of the reacting gas is kept constant by continuously supplying gas to

the surface. Thus, the law describing reaction rate becomes first order effectively. k_B is determined experimentally and is dependent on the oxidizing gas supply rate, the type of oxidizing gas, and melt temperature. Typical k_B values found in literature are 6–40 μm/s [7]–[9], and the value for k_P is 2–5 μm/s for phosphorus [6]. The typical melt temperature is ≈1425 C.

The creation of surface waves would, in principle, increase the S/V ratio, thus speeding up boron removal. Though under normal operating conditions no waves are generated during the purification process, it has been shown that waves on liquid metal surfaces can be generated, for example, by contactless electromagnetic interaction in mercury both experimentally [10] and theoretically [11]. Estimating the surface enlargement from [10] according to Eq. (16) (see Section 3.3.) with crucible radius $R_0 = 0.09$ m, wave amplitude $A = 0.001$ m and wavenumber $n = 10$, the potential increase in the free surface is approximately 10 %. Therefore, it would potentially be of interest to create waves during purification to increase process efficiency.

2. MODEL DESIGN AND BOUNDARY CONDITIONS

2.1. Problem Description

The physical system considered in this study is that of a cylindrical tank, which contains molten silicon. The oxidizing gas is introduced via a centrally located cylindrical pipe directly above the melt. The impurities located inside the melt can then evacuate from it via the melt-gas interface and escape the tank together with the gas flow. Then surface waves are introduced on the silicon melt to study the impact of these waves on the overall purification efficiency.

In cases where this study focuses on the diffusion of the impurities on a larger time scale, the entire system (melt + gas) is modelled with a stationary interface. However, when the effects of a wavy surface are studied, only the gas domain is modelled. In this case, the silicon melt is only taken into account in the form of a boundary with a certain harmonic profile and a constant impurity concentration.

To reduce the need for substantial computational resources, the problems are modelled with 2D axi-symmetric geometries.

In this study, the gas blowing above the melt is assumed to have the same viscosity as dry air $\nu = 1.51110^{-5}$ m^2/s [12].

In the simulation where only the bulk gas is considered, calculations are done for a 2D axisymmetric geometry. In Fig. 1, the geometry and a representative picture of the computational mesh are given. In Fig. 1a the sketch of the geometry is shown. The mesh grid used for calculations is illustrated in Fig. 1b and 1c. As can be seen, the grid is more refined where deformations of the mesh take place, both to better absorb the mesh deformations and to resolve the diffusion boundary layer.

The computational mesh was created using an open-source program SALOME. The number of elements in the mesh is 15000. To arrive at this number, a mesh independence study was performed. An initial coarse mesh was progressively made finer and finer until no significant difference in the simulation results could be observed. The results obtained with the mesh used in this study differed no more than 1% from the previous calculation, which was

deemed precise enough in the scope of this research. A mesh twice as fine (i.e., face size of each element is two times smaller) gave no appreciable improvement to the results as compared to the mesh used in the study (deviations were less than 1 %).

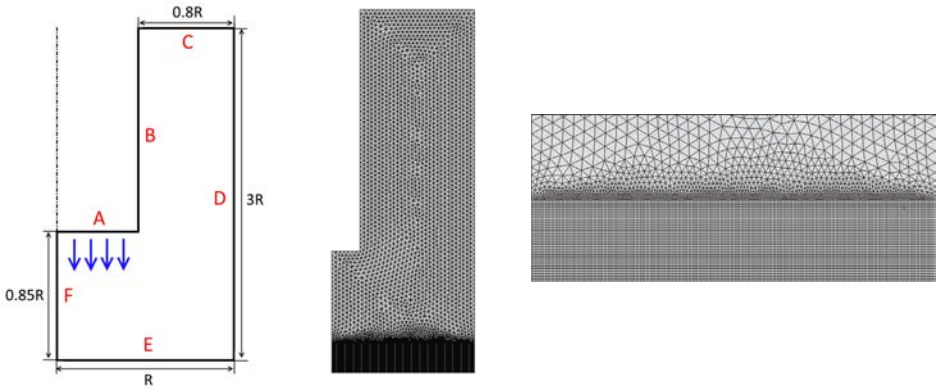

a) Sketch of the geometry, R = 1 m

b) The mesh in the entire domain

c) Zoomed mesh near the surface of the silicon melt

Fig. 1. Problem geometry and computational mesh.

2.2. Model Equations

To describe this problem, one needs to define the fluids in motion. The motion of an incompressible fluid is governed by the Navier-Stokes equations (Eq. (2)). The additional information necessary to describe fluid flow is the conservation of mass (Eq. (3)), expressed by the equation of continuity:

$$\frac{\partial \boldsymbol{u}^*}{\partial t^*} + (\boldsymbol{u}^* \cdot \nabla)\boldsymbol{u}^* = -\nabla p^* + \frac{1}{Re}\nabla^2 \boldsymbol{u}^*, \quad (2)$$

$$\nabla \cdot \boldsymbol{u}^* = 0, \quad (3)$$

$$Re = \frac{UL}{\nu}. \quad (4)$$

The species transfer equation is written in the form of

$$\frac{\partial C}{\partial t^*} + \boldsymbol{u}^* \cdot \nabla C = \widetilde{D}\nabla^2 C, \quad (5)$$

$$\widetilde{D} = \frac{1}{UL}\left(D + \frac{\mu_t}{Sc_t}\right). \quad (6)$$

Turbulence and turbulent viscosity are modelled with the standard k-ε model.

These equations implicitly take into account the following assumptions:

- The fluid is incompressible;
- The fluids in consideration are Newtonian;
- The molecular diffusion coefficient of the impurities D is independent of spatial coordinates;
- The effective diffusion coefficient $\widetilde{D}$ is composed of molecular diffusion D and turbulent diffusion terms.

Notably, heat transfer has been omitted from the model equations, effectively solving the flow in isothermal conditions. This is a reasonable simplification because the technological process demands that the flow must be dominated by forced convection from the gas blowing, thus allowing for buoyancy to be neglected.

To numerically investigate the role of surface waves on impurity removal from silicon, the open-source toolbox *OpenFOAM* is used. The main algorithm for calculating the flow and impurity transport is *pimple-*

DyMScalarFoam, which is derived from the default *OpenFOAM* algorithm *pimpleDyMFoam*, which calculates fluid flow for a dynamic mesh by deploying the PIMPLE algorithm. However, *pimpleDyMFoam* does not contain any other scalar diffusive transport equations, so a concentration diffusion term has been added to the algorithm, renaming it to *pimpleDyMScalarFoam* (the name contains *Scalar*, but it can simulate both thermal and diffusion processes due to the equations being identical).

pimpleDyMScalarFoam solves fluid flow and concentration diffusion separately – first, it recalculates fluid velocity relatively to the moving mesh, then it solves a full PIMPLE cycle (ignoring concentration diffusion), and, finally, calculates one step for diffusion with the newly obtained fluid variables. Therefore, the fluid impacts how concentration diffusion happens but not vice versa. It is thus implicitly stated that the gas above the molten silicon is dilute with respect to the concentration of silicon impurities. The algorithm repeats additional iterations until a residual of 10^{-6} is obtained. In this study, the PIMPLE algorithm runs with two outer corrector loops, one inner corrector loop and one non-orthogonal corrector loop. The time domain is discretized with the Euler scheme, divergence terms are discretized with the Gauss upwind scheme and the Laplacian terms are approximated with Gauss linear corrected schemes.

Boundary conditions must also be set for the problem. The boundary conditions are summarised in Table 1. It is important to note that the chosen boundary condition for the value of impurity concentration on the surface of the molten silicon being constant c=1 is a simplification that neglects the role of transient chemical reactions and impurity transport within the molten silicon itself. However, within the scope of this research it is an acceptable simplification (see Subsection 2.3). Inlet values for k and ε were chosen to keep turbulence low at the inlet in order to allow for the system geometry, wave interaction and impurity diffusion at the interface to dominate the effects on all physical processes.

In most cases, *OpenFOAM* has keywords for standard boundary conditions. However, in this case, a custom boundary condition was necessary for the deformation of the boundary corresponding to the surface of molten silicon. To do this, a new boundary condition *SineVelocity* was defined, which moves the boundary points according to the law $u_y = A\sin\left(\frac{2\pi x}{\lambda}\right)\sin\left(\frac{2\pi t}{T}\right)$. The free parameters here are amplitude A, wavelength λ and period T. The value of L, which corresponds to the length of the moving boundary, is determined automatically. Despite the parameters λ and T being free to choose from an implementation standpoint, the dispersion relation for gravity waves is nevertheless used as an approximation for the relation between variables λ and T. Generally, the dispersion relation for gravity waves is:

$$\omega^2 = gk_\lambda + \frac{\sigma k_\lambda^3}{\rho}. \tag{7}$$

However, with the characteristic values of g=10 m/s^2, λ=5 mm, σ=0.7 N/m [13] and ρ=2550 kg/m^3 [14] for molten silicon, the ratio between the first term and second term in Eq. (7) is approximately 140, thus allowing one to use only the first term in the dispersion relation. This permits rewriting the dispersion relation for variables λ and T:

$$\frac{\lambda}{T} = \sqrt{\frac{g\lambda}{2\pi}}. \tag{8}$$

Once calculations are complete, the concentration flow field is integrated on the outflow boundary at every time step to obtain the total amount of impurity concentration that has left the domain:

$$\Phi_C = \int C v_n \, dS. \quad (10)$$

The value of Φ_C serves as the main comparative quantity between different calculations if inlet velocity remains fixed.

Note also that for turbulence parameters and wall functions are used despite the fact that mesh resolution strongly varies in different places in the mesh. This is not an issue because *OpenFOAM* automatically implements the correct approach (linear vs. log) in a stepwise manner according to the mesh resolution at a certain point near the wall.

Table 1. Summary of Boundary Conditions in the Simulation. WF – Wall Function, SYMM – Symmetry

Boundary	Inlet	Inner wall	Outlet	Outer wall	Si surface	Axis
Label (Fig 1)	A	B	C	D	E	F
Quantity						
$\boldsymbol{u}^*$	$\boldsymbol{u}_n^* = 0.7$ m/s	$\boldsymbol{u}^* = 0$	$\frac{\partial \boldsymbol{u}^*}{\partial \boldsymbol{n}} = 0$	$\boldsymbol{u}^* = 0$	$\boldsymbol{u}^* = 0$	SYMM
p	$\frac{\partial p}{\partial \boldsymbol{n}} = 0$	$\frac{\partial p}{\partial \boldsymbol{n}} = 0$	$p = 0$	$\frac{\partial p}{\partial \boldsymbol{n}} = 0$	$\frac{\partial p}{\partial \boldsymbol{n}} = 0$	SYMM
c	$c = 0$	$\frac{\partial c}{\partial \boldsymbol{n}} = 0$	$\frac{\partial c}{\partial \boldsymbol{n}} = 0$	$\frac{\partial c}{\partial \boldsymbol{n}} = 0$	$c = 1$	SYMM
ε	$\varepsilon = 10^{-6}$ m^2/s^3	WF	$\frac{\partial \varepsilon}{\partial \boldsymbol{n}} = 0$	WF	WF	SYMM
k	$k = 10^{-5}$ m^2/s^2	WF	$\frac{\partial k}{\partial \boldsymbol{n}} = 0$	WF	WF	SYMM
Motion	$\boldsymbol{v} = 0$	$\boldsymbol{v} = 0$	$\boldsymbol{v} = 0$	$\frac{\partial \boldsymbol{v}}{\partial \boldsymbol{\tau}} = 0$	*SineVelocity*	$\frac{\partial \boldsymbol{v}}{\partial \boldsymbol{\tau}} = 0$

2.3. Neglecting Chemical Reactions

The reaction scheme for partial boron oxidation with the oxidizing gas is described in [7]:

$$\mathrm{Si} + \mathrm{H_2O} = \mathrm{SiO} + \mathrm{H_2}, \quad (11)$$

$$\mathrm{B} + \mathrm{H_2O} = \mathrm{HBO} + \frac{1}{2}\mathrm{H_2}, \quad (12)$$

$$\mathrm{B} + \mathrm{SiO} + \frac{1}{2}\mathrm{H_2} = \mathrm{HBO} + \mathrm{Si}. \quad (13)$$

For this research, reactions at the interface were neglected. Instead, constant concentration of HBO was assumed at the silicon surface. This was done for several reasons. First, Sortland [7] argues that resistance for HBO transport stemming particularly from the reactions at the interface is very small and their influence on boron removal rate is negligible.

Second, the supply of H_2O to the surface depends on the concentration of H_2O in the gas and the resistance of diffusion layer:

$$J_{\mathrm{H_2O}} = k_{\mathrm{diff}}^{\mathrm{H_2O}} \left(C_{\mathrm{H_2O}}^{\mathrm{gas}} - C_{\mathrm{H_2O}}^{\mathrm{int}} \right), \quad (14)$$

where $k_{\mathrm{diff}}^{\mathrm{H_2O}}$ is the mass transfer coefficient of the H_2O from the gas to the interface, $C_{\mathrm{H_2O}}^{\mathrm{int}}$, $C_{\mathrm{H_2O}}^{\mathrm{gas}}$, – concentration of H_2O in the gas and at the interface respectively. Here only $k_{\mathrm{diff}}^{\mathrm{H_2O}}$ can vary spatially due to a different thickness of the diffusion layer along the silicon-gas interface.

The same principle can be applied to the diffusion of from the interface to the gas. Assuming good mixing in the silicon and slowly changing concentrations of B (char-

acteristic time is several hours), C_B can be assumed to be constant along the surface; hence, $C_{\mathrm{HBO}}^{\mathrm{int}}$ is also constant.

$$J_{\mathrm{HBO}} = k_{\mathrm{diff}}^{\mathrm{HBO}}\left(C_{\mathrm{HBO}}^{\mathrm{int}} - C_{\mathrm{HBO}}^{\mathrm{gas}}\right). \quad (15)$$

Taking into account those considerations, it is possible to simplify the model to a purely diffusion dominated impurity flux from the silicon to the gas in the boundary layer. The boron removal rate depends also on the amount of water vapor in the reactive gas, but this is not taken into account here.

2.4. Submodel for Stationary Melt Surface

A variant of the model described above that also includes the molten silicon in the crucible was implemented in ANSYS *Fluent* to, first, verify the assumption that mass transfer of impurities from the melt could be approximated by effective diffusion, and, second, to study whether impurity removal rate could be improved solely by manipulating the gas flow above the melt. The model and its results are described more in detail in [15], but key elements are outlined here as well. Afterwards, the main model in *OpenFOAM* was verified against the submodel implemented in *Fluent* to obtain at least some verification of the main model.

In this separate study, a 2D axi-symmetrical crucible of radius $R_0 = 0.0031$ and centrally located inlet radius $r_0 = 0.0031$ was considered. The height of the crucible was $H = 0.186$ m and was filled up to half height with molten silicon. The top half of the crucible is filled with (initially clean) argon gas. Additionally, there is an inductor placed around the molten silicon that facilitates melt mixing. The current in the inductor was $I = 10$ kA with frequency $f = 50$ Hz, the inductor had 10 turns and a total height $h = 0.082$ m. The material constants were silicon density $\rho_{\mathrm{Si}} = 2550$ kg/m^3 [14], silicon viscosity $\mu_{\mathrm{Si}} = 9.78 \cdot 10^{-4}$ Pa·s [16], argon density $\rho_{\mathrm{Ar}} = 1.511$ kg/m^3, argon viscosity $\mu_{\mathrm{Ar}} = 7.44 \cdot 10^{-5}$ Pa·s [17]. The argon gas introduced through the top inlet was flowing in at a velocity of $v_0 = 2.21$ m/s. The temperature of the crucible was $T = 1500$ °C. Other boundary conditions are consistent with Table 1, except that in this model the interface between the melt and gas is no longer a geometric boundary. Instead, the silicon melt has an initial impurity concentration $c = 1$, which can diffuse to the gas phase according to Fick's law with a uniform diffusion constant $D_0 = 3.4 \cdot 10^{-4}$ m^2/s. This corresponds to the diffusion coefficient for HBO gas [18]. A schematic representation of the model can be seen in Fig. 2a.

3. RESULTS AND DISCUSSION

3.1. Verification of Effective Diffusion Assumption

The submodel described in Section 2.4. was run in *ANSYS Fluent*. An exponential decay was obtained for the average concentration in the silicon melt with a characteristic time of τ=1.36 (see Fig. 2b). This allows for the estimation of the coefficient according to Eq. (1), which gives the value k_{B}=1.9·10^{-5} m/s. This value is both in agreement with the range described in Section 1 and with literature where experimental data are available for similar cases with silicon melt stirring [7], [19]. This agreement with other works appears to justify the assumptions made previously in this paper.

However, later on, a moving silicon melt surface will be considered, and this will be

modelled with the algorithm *pimpleDyMScalarFoam* outlined in Section 2.2. To verify this algorithm, identical cases were studied with the *pimpleDyMScalarFoam* algorithm in *OpenFOAM 4.1* and in *ANSYS Fluent 18*. The case was set up according to Table 1 with a stationary melt surface and the same computational mesh was deployed in both programs. Upon comparing the results, the flow velocity fields and concentration fields matched, with differences of no greater than 3 % across the domain for all physical quantities and for the concentration flux at the outflow. Because the mesh independence study showed a dependence on the mesh no greater that 1 %, then the error of all results for concentration outflow is assumed to be 3 % of the flux value. This is how error bars are calculated later in the paper. This slight disagreement between *ANSYS Fluent* and *pimpleDyMScalarFoam* is most likely due to slightly different implementations of wall functions and numerical schemes.

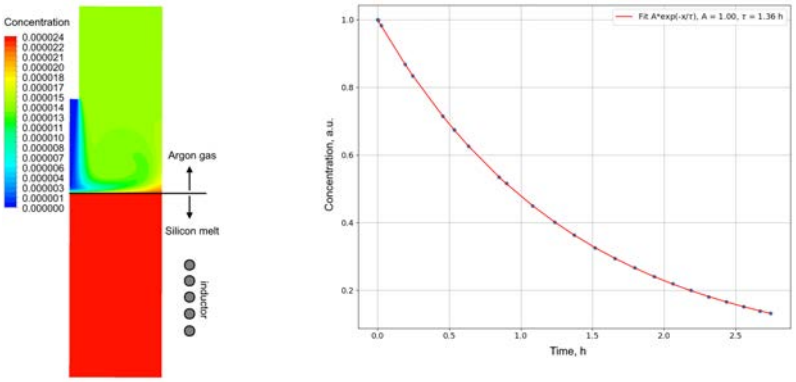

a) Schematic sketch of the verification case

b) Average concentration in the silicon melt over time in the verification case

Fig. 2. Verification case setup and data of impurity concentration over time.

3.2. Simulations for Steady Surface with the Fluent Submodel

Because it was not clear whether the gas velocity and thus also the turbulence and the thickness of the boundary layer are the main parameters responsible for the removal of boron, an assumption was made that it was the uniform distribution of the incoming (clean) oxidizing gas across the surface which could enhance the purification rate. For this reason, simulations with a steady (flat) free surface were done for a different number of lances of the incoming gas jet (see [15]). More jets may lead to a more uniform distribution of the incoming gas and the normal gradient of concentration would be equal across the free surface.

Quasi-stationary gas and silicon flow patterns and boron concentration distribution are shown in Fig. 3. Similar distributions are also obtained with a 3D model (see [15]). The time scale in plots is scaled according to $t^* = D/d^2 t$, where D – diffusion coefficient of HBO in gas, d – crucible diameter. Thus, time scale $t^* = 1$ corresponds to the diffusion time scale.

The computed integral boron concentration in silicon during long-time refinement process is shown in Fig. 4 – dotted and solid lines for 2D and axi-symmetrical 3D models with a single lance (n = 1), accordingly. The estimated dimensionless boron mass

transfer coefficient value $k_{\mathrm{B}}^{*} = k_b \cdot \frac{d}{D}$ based on simulation of refinement is $k_{\mathrm{B}}^{*} = 36.27$ for 2D model; for the axi-symmetrical 3D model the estimated value is by 10 % greater – $k_B^{*} = 39.94$ (see Fig. 4).

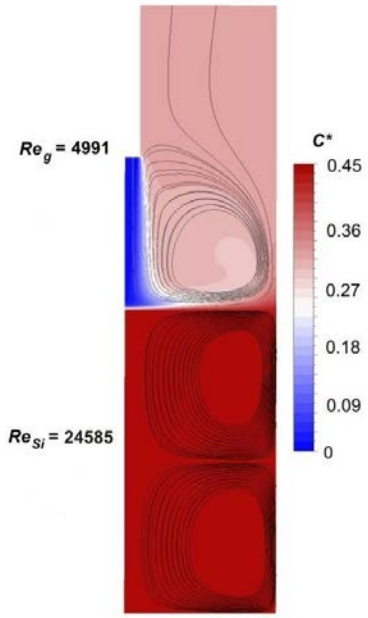

Fig. 3. 2D scheme of boron removal from silicon with gas jet: Re_{Si} and Re_g – silicon and gas Reynolds numbers and C^* – boron concentration contours, where $C^* = \frac{C_{B,t}}{C_{B,0}}$ and $C_{B,0} = 10^{-5} =$, obtained with 2D model for flow time $t^* = 0.022$.

The computations are performed for different numbers of lances n = 1, 2, 3, 4, 5, 13. The total flow rate of all gas jets is constant and equal to the flow rate of the gas jet for the model with a single lance. The coefficient k_B^{*} as a function of the number of lances n is shown in Fig. 5 (blue scale and triangles). The obtained results show that the largest value of k_B^{*} corresponds to a single lance system. A possible explanation is connected with the analysis of gas flow patterns in the vicinity of gas–silicon interface:

- The gas flow rate in each single jet for a multiple lance system is lower; hence, the turbulence is lower;
- Gas jets decelerate each other;
- The inertia of the incoming jet is lower and, thus, less gas reaches the surface, and the diffusion boundary layer is larger in case of multiple jets.

A very important issue here is the size of the diffusion boundary layer. This is essential in a real process where chemical reactions take place. As already noted, this is modelled instead via effective diffusion. A simple way of viewing the influence of the boundary layer is following the path of a single oxygen molecule. Oxygen with a water molecule diffuses through the boundary layer with a mass transfer coefficient $k_{diff}^{H_2O}$, then water reacts with boron (reaction Eq. (12)), and HBO is removed from the system, first through boundary layer with k_{diff}^{HBO}, and then with gas in bulk flow. For boron removal, two diffusion processes must follow each other.

Figure 5 also shows the dependence of the mass transfer coefficient on the height of the lance (distance from the silicon surface). It is visible that there is a slight enhancement of mass transfer if the lance is moved closer to the surface – an increase of by moving the lance from the distance $h^* = h/d = 0.75$ to $h^* = 0.05$.

Simulations with slanted lances were also performed; however, the coefficient k_{B}^{*} decreased by 30 % when the angle of the slope α_{lance} increased by 45° as measured from the vertical line.

This suggests that it is not possible to improve the purification rate by manipulating only the gas flow – different numbers of lances and/or diameters of lances and/or sloping angles of the lances do not give any improvement when the total mass flow rate of the gas is kept constant and the lance height is kept constant as well.

Therefore, to obtain any improvement, an investigation on the wavy melt surface is required.

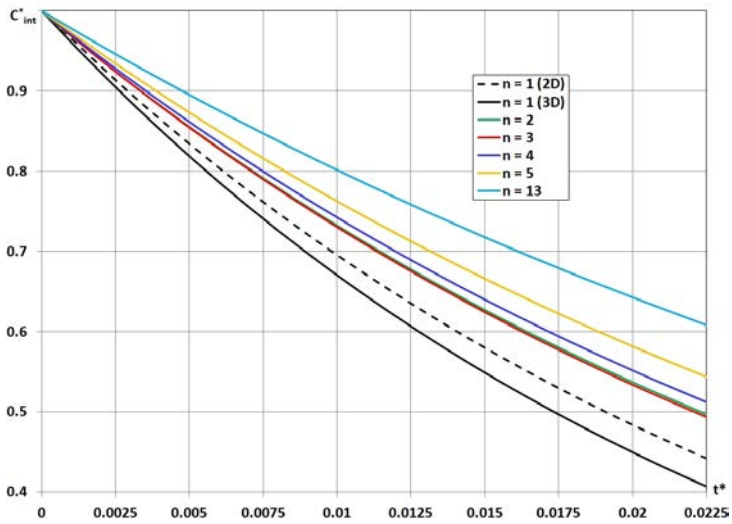

Fig. 4. Boron integral concentration C^*_{int} (where $C^*_{int} = \frac{C^{int}_{B,t}}{C^{int}_{B,0}}$) in silicon melt as a function of silicon refining process time t^* for different numbers (n) of vertical ($\alpha_{lance} = 0°$) gas lances.

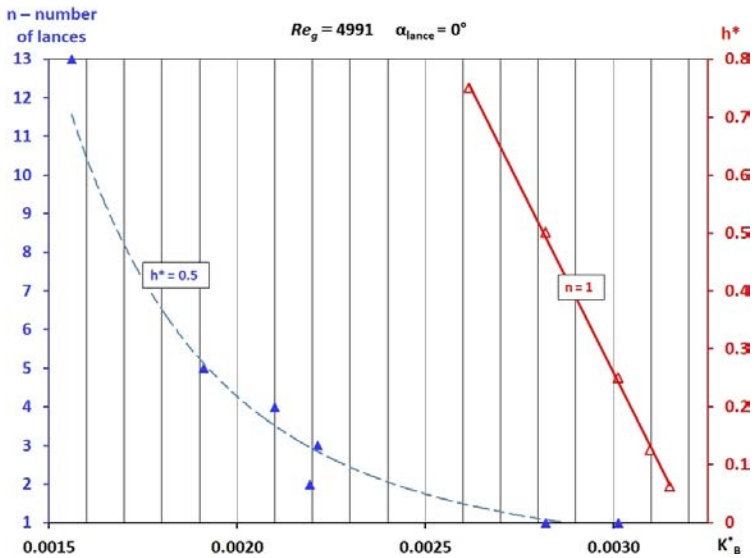

Fig. 5. Boron mass transfer coefficient k^*_B at the gas-silicon interface for vertical ($\alpha_{lance} = 0°$) gas lances: (red scale and triangles) k^*_B as a function of gas lance height lance-to-melt with a linear trend line (solid) (blue scale and triangles) k^*_B as a function of the number of lances n for $h^* = 0.5$ with power trend line (dotted).

3.3. Wave Parameter Impact on HBO Diffusion

From here on out, the wavy silicon surface is considered. To study the impact of molten silicon surface waves on impurity diffusion away from the silicon, numerical calculations were performed with the main model in *OpenFOAM*. The criterion

for the quality of impurity diffusion is the concentration flow which flows out of the computational domain Φ_C. Surface wave amplitude, frequency and wavelength are chosen as independent parameters to study the impact on impurity removal. The role of the impurity diffusion coefficient D on the factors determining impurity evacuation rate will be discussed later in Section 3.5.

In our calculations, no case went above a dimensionless wave amplitude of $A/\lambda > 0.2$. This is because waves larger than that approach the limit at which they would be expected to deform and crash. Furthermore, the obtained data were also normalized by the enlargement of the surface area due to waves to determine whether the improvement in impurity removal was solely due to the surface area enlargement. Since the surface waves are assumed to be harmonic in the scope of this research, one can analytically calculate the surface area of the wavy surface with basic calculus. To obtain the surface area enlargement, one must then divide the enlarged surface by the original surface of the stationary melt. Thus, the average surface area enlargement q over time can be calculated numerically by using:

$$q = \frac{1}{R_0}\int_0^{R_0} \sqrt{1 + \frac{1}{2}\left(\frac{\pi n A}{R_0}\cos\frac{\pi n x}{R_0}\right)}\, dx\,, \quad (16)$$

where l is the crucible radius and n is the wavenumber of the surface waves.

3.3.1. Effect of Frequency

First of all, the effect of wave oscillation frequency on impurity diffusion was studied. It is important to note that in this part of the study, frequency was considered independent of wavelength (that is, only the wave oscillation was changed while the wavelength was kept constant $\lambda = 0.25$ m). Later in the study, the dispersion relation was taken in account to model the relationship between frequency and wavelength. As can be seen in Fig. 6, no change was observed – the mean value of the total impurity concentration flow away from the computational domain was unchanged. Changes could be observed only in small time scale oscillations (at the same order of magnitude as the wave oscillations themselves) which did not affect long-term processes (such as the overall purification of the molten silicon). The frequencies studied were around the base frequency f_0 for the chosen base wavelength $\lambda = 0.25\,m$. According to Eq. (8), $f_0 = 2.52$ Hz. The error bars for Fig. 6 (and further figures from here on out) are calculated as described in Section 3.1.

3.3.2. Effect of Amplitude

A series of calculations with fixed wavelength and variable wave amplitudes was computed. In Fig. 7, a clear upward trend with increasing wave amplitude above the error threshold for the impurity concentration outflow can be observed. Furthermore, the normalized data almost agree with the stationary surface effective diffusion rate.

3.3.3. Effect of Wavelength

Next, a series of calculations with fixed amplitude and variable wavelengths was computed. In Fig. 8, an upward trend beyond the error threshold is also observable. The data were once again normalized to surface area enlargement. In this case, despite hav-

ing approximately the same dimensionless amplitudes, the observed concentration outflow values differ significantly.

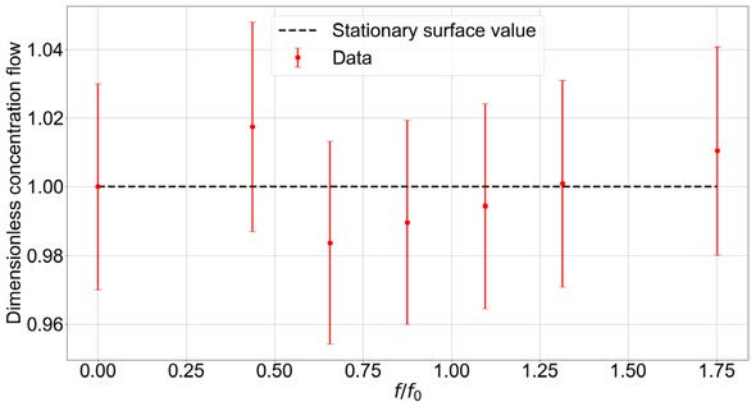

Fig. 6. HBO concentration outflow as a function frequency, $f_0 = 2.52$ Hz.

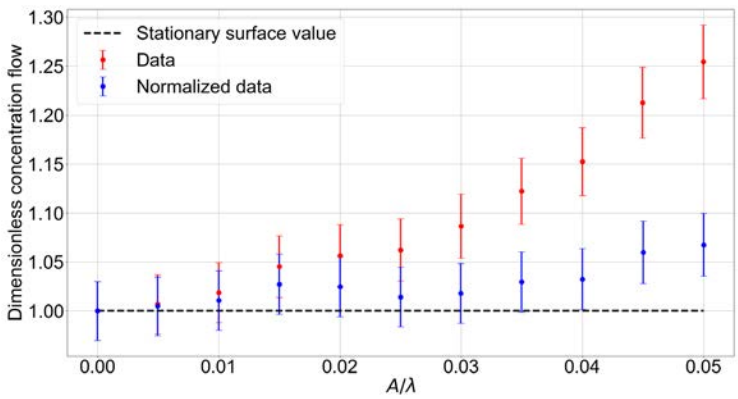

Fig. 7. HBO concentration outflow as a function of dimensionless wave amplitude for variable amplitudes. Amplitude is normalized to $\lambda = 0.25$ m.

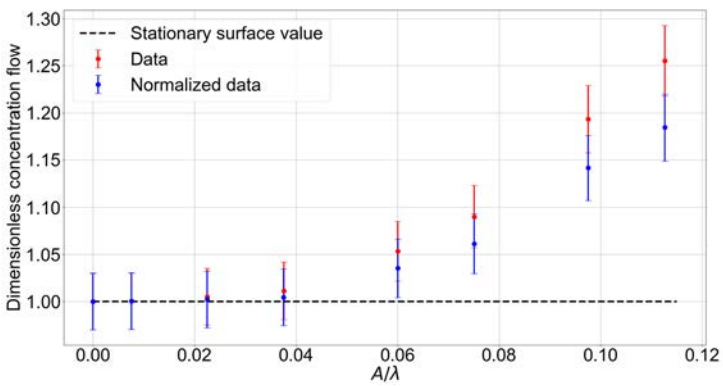

Fig. 8. HBO concentration outflow as a function of dimensionless wave amplitude for variable wavelength. The amplitude is constant $A = 0.015$ m.

3.4. Factor Analysis

In both cases of variable amplitude and variable wavelength, an improvement for integral concentration outflow is observed. There are multiple factors that could contribute to this.

To begin, there is the surface area enlargement due to waves. As impurity diffusion occurs via the surface, a larger surface area would also mean increased diffusion. In the variable amplitude case, this would almost suffice as an explanation – as can be seen in Fig. 7, the normalized data agree with the original stationary surface diffusion rate within a margin of error (except for the final two points). However, this does not explain the data obtained with variable wavelength. Here, the normalized data do not agree with the stationary diffusion rate. Therefore, some other mechanism must be in play.

As [20] has shown, thermal diffusion for inclined plates (with respect to the incoming flow direction) increases with an angle of attack. The flow above the surface waves is practically horizontal (consider Fig. 10), so the flow regime is not unlike the one studied by [20]. Therefore, the angle of the surface wave crests with respect to the incoming flow plays a role in the improvement of the diffusion rate. As the value of A/λ increases, so does the maximum angle of the wave, thus improving diffusion. This, for example, could contribute to the disparity for the final two points for the normalized data in Fig. 7.

Furthermore, it can also be shown that waves with a larger dimensionless wave amplitude generate greater turbulence in the vicinity of those waves. To support this, additional supportive calculations were performed in ANSYS Fluent, in which the flow close to the waves was studied. In Fig. 9, eddy viscosity μ_T near the waves is larger for the case when the amplitude is also greater. This has a direct impact for impurity diffusion as well – turbulent diffusion is far greater than molecular diffusion ($D_T/D_0 >> 1$); thus, eddy viscosity is a deciding factor for the rate of diffusion at a certain point in the flow. For larger wave amplitudes, turbulence near waves is also greater, facilitating better impurity removal from the area immediately next to the waves. This is in accord with a similar study done in [21], where an analogous problem is studied for heat diffusion in wavy channels.

Finally, the flow characteristics above surface waves must also be considered. All of the factors considered thus far affect diffusion uniformly across the whole surface. However, the flow above the waves introduce a certain asymmetry. In Fig. 10, the flow velocity vectors show that the flow both near the axis of the geometry (leftmost side) and next to the wall (rightmost side) is stagnant. In these stagnant points, particularly near the wall, a stable concentration gradient can form, as opposed to the waves in the middle, where no stable gradient can form. Because of this, diffusion is more intense where the flow is closer to the waves, and less intense in the stagnant points. Therefore, all the previously discussed effects also have a more pronounced effect for waves in the middle and less so for the waves near the edges of the geometry.

This effect allows for illustration of the tendency seen in Fig. 8. Even though values for A/λ were the same for both the cases of variable amplitude and variable wavelength, the integral concentration outflow differs significantly. This means that changing amplitude at a fixed wavelength and changing wavelength at a fixed amplitude

is not the same in terms of effect produced, even if it is in terms of dimensionless amplitude. This may be explained by the effect just discussed – when the wavelength is shortened, more waves appear in the active diffusion zone, allowing for all the previous mechanisms to have a more pronounced effect, leading to an increase in concentration outflow.

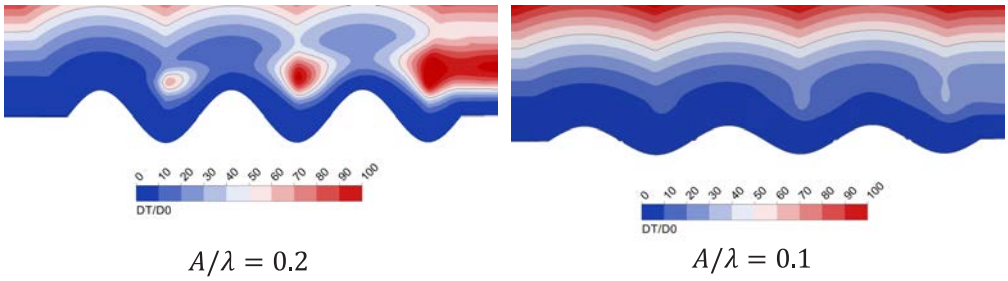

Fig. 9. Eddy viscosity near waves for different wave heights.

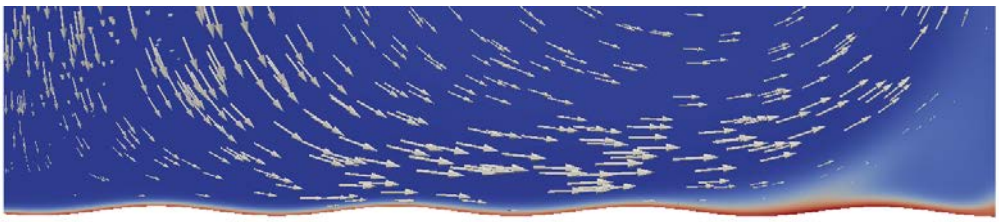

Fig. 10. Flow regime directly above the surface waves. Vectors denote velocity, background coloring denotes concentration of HBO.

3.4.1. Role of Molecular Diffusion

Up to this point, the role of molecular diffusion of HBO has not been analysed. Namely, the Peclet number in all cases considered up to this point was nearly the same. A separate study has been done to determine how the Peclet number impacts the results so far discussed. In this study, five otherwise identical cases were simulated with different values of Pe. To calculate Pe, one must choose a characteristic length and velocity. Because the silicon-gas interface is of interest, the characteristic length is chosen equal to wave amplitude and the characteristic velocity is chosen as the gas velocity directly above the interface. To better understand the factors impacting impurity removal, this study also considers the impact of different Pe numbers near the melt-gas interface.

To determine this, simulations exactly like described in Subsection 3.3.3 were run again, but with modified molecular diffusion coefficients for the impurities in order to obtain different Pe numbers. It was found that for certain values of Pe, the surface waves had no impact whatsoever on the concentration outflow – it remained the same for all combinations of dimensionless amplitudes and never showed a value larger than for the stationary surface without waves. However, for larger Pe, the characteristic impact discussed previously reap-

peared (see Fig. 12).

The different values of Pe dictate the extent to which impurities can diffuse into the gas phase at a given time. It was empirically determined that if the molecular diffusion length was large with respect to the amplitude of the waves, the waves could no longer impact the diffusion of HBO (see Fig. 12). Clearly, if the impurities quickly diffuse into the gas, then wave phenomena below this characteristic diffusion length have a diminishing impact. A side-by-side comparison of two cases with different values of Pe can be seen in Fig. 11.

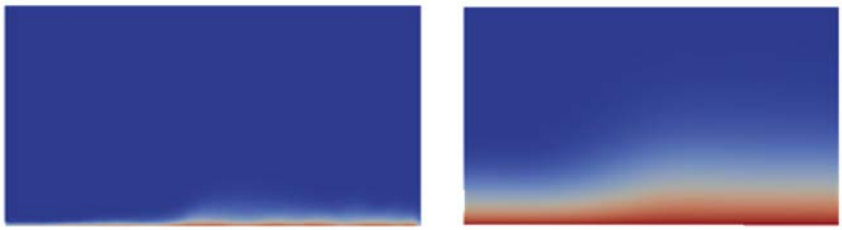

a) $Pe = 127$ b) $Pe = 0.32$

Fig. 11. Diffusion length at time *t* when the gas hits the melt surface for (a) a large value of Pe (b) a small value of Pe.

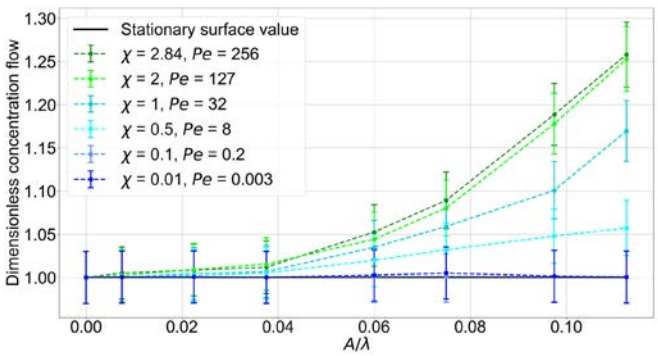

Fig. 12. HBO concentration outflow as a function of dimensionless wave amplitude for a variable amplitude at different values of χ, $A = 0.015$ m.

It is hypothesized that a dimensionless parameter that relates the molecular diffusion length to the amplitude of the waves is important for forecasting whether surface waves will have any impact on the overall diffusion of HBO impurities to the gaseous phase. It is defined in the following way:

$$\chi = \frac{A}{2\sqrt{(D_0 T)}}, \tag{17}$$

where A is the surface wave amplitude and T is the period of oscillation for these waves.

It has been observed that χ should be at least larger than unity for surface waves to have an effect on the impurity diffusion at the surface (see Fig. 12). This dimensionless number relates the wave amplitude with the characteristic diffusion length over one oscillation period. The reasoning behind choosing such a definition for this number is that the "period" of diffusion is also the wave period – that is to say that the global gas flow removes diffused impurities from the interface once per wave oscillation.

In Fig. 12, one can note that for values of $\chi \ll 1$ the existence of waves does not impact the outflow of HBO at all (at least within the amplitudes considered within the study). The behaviour considered previously in this paper, however, is described by the points corresponding to $\chi = 2.84$. One can note that, as χ approaches 1, the surface waves begin to affect the HBO removal process, but not quite to the extent as previously determined. When $\chi = 2$, practically the same behaviour is retained as when $\chi = 2.84$. This is in accord with our hypothesis that there is a requirement for $\chi > 1$ for surface waves to have an impact on the impurity removal phenomenon.

This may be counter-intuitive – greater diffusion of impurities to the gas phase leads to *less* effect from the wavy surface. However, this does not mean that the concentration outflow is less. In Fig. 12, the value on the vertical axis is the normalized concentration flow, meaning that the absolute concentration flow rates can be different for each case. In fact, total concentration outflow grows with an increasing diffusion coefficient – which is because more impurities can diffuse into the gas phase. However, as diffusion increases, the diffusion length also becomes greater, meaning that the wavy surface has less impact on the process efficiency because it is below the characteristic length of diffusion. For example, in Fig. 11 (a) the value of $\chi = 2$, and in Fig. 11 (b) the value of $\chi = 0.1$. The first case showed a pronounced effect of surface waves on impurity diffusion, the second displayed none.

In real-life applications, it is impossible to impact the molecular diffusion coefficient of some particular substance. However, in practical terms, this allows for the calculation of the minimum wave amplitude required to observe any improvement in effective diffusion (also in terms of wave frequency f if one assumes that must be larger than unity:

$$A \geq 2\sqrt{D_0 T} = 2\sqrt{\frac{D_0}{f}}. \tag{18}$$

Thus, for a given system, one must generate waves of at least such an amplitude to expect any meaningful improvement for the molten silicon purification process. Estimating this value from [10], using $f = 5$ Hz and D_0 for HBO gas, the minimum wave amplitude $A_{\min} \approx 0.017$ m. For a small crucible it is an unfeasible limitation, but for larger crucibles wave amplitudes of a few centimeters should be attainable.

4. CONCLUSIONS

In the analysed surface-to-gas diffusion problem, it was shown that the increased number of jets directed at the surface could not ensure better mass transfer from the surface at the fixed gas flow rate. For this reason, the wavy surface was analysed and it was found that it increased the effective diffusion rate of impurities from the surface by means of several phenomena:

- waves increased the surface area and thus also the effective diffusion rate;
- they altered the flow patterns near the surface, generating more turbulence near the surface and leading to better turbulent diffusion;
- a decreased diffusion boundary length due to an angle between the main flow and the surface also improved the impurity removal rate.

However, a limitation for the effective diffusion from the surface at large molecu-

lar diffusion coefficients was found. This limitation is linked to the ratio between the characteristic molecular diffusion length and the wave amplitude, making this approach unsuitable for small systems.

ACKNOWLEDGEMENTS

The research has been funded by the European Regional Development Fund under contract "Refinement of Metallurgical Grade Silicon Using Smart Refinement Technologies" (No. 1.1.1.1/16/A/097).

REFERENCES

1. International Renewable Energy Agency. (2022). *Renewable Power Generation Costs in 2022* (report). ISBN: 978-92-9260-544-5
2. Kavlak, G., McNerney, J., & Trancik, J.E. (2018). Evaluating the Causes of Cost Reduction in Photovoltaic Modules. *Energy Policy, 123*, 700–710. https://doi.org/10.1016/j.enpol.2018.08.015.
3. Delannoy, Y. (2012). Purification of Silicon for Photovoltaic Applications. *Journal of Crystal Growth, 360*, 61–67.
4. Fu, R., James, L. T., & Woodhouse, M. (2015). Measurements of Polysilicon for the Photovoltaic Industry: Market Competition and Manufacturing Competitiveness. *IEEE Journal of Photovoltaics*, *5* (2), 515–524.
5. Khattak, C., Joyce, D., & Schmid, F. (2002). A Simple Process to Remove Boron from Metallurgical Grade Silicon. *Solar Energy Materials and Solar Cells*, 74 (1), 77–89.
6. Safarian, J., & Tangstad, M. (2012). Kinetics and Mechanism of Phosphorus Removal from Silicon in Vacuum Induction Refining. *High Temperature Materials and Processes*, *31*. 10.1515/htmp.2011.143.
7. Sortland, Ø., & Tangstad, M. (2014). Boron Removal from Silicon Melts by H2O/H2 Gas Blowing: Mass Transfer in Gas and Melt. *Metallurgical and Materials Transactions E*, *1* (3), 211–225.
8. Safarian, J., Thang, K., Hildal, K., & Tranell, G. (2014). Boron Removal from Silicon by Humidified Gases. *Metallurgical and Materials Transactions E, 1*, 41–47.
9. Nordstrand, E. F., & Tangstad, M. (2012). Removal of Boron by Moist Hydrogen Gas. *Metallurgical Material Transactions B, 43*, 814–822.
10. Galpin, J., & Fautrelle, Y. (1992) Liquid-Metal Flows Induced by Low-frequency Alternating Magnetic Fields. *Journal of Fluid Mechanics*, *239*, 383–408. doi:10.1017/S0022112092004452
11. Fautrelle, Y., & Sneyd, A.D. (2005). Surface Waves Created by Low-Frequency Magnetic Fields. *European Journal of Mechanics – B/Fluids*, *24* (1), 91–112. https://doi.org/10.1016/j.euromechflu.2004.05.005
12. Kestin, J., & Whitelaw, J.H. (1964). The Viscosity of Dry and Humid Air. *International Journal of Heat and Mass Transfer*, *7* (11), 1245–1255. https://doi.org/10.1016/0017-9310(64)90066-3
13. Yuan, Z., Mukai, K., & Huang, W. (2002). Surface Tension and Its Temperature Coefficient of Molten Silicon at Different Oxygen Potential. *Langmuir, 18*, 6, 2054–2062. https://doi.org/10.1021/la0112920
14. Sato, Y., Nishizuka, T., Hara, K., Yamamura, T., & Waseda Y. (2000). Density Measurement of Molten Silicon by a Pycnometric Method. *International Journal of Thermophysics, 21*, 1463. https://doi.org/10.1023/A:1006661511770
15. Geža, V., & Pavlovs, S. (2020). Numerical Modelling of Boron Removal from Silicon by Oxidizing Gas Jet. *Magnetohydrodynamics*, *56*, 81–91. doi:10.22364/mhd.56.1.8

16. Rhim, W.K., & Ohsaka, K. (2000). Thermophysical Properties Measurement of Molten Silicon by High-Temperature Electrostatic Levitator: Density, Volume Expansion, Specific Heat Capacity, Emissivity, Surface Tension and Viscosity. *Journal of Crystal Growth*, *208* (1–4), 313–321. https://doi.org/10.1016/S0022-0248(99)00437-6
17. Guevara, F. A., McInteer, B. B., & Wageman, W. E. (1969). High-Temperature Viscosity Ratios for Hydrogen, Helium, Argon, and Nitrogen. *The Physics of Fluids, 12* (12), 2493–2505.
18. Marrero, T.R., & Mason, E.A. (1973). Correlation and Prediction of Gaseous Diffusion Coefficients. *AIChE J.*, 19, 498–503. doi:10.1002/aic.690190312
19. Sortland, O.S. (2015). Boron Removal from Silicon by Steam and Hydrogen. PhD Thesis. Trondheim: Norwegian University of Science and Technology.
20. Khanjian, A., Habchi, C., Russeil, S., Bougeard, D., & Lemenand, T. (2018). Effect of the Angle of Attack of a Rectangular Wing on the Heat Transfer Enhancement in Channel Flow at Low Reynolds Number. *Heat Mass Transfer, 54*, 1441. https://doi.org/10.1007/s00231-017-2244-8
21. Dellil, A.Z., Azzi, A., & Jubran, B.A. (2004). Turbulent Flow and Convective Heat Transfer in a Wavy Wall Channel. *Heat Mass Transfer, 40*, 793. https://doi.org/10.1007/s00231-003-0474-4

sciendo

LATVIAN JOURNAL OF PHYSICS
AND TECHNICAL SCIENCES
2023, N 6

DOI: 10.2478/lpts-2023-0050

DENSITY-BASED TOPOLOGICAL OPTIMIZATION OF 3D-PRINTED CASTS FOR FRACTURE TREATMENT WITH FREEFEM SOFTWARE

K. Kokars[1], A. Krauze[1], K. Muiznieks[1], J. Virbulis[1],
P. Verners[2], A. Gutcaits[3], J. Olins[4]

[1]Institute of Numerical Modelling, University of Latvia,
3 Jelgavas Str., Riga, LV-1004, LATVIA
[2]Institute for Mechanics of Materials, University of Latvia,
3 Jelgavas Str., Riga, LV-1004, LATVIA
[3]Riga Technical University, HPC Center,
3 P. Valdena Str., Riga, LV-1048, LATVIA
[4]SIA CastPrint,
19 Krišjāņa Barona Str., Riga, LV-1011, LATVIA
*e-mail: armands.krauze@lu.lv

3D printed plastic casts can be used for healing bone fractures. The main requirements for these cases are: they should be light, require little printing time, have good mechanical properties, and ensure proper skin ventilation. We present a density-based topology optimization algorithm for obtaining optimal cast shapes that fulfil these requirements. The algorithm uses a linear stress model and simplified boundary conditions to model the contact problems. The cast shapes were optimized against the influence of several sharp corners. The parametric studies showed that the mass of optimized casts was reduced by 20 %–25 % in comparison with original industrial casts, and the printing time is reduced by 1.4–1.7 h for the largest cast. A major model drawback is the use of 3D numerical volume to model the density distribution. The density distribution should be homogenized across the cast layer. The overhang problem should also be addressed. We also suggest that the cast producers collect more experimental data on the cast breakages for a better calibration of the numerical model.

Keywords: *3D printing, medical casts for bone fractures, topology optimization.*

1. INTRODUCTION

3D printing is used to print plastic casts for medical treatment of bone fractures, in particular forearm fractures [1], [2]. 3D-printed plastic casts have significant advantages over traditional plaster casts – they are lightweight, and they can have complex geometries that fit the patient's arm and have holes that enhance skin ventilation (see Fig. 1). Important considerations in the production of 3D printed casts are the mass and printing time of the cast, which determine its production costs and its mechanical durability.

A leading producer of 3D printed casts in Latvia is CastPrint Ltd. Currently, CastPrint Ltd uses the following method to produce 3D printed casts. A scanned 3D surface of a patient's arm is sent to CastPrint Ltd. An operator of the company cuts the scanned surface into two parts and cuts large holes in them. Then a special algorithm generates a triangular mesh with thick connections on the rest of the surface area. After that the surface is extruded to obtain the final 3D shape of the cast; four connectors are added to bind both cast halves together, and then the cast is 3D printed (see Fig. 1) using polylactic acid (PLA plastics) as the material.

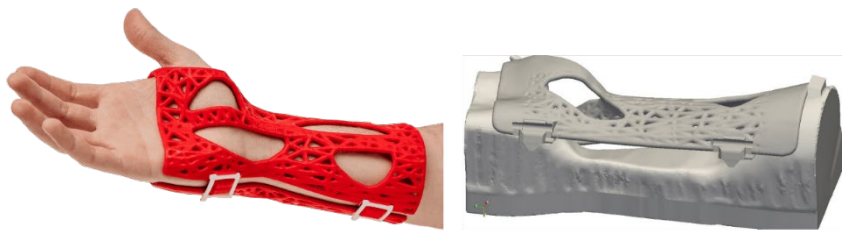

Fig. 1. Examples of original, unoptimized 3D printed casts produced by CastPrint Ltd. Left: a cast on a patient's arm (promotional materials of CastPrint Ltd). Right: A cast part placed on a lower test fixture for mechanical testing (numerical 3D surface meshes).

Such an approach allows obtaining casts with good skin ventilation, but it has two main deficiencies. First, the large amount of manual work is tiresome for operators and causes mistakes during the shape creation. Second, mechanical durability of the cast is not considered when the shapes and positions of the holes are chosen. An alternative approach would be to use a topology optimization algorithm which would choose holes that would minimize the stresses forming in the cast under different applied loads and would also minimize the mass of plastics used in the production. Therefore, a study was needed to examine whether the topology optimization could be used to generate lighter casts with at least the same mechanical strength as the casts obtained by the original approach and whether the topology optimization could be incorporated in an automated production line in which 3D cast shapes would be generated with a minimum input from operators.

Numerical modelling was used to determine optimal cast geometry in the past. A very simple approach was used in [1], where the authors considered three different hole patterns for a cast, calculated stress

distributions for two different loads for each pattern and determined the best pattern by comparing maximum stresses and displacements. A powerful two-step topology optimization algorithm was used in [3], [4]. In the first step, the cast surface was meshed with a coarse mesh (100–200 cells) using Voronoi tessellation. The cell sizes were iteratively adjusted to minimize a temperature-based sensitivity comfort functional. In the second step, holes were cut in the cells, and a new finer mesh was constructed. A series of mechanical stress simulations was carried out for a given applied force load, in which the local thickness of the cast was iteratively varied until the local stress values dropped below a predefined maximum level. It seems that the interaction between the cast and the arm tissue was not considered. In [5], a density-based topology optimization algorithm, also known as SIMP (solid isotropic material with penalization, see also [6], [7]), was used to optimize compression casts. The mechanical stresses in the casts were modelled using a thin plate model, which allowed to reduce the mesh size. The authors optimized the cast geometry against the pressure exerted by compressed tissues of patient's extremities. Interaction with external objects was not used in the optimization.

This paper presents an optimization algorithm for the geometry of forearm healing casts which is also based on the density-based topology optimization algorithm (SIMP). The development of the model is the result of collaboration between CastPrint Ltd, the Institute of Numerical Modelling, where the model was developed, RTU HPC Center, which provided the computer resources for simulations, and the Institute for Mechanics of Materials, which carried out mechanical tests of original and optimized casts. The model was developed in the frame of a project to design an automated production chain for 3D-printed casts, which would be implemented in the production line of CastPrint Ltd. To reduce costs, the algorithm was implemented via opensource software such as *FreeFEM*, [8], and *python* scripts.

The optimization algorithm consists of two parts: a simplified model for stress simulations, in which interactions with external objects are modelled via simplified boundary conditions, and the topology optimization algorithm that uses the stress simulation results. Due to practical considerations, the project set a limit to the duration of an optimization simulation per cast (one hour). For this reason, several series of simulations were performed to determine whether it was feasible to satisfy this limit, what simplifications should be done in the model for this purpose, and what the optimum values of the model parameters were that could be used for a wide range of casts. Below, a brief description of the optimization model is given, and the results of parametric simulation studies are shown and discussed. The results of mechanical testing of original and optimized 3D printed casts are also presented.

2. MODEL DESIGN AND BOUNDARY CONDITIONS

2.1. Model for Stresses

A 3D-printed cast (Fig. 1) consists of two separate parts connected with four connectors that fix it on the patient's arm. Modelling an interaction of such a cast with an

external object requires, in general, a solution of dynamic contact problems between at least four objects (the arm, the two cast parts, and the object), which could also involve non-linear deformations. Solving such a problem is practically unfeasible, given the time limit set by the project.

To make simulations practical, the stress model was significantly simplified. First, a linear stress model is used under the assumption that the linear model can predict at least the positions of the regions with high stresses. If the cast shape is optimized against the stresses obtained with the linear model, the optimized shape would still work for stronger, non-linear stresses provided that the qualitative distribution of the stress maxima remains the same. Second, an equation for steady-state stresses σ^{ij} is solved:

$$\nabla\sigma^{ij} = 0, \tag{1}$$

where the gravity force is discarded due to its small importance. In the weak formulation, this equation can be rewritten as

$$\oiint f^i \tilde{u}_i \, ds - \iiint \sigma^{ij} \tilde{\varepsilon}_{ij} \, dv = 0, \tag{2}$$

where $\tilde{u}_i$ are test functions in the form of a displacement field, $\tilde{\varepsilon}_{ij}$ is a deformation tensor formed from $\tilde{u}_i$, and f^i is the force density field that describes the interaction between the cast and the external world.

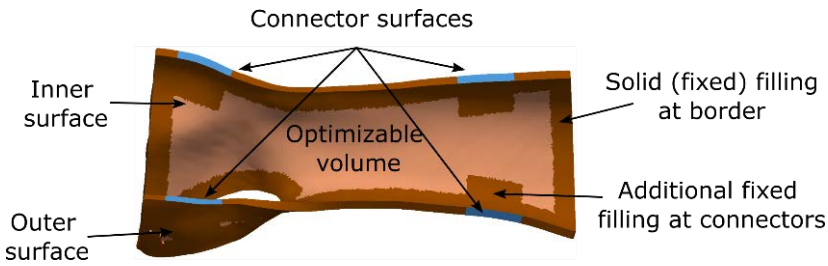

Fig. 2. Numerical representation of one half of a 3D printed cast.

In principle, f^i is not known and is obtained together with σ^{ij} by solving the contact problem. However, to speed up the simulation time, the contact problem is significantly simplified. The stress equation is solved separately for each half of the cast. The interaction of a cast half with the surrounding environment occurs on three surfaces (see Fig. 2): the outer surface can interact with external objects, the inner surface interacts with the arm, and the interaction with the other half of the cast is modelled on four connector surfaces. The contact problem for each of these surfaces is modelled via a special simplified boundary condition.

On the outer surface, the cast can interact with large external objects such as walls or table edges, but modelling such interactions is difficult. For example, a wall can be modelled as a plane surface, but one must ensure a correct plane orientation that does not cut through the cast. It seems that interactions with large objects require proper modelling of the contact problem, which would be too cumbersome and time consuming. For this reason, interactions with large objects were not modelled. Instead, interactions with small, sharp objects are considered.

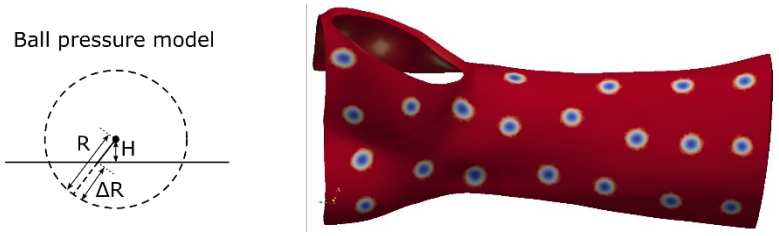

Fig. 3. Left: the parameters of the ball pressure model.
Right: an example of ball position distribution on a cast half.

The influence of a small object can be modelled as a pressure distribution on a small area of the outer surface. The pressure has its maximum in the centre of the area, and it decreases to zero at the area boundary. Since the exact details of such a pressure distribution are not important, the following simplified model is used. A point on the outer surface is chosen. A ball with the radius R is drawn at the height H above the point (see Fig. 3). The applied pressure distribution is calculated as $p = A_{ball}\Delta R$ for the outer surface points inside the ball (ΔR is defined as shown in Fig. 3). The pressure distribution outside the ball is zero.

Several impact positions are modelled in the simulations. The stress equation is solved for each position, and the simulation results are averaged before using them in the topology optimization model. The exact statistics of the impact distribution on the outer surface is not known, so it is assumed that it is homogeneous, and the ball positions are spread out evenly across the outer surface (see Fig. 3) by using a special algorithm.

Due to pressure concentration, the topology optimization algorithm places material around the ball impact points and forms holes between them. Thus, by changing the number of impact points, one can influence the distribution and size of the holes to some extent. A major drawback of this approach is that the hole distribution is heavily dependent on the impact positions. By choosing different initial ball positions, one can obtain a completely different hole distribution.

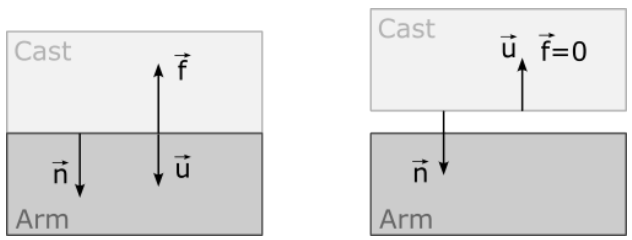

Fig. 4. Qualitative model of forces acting on the inner surface. Left: the pushback from the arm when the cast is pressed into it. Right: no forces when there is an air gap.

For the inner surface, it is assumed that when the cast is pushed against the arm (the normal component of the inner surface displacement $u_n > 0$), the arm pushes back with a force density that is proportional to u_n (see Fig. 4). However, if $u_n < 0$, an air gap forms between the arm and inner surface, and there is no force acting on the inner surface. Mathematically this is described by the following boundary condition:

$$\vec{f} = -H(u_n)A_{skin}u_n\vec{n}, \quad (2)$$

where $\vec{n}$ is the normal of the inner surface, A_{skin} is a constant, and $H(u_n)$ is the Heaviside step function.

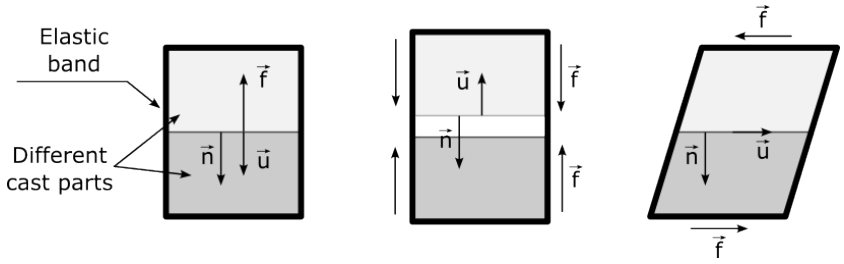

Fig. 5. A model for the contact problem between the connectors of the two cast halves.

The model for the contact problem on the connector surfaces is more complex (see Fig. 5). The cast halves are bound to each other by elastic bands that are put on the connectors (see Fig. 1). The connectors themselves are not modelled. Instead, there are four connector surfaces on the surface of each cast half (see Fig. 2), where the connectors will be placed in the post-processing stage. The forces arising in the interaction between the connectors are modelled as force density distributions on the connector surfaces. It is assumed that a normal force acts on the connector surface when it is pushed against the other cast half. A normal force is also created by the elastic band when an air gap develops between the connectors (it is also possible that the connectors are locked to each other). The elastic band also creates a tangential force when a cast part slips tangentially against the other part. Thus, the following boundary condition is applied on the connector surfaces:

$$\vec{f} = -\left(A_{soft} + H(u_n)\left(A_{hard} - A_{soft}\right)\right)u_n\vec{n} - A_{soft}\vec{u}_\tau, \quad (3)$$

where A_{soft}, A_{hard} are constants, and $\vec{u}_\tau$ is the tangential $\vec{u}$ component. The tangential term ensures the numerical stability of the solution.

A series of mechanical tests of the 3D printed casts were carried out (see Fig. 1). To compare the results of the mechanical test to the stress simulations and validate the chosen model, the model described above is modified to model the test conditions. The upper fixture in the tests was a cylinder. The interaction with it is modelled via a surface pressure distribution calculated as:

$$p_{cyl} = A_{cyl}\Delta R_{cyl}, \quad (4)$$

where ΔR_{cyl} was calculated as a difference between the cylinder radius and the distance of an outer surface point to the cylinder axis. The pressure on the points that lay outside the cylinder is set to zero. Such a model can be justified by the fact that only a small part of the cylinder touched the cast part. Zero force density is applied to the connectors, and the boundary condition for the inner surface is modified to:

$$\vec{f} = -H(u_n)\left(A_{skin}u_n\vec{n} + A_{skin,friction}\vec{u}_\tau\right)F_{groove,mask}, \quad (6)$$

where $A_{skin,friction}$ is an artificial friction coefficient introduced for numerical stability, and $F_{groove,mask}$ is a mask function, which models the groove on the fixture. $F_{groove,mask}$ is set to zero, if the inner surface points lie above the groove of the bottom fixture. It is also set to zero for holes in the cast. Otherwise, the value of this function is one.

2.2. Topology Optimization Algorithm

Due to the complex geometry of the 3D printed casts, a density-based topology optimization algorithm is used for the cast optimization, because it does not change the simulation mesh. The applied algorithm is based on a 2D topology optimization algorithm for a cantilever, which was implemented as a *FreeFEM* script in [9]. This model was rewritten and expanded to use it for optimization 3D printed casts and to make it run on parallel processors.

The core concept of the density-based topology optimization algorithm is a scalar field h, which determines the material distribution in the cast ($h = 0$ means no material and $h = 1$ means fully filled). The material properties are calculated as functions of the field h. For example, the level of material filling at a given point in the cast volume is calculated by using a smooth approximation to the Heaviside step function $H(t, \beta)$, which is defined as

$$H(t,\beta) = \frac{1/2(\tanh\beta/2 + \tanh\beta(t - 1/2))}{\tanh\beta/2}, \quad (7)$$

where β determines the sharpness of the transition area between the holes and fully filled areas. The β value is increased incrementally (every fifth iteration in the script), so that a very sharp material distribution is obtained at the end of the simulation. The total volume of a cast is calculated as the integral:

$$V = \iiint H(h,\beta)\, dv. \quad (8)$$

The material properties (the Lamè coefficients) are also defined as functions of h:

$$\lambda = \lambda_0\zeta\left(H(h,\beta)\right), \quad (9)$$

$$\mu = \mu_0\zeta\left(H(h,\beta)\right), \quad (10)$$

where λ_0 and μ_0 are the actual material properties of the plastic, and $\zeta(t)$ is defined as:

$$\zeta(t) = e_{rs} + (1 - e_{rs})t^3, \quad (11)$$

where $e_{rs} = 0.001$ ensures that holes have non-zero material properties. All material properties are isotropic; the anisotropy caused by the 3D printing technology is ignored.

The optimal cast topology is obtained by iteratively modifying the field h to minimize the functional:

$$J(h) = \iiint \sigma^{ij}\varepsilon_{ij}\, dv + e_{ll}\left(\frac{V - V_t}{V_0}\right)^2. \quad (12)$$

The first term represents the total deformation energy. Minimizing it reduces the stresses in the cast and the risk of the cast

breaking. The second term is a penalty function that forces the solution to converge to a target material filling level V_t/V_0, where V_0 is the whole simulation volume, and V_t is the desired material amount. e_{ll} is a scaling coefficient for the penalty term, the value of which is determined in the parametric studies.

The deviation δh that minimizes J is calculated in each iteration step as:

$$\delta h = -k\left(-\frac{\partial \sigma^{ij}}{\partial h}\varepsilon_{ij} + \frac{2e_{ll}(V - V_t)}{V_0^2}\frac{\partial H}{\partial h}\right)F_{opt}, \quad (13)$$

where k is the step. The step size is adjusted to the rate of change of the function J. The stress derivative is calculated as:

$$\frac{\partial \sigma^{ij}}{\partial h} = \frac{\partial \lambda}{\partial h}I(\varepsilon)\delta^{ij} + 2\frac{\partial \mu}{\partial h}\varepsilon^{ij}. \quad (14)$$

F_{opt} is a special mask function that is used to exclude certain areas of the cast from the optimization. For example, it was required that holes should not reach the borders of the cast parts, so a 5–10 mm wide zone of continuous material is created at the borders (see Fig. 2). This zone is enlarged to 20 mm at the connectors.

A known problem of the topology optimization is the checker-board instability, in which material properties can change from filled to hole in neighbouring mesh cells. To avoid this, δh distribution is smoothed by solving the equation:

$$\alpha^2 \Delta \delta h^* = \delta h^* - \delta h, \quad (15)$$

where α is the smoothing scale. The smoothed deviation δh^* is added to the h field. The same smoothing algorithm is applied to the h field before the calculation of the material properties.

3. RESULTS AND DISCUSSION

3.1. Numerical Implementation

The iterative topological optimization algorithm was implemented as a script for the finite element program *FreeFEM* [8]. The equations for the stresses and smoothing operators are expressed in their weak forms; the Laplacian operator and gradients are expressed via the first order derivatives ∂_x, ∂_y, ∂_z, the discretization schemes of which are implemented in *FreeFEM*. *FreeFEM* uses only tetrahedron meshes for volume discretization.

The *FreeFEM* script forms a part of the software that was developed for an automatic generation of 3D printable cast shapes. The generation of a printable cast (Fig. 6) begins by scanning the surface of a patient's arm and splitting the scanned surface into two parts, which is done already by CastPrint Ltd in the case without topological optimization. A special *python* script reads the scanned surfaces and remeshes them with *gmsh* program [10] to obtain a homogeneous surface mesh with ~1.5 mm cell size. The 3D tetrahedron mesh is obtained by extruding the surface mesh by 4 mm (the cast thickness). The *python* script also defines all necessary boundary surfaces and sets the region with fixed filling.

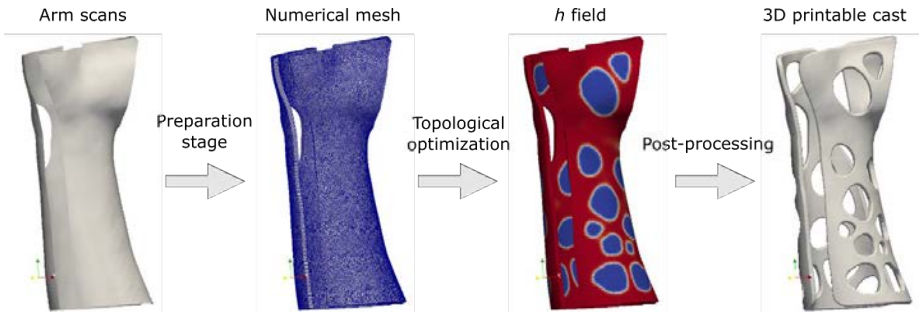

Fig. 6. Outline of generation of 3D-printable casts from scanned patient arms.

After the generation of the numerical mesh, the python script reads numerical parameters and physical property values of the model and launches a parallelized simulation on an HPC cluster. The result of the simulation is the distribution of the h field (Fig. 6). In the post-processing, the h field is averaged across the cast layer, and a 3D surface distribution of the averaged h field is obtained. *mmg* software [11] is used to cut out holes along the $h = 0.5$ isolines of the averaged field, after which the mesh is extruded again, and sharp corners and edges are rounded. The post-processed 3D cast geometry can be printed after adding connectors manually. All simulations are carried out on the RTU HPC Center computer cluster. Typically, a simulation is run on 24 to 36 processors.

3.2. Results of Parametric Studies

A series of simulations was performed in the parametric studies of the optimization model to determine the optimal parameter values that would be valid for different types of casts. Arm scans of five different persons, labelled from P1 to P5, were used in the simulations: four adults and a child (P3). Table 1 lists the obtained model parameter values and applied material properties of the PLA plastics.

For the PLA plastics, the Young's modulus $E = 2.9$ GPa is used as a representative value, see [12]. The PLA plastics material is assumed to be isotropic; however, the casts are 3D printed by fusing together heated PLA filaments, layer by layer, and the casts tend to break apart along the fusion lines in the mechanical tests. This suggests that the PLA material in the casts could have anisotropic properties, but this problem is ignored in the current model.

The ball radius and height above the outer cast surfaces were kept constant in the simulations. Their values guarantee that the ball pressure areas are small in comparison with the cast dimensions. In principle, the value of the ball pressure scale could be estimated if characteristic parameters of the interaction of the patient with sharp corners were known. However, our stress model is quasi-linear, and a solution u_i obtained for some A_{ball} value can be scaled by a positive number k to obtain a solution for increased pressure value kA_{ball}. Correspondingly, deformation energy density scales as k^2. Therefore, if an optimized topology (i.e., the h field distribution) is obtained for some A_{ball} and e_{ll} values, we should be able to obtain the same h distribution for kA_{ball} and $k^2 e_{ll}$ values. Since the h field is the solution, and u_i is only an intermediate

help value, we decided to use an arbitrary $A_{ball} = 3\ \mathrm{GPa/m}$ value in all simulations. (This value corresponds to about 150 N pressure created by the ball.)

Table 1. Parameter Values Used by the Topology Optimization Model

Parameter	Value		Parameter	Value
Young's modulus, E	2.9 GPa		A_{ball}	3 GPa/m
Poisson's coefficient, v	0.36		Ball radius R	10 mm
Cell size	1.5 mm		Ball height H	8.75 mm
Iteration number	80		Ball position density	1600 m^{-2}
e_u	1.5 J		A_{skin}	1 MPa/m
α	5mm		A_{skin} for mechanical tests	100 MPa/m
Filling level V/V_0	0.75		A_{hard}	100 GPa/m
β	0.75..12		A_{soft}	10 GPa/m
k	0.0005..0.2		$A_{skin,\ friction}$	1 MPa/m

In the final scripts used in the production line, only the first order finite elements are used on a one-layer mesh. The first order elements, however, are very imprecise, and simulations with the second order finite elements were also conducted. The simulations with the second order finite elements produced significantly higher displacements and stresses for the same applied boundary conditions. To compare the optimization results, the ball pressure scale A_{ball} was reduced for the second order elements. The obtained distributions of the h field for the first and second order finite elements are compared in Fig. 7. There are general similarities between the solutions, but the second order finite elements produced additional holes in the middle section.

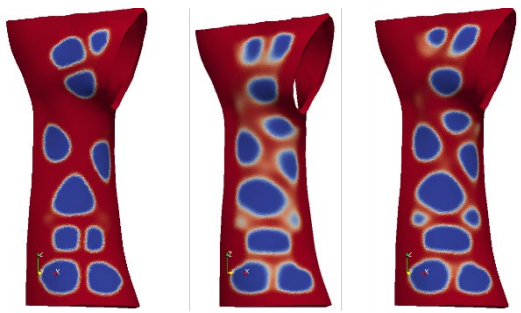

Fig. 7. Topologically optimized shapes of the cast P4. Simulations with $A_{skin} = 1\ \mathrm{MPa/m}$. Left: simulation with first order finite elements, $A_{ball} = 3\ \mathrm{GPa/m}$. Middle and right: simulations with the second order finite elements and $A_{ball} = 1.2\ \mathrm{GPa/m}$ and $A_{ball} = 2\ \mathrm{GPa/m}$. Filling level $V_t/V_0 = 0.70$.

Table 2 shows the approximate times required by simulations for the largest and smallest casts with different finite element orders. The simulations with the second order elements require 5–8 more time than the first order elements, and they can last several hours for the largest cast. This makes the use of the second order finite elements completely impractical for this project. For this reason, all simulation results below are obtained with the first order elements.

Table 2. Comparison of Simulation Times for the Largest (P1) and Smallest (P3) Casts for Different Finite Element Orders

Number of processors	P1, 1st order	P1, 2nd order	P3, 1st order	P3, 2nd order
24	0.9 h	7.2 h	0.3 h	1.5 h
36	0.7 h	5.1 h	0.2 h	1.1 h

Similar conclusions can be made about the mesh size. Using more than one layer in the mesh would increase the simulation time beyond the acceptable one-hour limit. Our experience showed that the 1.5 mm cell size for the surface mesh was also optimal.

Convergence of the h field (see Fig. 8) shows that the solution practically converges after about 81 iterations. The h field distribution slightly fluctuates from iteration to iteration; for this reason, all simulations are run for a fixed number of 81 iterations in the production scripts.

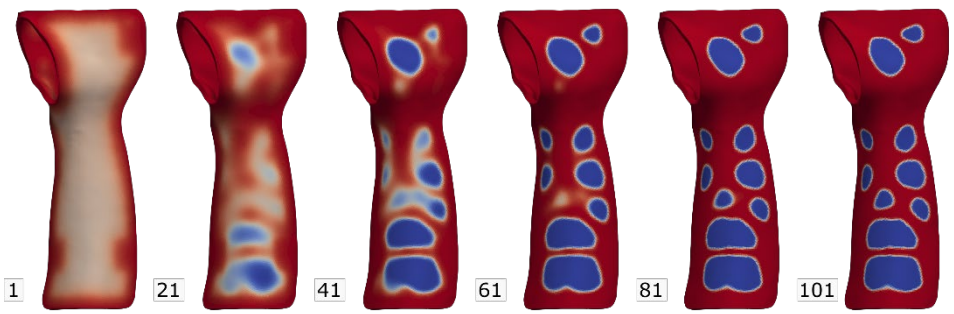

Fig. 8. Convergence of field h at different iterations. Topological optimization of P1. Target material filling level $V_t/V_0 = 0.75$, $e_{ll} = 1.5$ J, $A_{skin} = 1$ MPa/m.

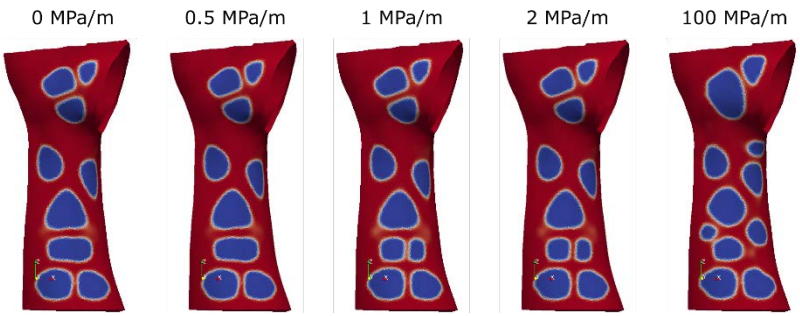

Fig. 9. Dependence of the h field distribution on A_{skin} for the cast P4. Filling level $V_t/V_0 = 0.70$. Basic values for other parameters.

The value of the elastic arm response A_{skin} is estimated as ~ 2 MPa/m from the data in [13]. However, there is an additional sheet of soft material between the cast and arm to prevent their direct contact. Therefore, a smaller value $A_{skin} = 1$ MPa/m was chosen as its basic value. A series of simulations with different A_{skin} values was performed to determine its influence (see Fig. 9). The calculated h field distributions remain practically the same for $A_{skin} = 0..2$ MPa/m, which suggests that the arm influence is small. Significant h field changes can be observed when very large A_{skin} values are used.

It is difficult to estimate the value of the A_{hard} coefficient due to the complex shape of the cast. $A_{hard} = 100$ GPa/m was chosen as its basic value, which corresponded to the elastic response of about 30 mm thick plastic layer. It was assumed that A_{soft} was ten times smaller than A_{hard}. A series of simulations with ten times smaller A_{hard} and A_{soft} was carried out (see Fig. 10). The simulation results show a significant change in the h field distribution both when A_{hard} and A_{soft} are changed. It seems that the connectors are major limiters for the movement of the casts, and the stress distribution is more sensitive to the A_{hard} and A_{soft} values. Therefore, the values of A_{hard} and A_{soft} could be potentially improved further by building a more precise model for the reaction of the cast to the forces on the connector surfaces.

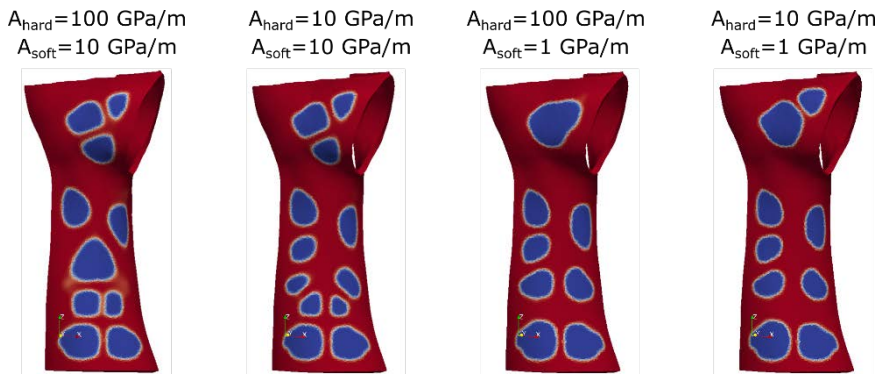

Fig. 10. Dependence of the h field distribution on A_{hard} and A_{soft} for the cast P4. Filling level $V_t/V_0 = 0.70$. Basic values for other parameters.

Fig. 11. Topologically optimized P1 shapes for different filling levels. The shape for 65 % filling level shows abnormalities: development of overhangs and a thin connection between two large holes in the middle of the cast.

The optimum material filling level for the casts was estimated to be ~0.70..0.75. With such fillings, the printing time of the P1 cast is reduced by 1.4..1.7 h (compared to 10.5 h which is required by the original cast), and its mass is reduced by 20 %–25 %, (see Table 3). More mass and printing time could be reduced when lower filling levels were used (60 %–65 %). However, such casts are mechanically weaker (see Table 4) and have a greater risk of the development of material overhangs which 3D printers cannot print (see Fig. 11). Similar mass reduction is achieved for the P3 cast (see Table 5).

Table 3. Estimated Masses and Printing Times for the P1 Cast; Comparison between the Original Design of CastPrint Ltd and Optimized Designs with Different Target Filling Levels

Parameter	Original	Optimized, 0.60	Optimized, 0.70	Optimized, 0.75
Mass	208 g	139 g	148 g	160 g
Printing time	10.5 h	8.4 h	8.75 h	9.1 h

The parameter e_{ll} determines the weight of the deviation of the cast filling level from the set target value in the optimization functional (12). Increasing e_{ll} allows obtaining solutions where the actual filling level is closer to the target value. However, at very large e_{ll}, the convergence of the solution worsens, and h field fluctuations increase. The hole boundaries can also become diffused. The results of numerous simulations have shown that $e_{ll} = 1.5$ J is an optimal value that guarantees reasonably small deviations (by few percent) of achieved filling levels from their target values for casts of different sizes (see Fig. 12).

Table 4. Maximum Values of the von Mises Stress σ_{vM} and Deformation Energy $\sigma^{ij}\varepsilon_{ij}$ in the Area around the Palm Base of the Cast P3. Simulation Results for Different Filling Levels

Filling level, V/V_0	0.60	0.65	0.70	0.75
Maximum of σ_{vM}	63.3 MPa	62.8 MPa	59.5 MPa	59.1 MPa
Maximum of $\sigma^{ij}\varepsilon_{ij}$	0.113 MJ/m^3	0.105 MJ/m^3	0.077 MJ/m^3	0.076 MJ/m^3

Table 5. Estimated Masses and Printing Times for the P3 Cast; Comparison between the Original Design of CastPrint Ltd and Optimized Design

Parameter	Original	Optimized, 0.65
Mass	102 g	75 g
Printing time	5 h	4.5 h

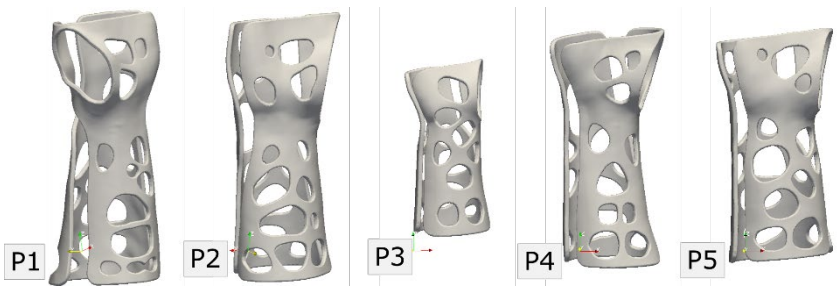

Fig. 12. Optimized 3D-printable cast geometries for five test patients. Target material filling level $V_t/V_0 = 0.70$, $e_{ll} = 1.5$ J, $A_{skin} = 1$ MPa/m.

An important parameter that determines, for example, the hole size is the smoothing scale α. It is suggested in [9] that α should be about the size of the mesh cell. In our case, the optimum value of $\alpha = 5$ mm is approximately the same as the thickness

of the cast (4 mm). Smaller α values can cause layering of the plastic material in the cast (i.e., a local change of the thickness). A possible solution to the layering problem which would also allow using smaller α was to use a 3D surface mesh to model the h field distribution (i.e., to use the same material properties across the layer). The material properties would have to be mapped to the 3D volume, and the stress simulations in the 3D volume would have to be mapped to the surface.

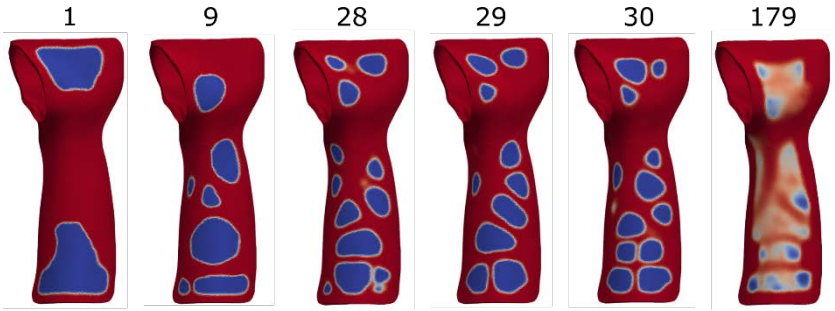

Fig. 13. h field distributions in the P1 cast obtained for different number of ball positions. Basic values for other parameters with the filling level $V_t/V_0 = 0.70$.

A special parametric study was carried out to determine the optimal number for the ball positions (Fig. 13). The number should be large enough to properly model the impact statistics. However, if the number of positions is large, it also increases the simulation time, and, for very large numbers, the h field distribution becomes diffuse. The optimum value for ball position density is estimated to be 1600 m^{-2} which corresponds to 20–30 positions per cast half for adults.

3.3. Results of Mechanical Tests

Samples of 3D printed casts were tested in ZwickRoell Z100 TEW material testing machine in a custom fixture that allowed bending of a cast perpendicularly to the fixture (see Fig. 14). The upper test support was a 60 mm diameter cylinder. The lower test fixture was a copy of patient's arm with the middle section hollowed out to allow free movement of the sample during the bending test. Both fixtures were made of 3D-printed high-performance polyether-based thermoplastic polyurethane filament, which smoothed the distribution of the applied force in a larger area.

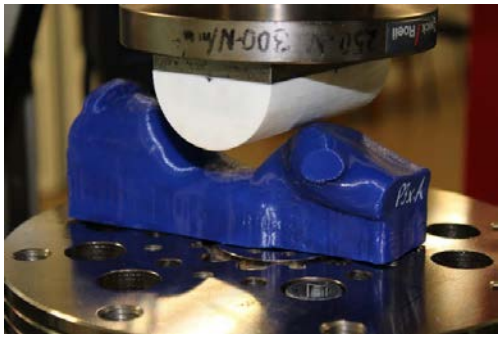

Fig. 14. The cylindrical upper test support together with a lower test fixture for the P3 cast in the ZwickRoell Z100 TEW material testing machine.

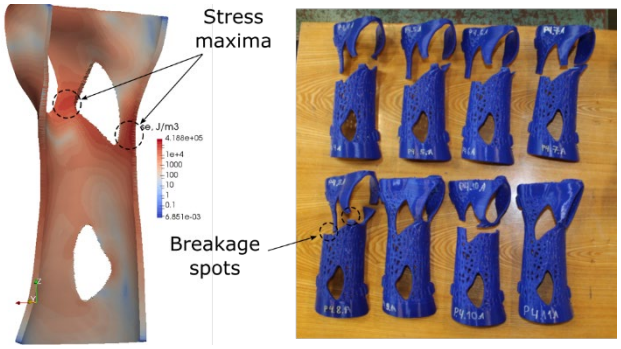

Fig. 15. Left: simulated deformation energy density distribution in original P4 casts in mechanical testing facility. Right: P4 casts broken in mechanical tests.

In the first batch of experiments, original CastPrint casts were tested. The test results for the P4 cast showed that the casts typically broke at specific spots at the palm base (Fig. 15). To validate our linear stress model, a numerical model of the original cast P4 was developed in which the major holes of the cast were modelled. The model parameters (for example, A_{skin}) were adjusted to fit the simulation results to the available data from the tests – the maximum bending of the cast was 6 mm at 100 N force. The cast deformations at the 6 mm bending are most likely nonlinear; however, the breaking spots correspond well to the calculated maxima of the deformation energy density $\sigma^{ij}\varepsilon_{ij}$ (see Fig. 15). Therefore, it seems that the linear stress model can still predict correctly critical stress concentrations against which the cast geometry should be optimized.

In the second test, a topologically optimized P3 cast, obtained with $A_{skin} = 100$ MPa/m and target filling level 0.65, was printed and tested. The test showed that the average breakage force for the optimized cast (635 N) was about 1.5 times higher than for original casts (431 N) (see Fig. 16), even though the optimized casts are 25 % lighter. Thus, the topological optimization could potentially increase the mechanical strength of the casts, but more tests were required for a more definite claim.

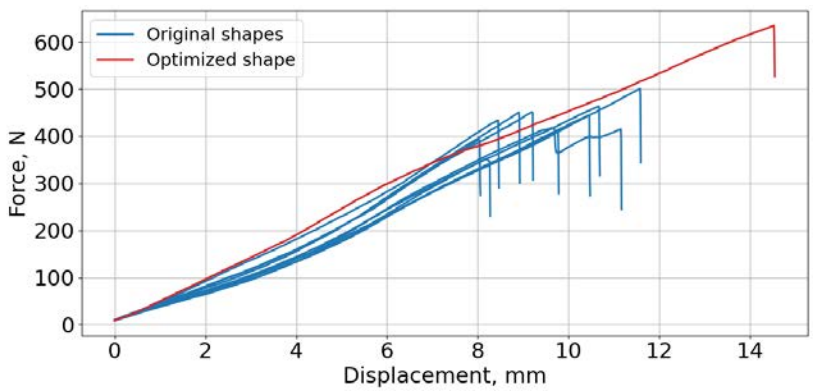

Fig. 16. Results of mechanical tests for the cast P3. Maximum displacement of the casts during bending versus applied forces. Comparison between ten 3D printed casts with the original shapes of CastPrint Ltd and the one optimized shape.

3. 4. Implications of the Results: Discussion

We have shown that the density-based topology optimization can be used to build a software program that produces a 3D-printable cast geometry from a scan of a patient's arm in less than an hour, which fulfils the project requirements. The parametric studies have also shown significant problems with our approach. The model requires significant simplification of the contact problem and can only use the first order finite elements, which makes the simulation results imprecise. To use more precise second order elements, one must speed up simulations ~5 times.

Using a 3D volume mesh is also a significant drawback of the model. It allows layering of the material, which can be solved only by using a very large smoothing parameter . It seems that the thin plate model used by [5] is more advantageous, because it automatically solves the layering problem and requires smaller meshes.

Our simulation results depend significantly on the parameters for the connectors, which means that additional modelling is required to better estimate the values for these parameters. A more general problem is that the interaction of the cast with large objects such as walls is ignored. Perhaps, the current model with many ball positions could be replaced by a model with few interactions with large objects, but this requires the actual statistics of the interactions of the cast with external objects.

A significant and unsolved problem in the current model is the overhang formation. Here, the model based on the hollowed Voronoi tessellation [4] shows significant advantage, because it allows controlling the shapes and positions of the holes.

The current model also considers only the constant thickness casts. It might be more advantageous to make the cast thicker in places where it breaks more often. For this purpose, we suggest that CastPrint Ltd. collect information about actual breakings that occur during the exploitation of the casts. Such information can also be used to calibrate the boundary conditions for the model and to determine whether the mechanical tests replicate well the conditions of the actual use. Finally, more mechanical tests with different casts and more loads should be conducted to make more definite conclusions about the optimization quality.

4. CONCLUSIONS

The results of numerical modelling have showed that a density-based topology optimization model can be used to optimize the shapes of 3D-printed casts. The shapes are optimized against multiple loads created by small balls placed at different places on the cast to model the statistics of the cast interactions with sharp corners. The interaction between both cast halves and between the cast and the arm are also modelled. However, the numerical model requires significant simplifications to make it practical for industrial applications. The contact problems must be significantly simplified, and the first order finite elements must be used.

The simulation results have demonstrated that the mass of the optimized casts is reduced by 20 %–25 % in comparison with the original casts of CastPrint Ltd. The printing time for the largest cast is reduced by 1.4–1.7 h which exceeds the time spent on the simulations. Similar time reduction

is obtained for the smallest cast. These are significant improvements in the cast production from the industrial point of view. The created optimization model has been implemented in the cast production line, and it can be used to generate 3D-printable cast shapes.

The conducted mechanical tests on the smallest cast have shown that it may be more durable than the original cast of Cast-Print Ltd. However, only one optimized cast sample has been tested, which is insufficient to make any definite conclusions. More mechanical tests with a larger variety of mechanical loads should be conducted in the future.

The simulation results show that using a 3D numerical volume to model material distribution in the cast is a drawback, and the material distribution should be homogenized across the cast layer (this could be done, for example, by using a thin plate model). The problem of material overhangs should also be addressed in the future model versions. The anisotropy of the plastic material properties caused by the production process should be considered, too.

Finally, the cast interactions with other types of external objects should be considered (for example, walls). A significant problem here is the lack of experimental data on the interactions of the casts with external objects. We suggest that the cast producers collect more data on the breakages of the cast during their exploitation, which could help in developing better boundary conditions for the numerical model.

ACKNOWLEDGEMENTS

The research has been financed by the project "Application of HPC Tools for the Optimization of 3D-printed Orthopedic Devices (H2020-JTI-EuroHPC-2019-2, Experiment 1109–OrthoHPC)".

REFERENCES

1. Ranaldo, D., Zonta, F., Florian, S., & Lazzaro, J. (2023). A Facile, Semi-Automatic Protocol for the Design and Production of 3D Printed, Anatomical Customized Orthopedic Casts for Forearm Fractures. *Journal of Clinical Orthopaedics and Trauma, 42*, 102206.
2. Lin, H., Shi, L., & Wang, D. (2015). A Rapid and Intelligent Designing Technique for Patient-Specific and 3D-Printed Orthopedic Cast. *3D Printing in Medicine, 2* (1), 4.
3. Zhang, X., Fang, G., Dai, Ch., Verlinden, J., Wu, J., Whiting, E. & Wang, Ch. (2017). Thermal-comfort design of personalized casts. In *UIST '17: Proceedings of the 30th Annual ACM Symposium on User Interface Software and Technology* (pp. 243–254). ACM, New York, USA.
4. Rao, C., Tianc, L., Yan, D.-M., Liao, Sh., Deussen, O. & Lu, L. (2019). *Computer Aided Geometric Design, 71*, 130–141.
5. Zhang, Y., & Kwok, Tsz. (2019). Customization and Topology Optimization of Compression Casts/Braces on Two-Manifold Surfaces. *Computer-Aided Design, 111*, 113–122.
6. Sigmund, O., & Maute, K. (2013). Topology Optimization Approaches. *Structural and Multidisciplinary Optimization, 48*, 1031–1055.
7. Bendsoe, M. P. (1989). Optimal Shape Design as a Material Distribution Problem. *Structural Optimization, 1*, 193–202.
8. Hecht, F. (2012). New Development in FreeFem++. *Journal of Numerical Mathematics, 20*, 251–265.

9. Bonnetier, E., & Dapogny, C. (n.d.). *Optimization of a Cantilever Beam with Density-Based Topology Optimization Algorithm. An Introduction to Shape and Topology Optimization*. Available at https://membres-ljk.imag.fr/Charles.Dapogny/coursoptim.html
10. Geuzaine, C., & Remacle, J.-F. (2009). Gmsh: A 3-D Finite Element Mesh Generator with Built-in Pre- and Post-Processing Facilities. *International Journal for Numerical Methods in Engineering, 79*, 1309–1331.
11. Balarac, G., Basile, F., Bénard, F. P., Bordeu, F., Chapelier, J.-B., Cirrottola, L., … & Zakari, M. (2022). Tetrahedral Remeshing in the Context of Large-Scale Numerical Simulation and High Performance Computing. *MathematicS In Action, 11* (1), 129–164.
12. Pszczółkowski, B., Nowak, K.W., Rejmer, W., Bramowicz, M., Dzadz, Ł., & Gałęcki, R. (2022). A Comparative Analysis of Selected Methods for Determining Young's Modulus in Polylactic Acid Samples Manufactured with the FDM Method. *Materials, 15*, 149.
13. Van Kuilenburg, J., Masen, M. A., & van der Heide, E. (2012). Contact Modelling of Human Skin: What Value to Use for the Modulus of Elasticity? *Proc IMechE Part J: J. Engineering Tribology, 227* (4), 349–361.

sciendo

LATVIAN JOURNAL OF PHYSICS
AND TECHNICAL SCIENCES
2023, N 6

DOI: 10.2478/lpts-2023-0051

ANALYSIS OF THE HEAT EXCHANGER ENERGY EFFICIENCY OF VARIABLE CROSS SECTION WITH AN INHOMOGENEOUS COOLANT

S.E. Sakipova, B.R. Nussupbekov, D.A. Ospanova,
K.M. Shaimerdenova, B.B. Kutum

E.A. Buketov Karaganda University,
28a Universitetskaya Str, Karaganda, 100024, KAZAKHSTAN
*e-mail: sakipovasaule@gmail.com

One of the main priorities in the modern thermal power engineering development is the problem of energy saving due to the economical use of fuel and energy reserves. Increasing energy consumption with a simultaneous increase in energy prices and widespread environmental degradation necessitates the development and implementation of energy efficient technologies to save fuel, materials and labour costs. The object of study is tubular heat exchangers of variable cross section, which are widely used in steam generators of nuclear power plants, gas turbines and transport plants. Scale deposit properties and the composition of the heat coolant were studied, and their influence on the energy efficiency of heat exchangers was analysed. To study the scale deposits and coolant influence on the energy efficiency of heat exchangers, their properties were examined using an atomic emission analysis with the help of a TESCAN electron microscope. The principles of implementing technologies aimed at intensifying heat transfer, reducing hydraulic and heat losses in heat exchangers were formulated.

Keywords*: Condenser tube, heat transfer, inhomogeneous coolant, peak boiler, scale deposits, variable cross-section.*

1. INTRODUCTION

Efficient use of energy is the most pressing problem in energy development at the present stage. Energy conservation includes a wide range of interrelated activities and techniques to ensure efficient use of energy, i.e., solving problems of reducing energy losses and its effective use at all stages [1]–[4]. In many energy and technological processes, inhomogeneous liquid media are widely used as a coolant, for example, water vapour in the flow part of turbines, in steam generators, mixtures in various heat

exchangers, etc. The parameters and state of the coolant largely determine the hydrodynamics of the flow, which in turn affects the rate of heat exchange processes.

The intensity of heat exchangers depends on many factors and conditions, including the degree of variability of the cross section of the pipeline, which is often found in various heat exchange devices [5], [6]. The narrowing or expansion of the channel leads to a change not only in the flow rate of the coolant, but also in a transition in the nature of the flow from laminar to turbulent due to the appearance of vortices and additional swirling of the flow. The flow pressure on the pipeline walls changes, and the amount of friction increases. The presence of a variable cross section affects the hydrodynamics of the flow of a non-uniform coolant, its thermophysical properties and the intensity of various reactions. The appearance of reaction heterogeneity can cause a decrease in the heat transfer of the reactor. In the study [7], a "model of thermal coupling between the powder layer and the coolant" was established for a reactor with an annular fin of variable cross section. It has been discovered that it is possible to effectively eliminate the phenomenon of inhomogeneous response by adjusting the angle of inclination between the outer profile and the outer edge of the layer.

The creation of efficient heat exchangers is one of the priority tasks of thermal power engineering that arises when designing heat supply for industrial structures and residential buildings. To increase the efficiency of heat exchange in heat exchangers, as a rule, turbulization of coolant flows is used [4], [8]–[11]. For example, [9] proposes to use porous metal inserts in a shell-and-tube heat exchanger, which increase the heat transfer surface and the apparent conductivity of the porous medium. With such optimization, it is important to balance two opposing contributions: increased heat transfer and losses due to pressure drop. In addition, the manufacture and installation of porous inserts require additional costs.

Article [12] provides a description of the technological process for purifying process water to prevent scale formation in heat exchangers at production facilities in the energy industry. Quantitative costs for reagents and additives used to purify source process water at thermal power plants can be found in article [13]. The authors also analysed the dosing of additional water to soften the antiscale agent.

Obviously, the degree of heat transfer depends on the purity of heat exchange processes, during which scale deposits occur over time [14]. The presence of even a very thin coating of intra-pipe deposits masks the heat transfer process. In [6], a description is given of an effective method for cleaning heat transfer surfaces from standard deposits using electrohydraulic action. Despite the technique used, cleaning using electrohydraulic action occurs no more than 1–2 times a year, and sometimes even after a year or two. In this case, the operation of the heat exchanger itself temporarily stops. During the heating season, it is necessary to take into account the influence of scale deposits on the heat exchanger.

The present study mainly focuses on the patterns of formation of scale deposits in heat exchange pipes taking into account the treatment of process water (coolant) in accordance with established standards at existing heat and power facilities. To carry out the experiments, separate fragments of turbogenerator condenser pipes and peak boiler pipes were taken, cut from various sections from heat exchangers after seasonal operation in 2021–2022 at CHPP-3 in Karaganda.

2. EXPERIMENTAL PART. MATERIALS AND RESEARCH METHODS

Let us consider the features of some technologies for processing coolant in combined heat and power plants using the example of a water treatment plant (WTP). The standard technology of the water treatment process includes several stages, such as filtration, ultrafiltration, softening with Na-cation resin, etc. [15]. This step-by-step water treatment technology makes it possible to reduce to a minimum the amount of hazardous chemicals used (sulfuric acid, sodium alkali) compared to traditional technologies. At the water treatment facility, process water, preheated to a temperature of 25□35 °C, is supplied through a pipeline. Since the amount of water being treated is quite large (>1200 m^3/h), to ensure the stability of the WTP, the flow is divided into four parallel flows between pressure filtration units, with four filter columns in each. The filters are loaded with anthracite. Part of the filtrate is accumulated in filtered water storage tanks TW-40/1 and TW-40/2 to provide the required amount of water for backwashing the filters, part is used to prepare a coagulant solution, and the rest of the filtrate is supplied to the ultrafiltration unit. If the water preparation technology allows for a higher content of hardness ions, clarified water pre-treated with antiscalant after ultrafiltration units can be immediately sent to storage tanks.

Effluents from pressure filters and ultrafiltration units are transported through water pipelines, into which, to accelerate the deposition of suspended matter into sediment, a 0.1% flocculant solution is dosed by flocculant preparation and dosing unit. In wastewater from chemical backwashes using sodium hypochlorite, the concentration of free chlorine in the wash water will be up to 20–25 mg/l. To neutralize free chlorine in wastewater, sodium bisulfite is dosed during recirculation. Wastewater with a neutral pH value is discharged into the wastewater system. The listed water treatment processes should ensure uninterrupted operation of the heat and power process. However, as practice shows, after long-term operation, solid scale deposits form in heat exchange pipes [16], [17].

As noted above, during the heating season, due to the formation of scale deposits, the cross section of the pipeline becomes variable. Visual analysis of longitudinal and transverse sections of heat exchange pipes with diameter *d* showed that the nature and thickness of scale deposits were changing along the length of the pipe (see Fig. 1). Another photograph of the same boiler pipe fragment is shown in [6] (Fig. 2a). The uneven formation of scale deposits is clearly visible here.

a *b*

Fig. 1. Photos of a cross section of heat exchange pipes with scale deposits:
(a) – condenser pipe, *d* = 28mm; (b) – peak boiler pipe, *d*=19 mm.

The greatest thickness of deposits is formed, as a rule, at the inlet section of the coolant or immediately after the turn (bend) of the pipe. Even in a straight section, scale deposits form in the form of rings of varying thickness and width, alternating at certain distances. Between these so-called annular scale formations, the coolant actually moves as if through a pipe of variable cross section.

3. RESULTS AND DISCUSSION

As part of the study, a spectral analysis of the coolant used in the peak boiler tube and the condenser pipe was carried out for the content of chemical elements. According to standard technology, atomic emission analysis of the dry residue of the coolant liquid was carried out. Table 1 shows the content of chemical elements in coolant samples before and after treatment at the WTP. It can be seen that if the content of some elements, such as P, Zr, practically does not change after treatment on WTP, then the concentration of other elements decreases (Pb, Ag) or increases (Sc, Mn, Ga, Be, Zn) several times. The spectral analysis protocol dated 16 October 2022 noted that the elements Au, Hf, Hg, In, Pt, Ta, Te, Th, Tl, U were not detected.

Table 1. Chemical Composition of the Heat Coolant

Heat coolant samples:	Sc, mg/kg	P, mg/kg	Mn, mg/kg	Pb, mg/kg	Zr, mg/kg	Ga, mg/kg	Ni, mg/kg	Be, mg/kg	Mo, mg/kg	Yb, mg/kg	Zn, mg/kg	Ag, mg/kg
before processing	<1	<300	50	15	≤5	<1	≤2	<0.3	1	<0.5	<20	0.15
after processing	8	<300	150	<2	5	20	10	1.2	5	1.5	40	0.12

Despite the fact that the same coolant was used in the experiments on the studied sections of the heat exchanger, differences in the concentrations of the same chemical elements were found in samples of scale deposits taken in different sections of the heat exchanger (see Table 2). For example, zinc present in the coolant was not detected in scale sample No. 2.

Table 2. Chemical Composition of Scale Deposits

Scale deposits samples	Sc, mg/kg	Pb, mg/kg	Ti, mg/kg	Zr, mg/kg	Ga, mg/kg	Cr, mg/kg	Ni, mg/kg	Mo, mg/kg	Sn, mg/kg	Li, mg/kg	Yb, mg/kg	Zn, mg/kg	Ag, mg/kg
No. 2	4	120	300	15	3	80	50	3	500	<10	0.5	8000	1.2
No. 3	≤1	10	30	5	<1	5	250	≤1	12	<10	<0.5	800	<0.05

The structure and composition of scale deposits was studied using a TESCAN electron microscope. Atomic emission (spectral) analysis was used as a determination method; the results are shown in Figs. 2–6. General map spectrum was obtained as a result of superposition and processing of several spectra taken at different points of the sample (see Fig. 2a). For example, for deposits in the boiler pipe at different points 12 spectra were obtained.

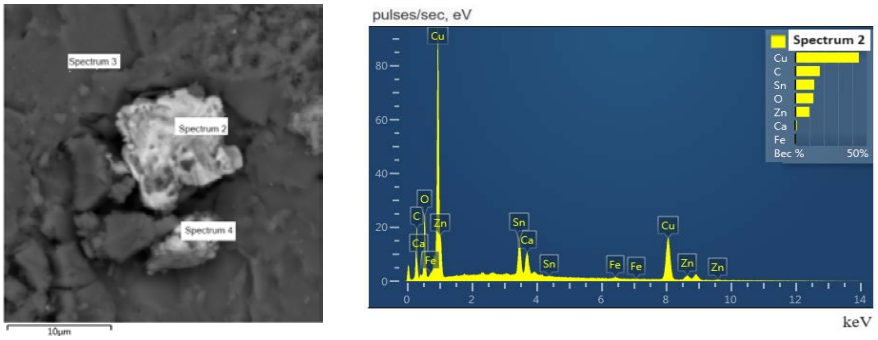

a b

Fig. 2. Electronic image of (a) and (b) elemental composition of scale deposits in the condenser tube; d = 24 mm.

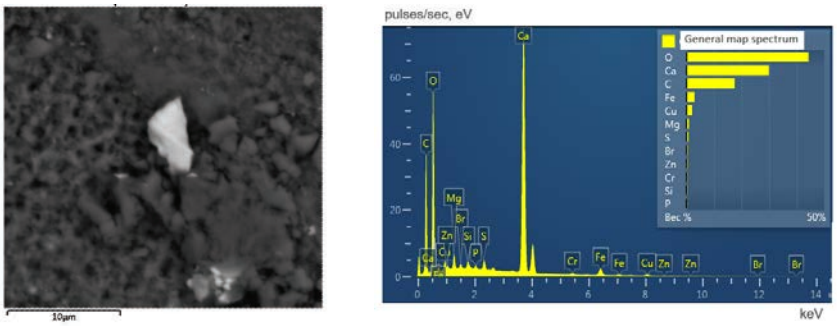

a b

Fig. 3. Electronic image of (a) and (b) elemental composition of scale deposits in the condenser tube; d = 28 mm.

Figures 4–6 show multilayer EDS maps obtained as a result of energy dispersive analysis (EDS) of chemical elements across layers of scale deposits. On the EDS-map, chemical elements are shown by different colours.

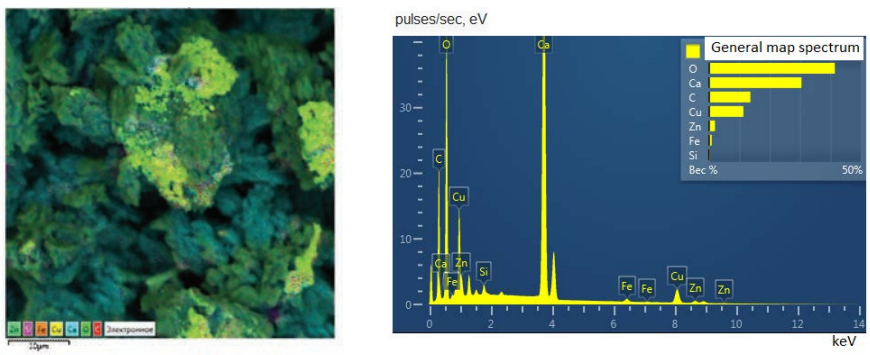

a *b*

Fig. 4. Multilayer EDS-map (a) and (b) elemental composition of scale deposits in condenser tube; d = 24 mm.

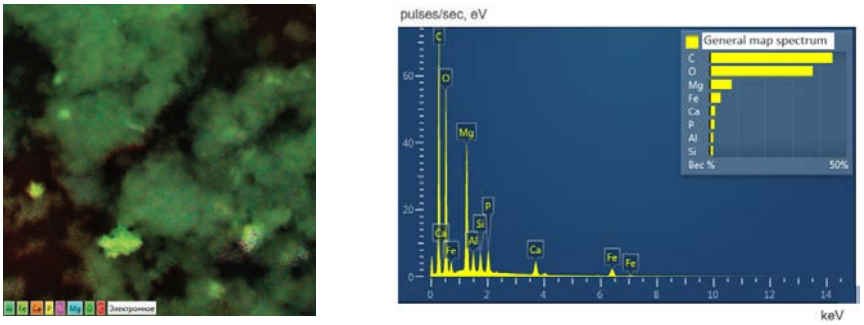

a *b*

Fig. 5. Multilayer ECD map (a) and (b) elemental composition of deposits in boiler pipe; *d* = 19 mm.

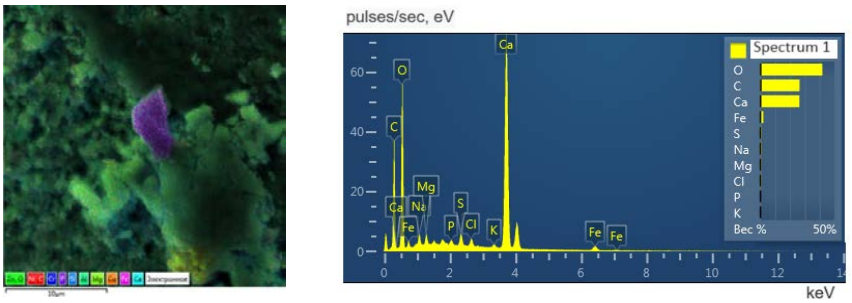

a b

Fig. 6. Multilayer ECD map (a) and (b) elemental composition of scale deposits in the condenser tube; *d* = 28 mm.

Thus, in fact, the coolant is a multicomponent mixture of technical water with various chemical elements, in which phase transformations also occur. When flowing at different speeds in an inhomogeneous coolant, due to temperature changes, gas bubbles appear, which also affect the intensity of heat exchange processes. To construct a computational model, a regression analysis of experimental data was carried out using the method of group consideration of arguments (GMCA). The principle of constructing the calculation algorithm and the methodology for choosing a criterion to ensure the quality and accuracy of the model are described in [18]. It is shown in [19] that, if all conditions are maintained, the presence of a narrowing or expansion of the tubular channel leads to a significant restructuring of the nature of the flow in the initial section of the pipe, which in turn determines the intensity of heat transfer along the entire length. As a result of the regression analysis of the data, the following calculation formula for the heat transfer coefficient was obtained:

$$Nu = 101{,}5 - 14{,}5\frac{l}{d} + 445\beta^2 + 0{,}75\left(\frac{l}{d}\right)^2 + 39{,}5\beta\cdot\frac{l}{d} + 0{,}01\alpha^3\cdot\beta\cdot\frac{l}{d} - 13\alpha\cdot\beta^2\cdot\frac{l}{d},$$

where α is the angle of narrowing or expansion of the channel; *l*/*d* is the calibre, determined by the ratio of the distance from the edge of the pipe to the measured section to the diameter of the pipe; β is a gas content coefficient.

As a result of the calculations, graphs of the dependence of the heat transfer coefficient on the concentration of the gas phase at various distances from the edge of the pipe at different constriction angles (α = 10°, 20°, 30° и 60°) were obtained. It was shown that along the entire length of the pipe, an increase in the concentration of the gas phase led to an increase in the intensity of heat transfer at the same flow rate.

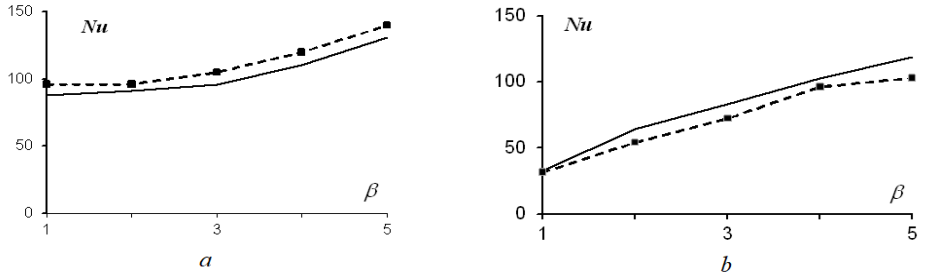

Fig. 7. Dependence of the heat transfer coefficient on the concentration of the gas phase in a non-uniform coolant along the length of the pipe: (a) l/d=1 and (b) l/d=10; channel narrowing angle α=10°; Re = 2450; ■ – an experiment, line – a calculation.

In the immediate vicinity beyond the sharp expansion (expansion angle α=180˚) at a speed of Re≈5103, the presence of gas bubbles has virtually no effect on the level of turbulence of the flow. In the separated flow zone, the intensity of heat exchange is the same as during the movement of a homogeneous fluid. With an increase in the Reynolds number, gas bubbles in a zone of high turbulence play the role of dampers of turbulent pulsations, as a result of which the intensity of heat transfer decreases. At small diffuser expansion angles (α ≤ 20˚), the size of the separation zone and the level of flow turbulence increases; the presence of gas bubbles can also lead to an increase in the level of flow turbulence. Thus, the addition of a gas phase can help increase heat transfer intensification by 10–12 %.

4. CONCLUSIONS

The performance of the heating system will reduce over time without proper care and annual maintenance. Hard water can result in scale deposits lowering the heat transfer rate. Large deposits in the heat exchanger will also reduce the heat transfer rate and negatively affect the boiler efficiency.

It is known that the intensity of a heat exchanger depends on the characteristics of its hydrodynamics of motion and the properties of the inhomogeneous coolant. As part of the project, the structure and chemical composition of scale deposits and the coolant were studied using a spectral analysis. The effect of the scale deposits nature and sizes on the energy efficiency of heat exchangers was considered.

A regression analysis of experimental data was carried out, which made it possible to identify some patterns of heat transfer during the flow of a non-uniform flow through channels of variable cross section. The research results can be used to develop

a reagent in the process of treating a coolant liquid, which helps prevent the formation of scale deposits. In addition, by creating a variable cross section it is possible to further turbulize the flow and, accordingly, intensify heat exchange processes.

ACKNOWLEDGEMENTS

The research has been funded by the Science Committee of the Ministry of Science and Higher Education of the Republic of Kazakhstan (Grant no. AP14870433).

REFERENCES

1. Gerasimov, A.A., Aleksandrov, I.S., & Dorokhov, P.I. (2015). *Energy Efficiency in Engineering Systems: Module Reference Book*. Kaliningrad.
2. Siegenthaler, J. (January, 2011). *How to Improve the Energy Efficiency of Boiler Systems.* Available at https://www.weil-mclain.com/news/boiler-systems-and-energy-saving
3. Laptev, A.G., Nikolaev, N.A., & Basharov, M.M. (2011). *Methods of Intensification and Modelling of Heat and Mass Transfer Processes: Educational and Reference Manual*. Moscow. [in Russian]
4. Stehlik, P., Jegla, Z., & Kilkovsky, B. (2013). Possibilities of Intensifying Heat Transfer in Heat Exchangers for High Temperature Applications. *Chemical Engineering Transactions*, *35*, 439–444. doi:10.3303/CET1335073
5. Zhang, T. (2020). Methods of Improving the Efficiency of Thermal Power Plants. *Journal of Physics: Conference Series*, *1449*, 012001. doi:10.1088/1742-6596/1449/1/012001
6. Nussupbekov, B.R., Sakipova, S.E., Ospanova, D.A., Kutum, B.B., Shaimerdenova, K.M., & Bekturganov, Zh.S. (2022). Some Technological Aspects of Cleaning Pipes of Heat Exchangers from Solid Scale Deposits. *Bulletin of the Karaganda University. Physics Series*, *4* (108), 106–114. doi: 10.31489/2022PH4/106-114.
7. Liu, Y., Wang, H., Ayub, I., Yang, F., Wu, Z., & Zhang, Z. (2021). A Variable Cross-section Annular Fins Type Metal Hydride Reactor for Improving the Phenomenon of Inhomogeneous Reaction in the Thermal Energy Storage Processes. *Applied Energy, 295*, 117073. https://doi.org/10.1016/j.apenergy.
8. Laptev, A.G., Basharov, M.M., & Farakhov, T.M. (2017). Determination of Heat Transfer Coefficients in Channels with Process Intensifiers. *Energy Problems, 19*, (11–12), 112–118.
9. Wajs, J., Bajor, M., & Mikielewicz, D. (2019). Thermal-Hydraulic Studies on the Shell-and-Tube Heat Exchanger with Minijets. *Energies, 2*, 3276. https://doi.org/10.3390/en12173276
10. Rydalina, N., Antonova, E., Akhmetova, I., Ilyashenko, S., Afanaseva, O., Bianco, V., & Fedyukhin, A. (2020). Analysis of the Efficiency of Using Heat Exchangers with Porous Inserts in Heat and Gas Supply Systems. *Energies*, *13* (22), 5854. https://doi.org/10.3390/en13225854.
11. Popov, I.A., Shchelchkov, A.V., Yarkaev, M.Z., Al-Janabi, A.Kh.A., Skrypnik, A.N. (2014). Heat exchangers with heat transfer intensification. *Energy of Tatarstan*, *1* (19), 10–16.
12. Brodov, Yu.M., Aronson, K.E., Ryabchikov, A.Yu., Blinkov S.N., Kuptsov V.K., Murmansky I.B. (2016). Increasing the Efficiency of Heat Exchangers of Steam Turbine Installations through the Use of Profile Twisted Tubes. *News of Universities. Energy problems,* (7–8), 72–78.

13. Kutum, B.B., Ospanova, D.A., Nussupbekov, B.R., & Oshanov, Y.Z. (2023). Research of Process Water of a Thermal Power Plant. *Eastern-European Journal of Enterprise Technologies*, 2 (6–122), 53–61. doi: 10.15587/1729-4061.2023.276486.
14. Ospanova, D. A., Kutum, B. B., & Nusupbekov, B. R. (2022). Features of Nutrient Water Purification in Thermal Power Facilities. *Actual Scientific Research in the Modern World. International Science Journal,* 10 (90), 138–144.
15. Tekhnologicheskie resheniya proekta 09L129 "Ustanovka t.a. st. no. 5 Vodopodgotovka podpitki teploseti s predochistkoy" razrabotany dlya JSC Institut KazNIPIEnergoprom (2019). Karaganda, 187. [in Russian]
16. Karabelas, A. J. (2002). Scale Formation in Tubular Heat Exchangers. *International Journal of Thermal Sciences*, 41 (7), 682–692. https://doi.org/10.1016/S1290-0729(02)01363-7
17. Sakipova, S.E. (2009). Study of the Structure of Scale Deposits on Heat Transfer Surfaces and Technology for their Destruction. *Bulletin of KarSU. Physical Series, 1* (53), 66–71.
18. Ivakhnenko, A.G. (1975). *Long-term Control and Forecasting of Complex Systems.* Kyiv. [in Russian]
19. Sakipova, S.E., Shaimerdenova, K.M., Nussupbekov, B.R., Ospanova, D.A., & Kutum, B.B. (2023). Modeling the Dynamics of Heat and Mass Transfer Processes in a Tubular Heat Exchanger under Pulsed Influences. *Eurasian Phys. Tech. J., 20* (1(43), 51–55. doi.org/10.31489/2023No1/51-55